EROSION IN STEADY STATE DRAINAGE BASINS

A THESIS
SUBMITTED TO THE FACULTY OF THE GRADUATE SCHOOL
OF THE UNIVERSITY OF MINNESOTA
BY

Leslie Edward Hasbargen

IN PARTIAL FULFILLMENT OF THE REQUIREMENTS
FOR THE DEGREE OF
DOCTOR OF PHILOSOPHY

Professor Chris Paola, Adviser
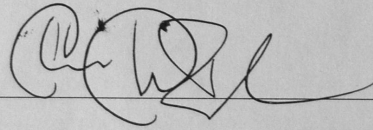
May 2003

UNIVERSITY OF MINNESOTA

This is to certify that I have examined this copy of a doctoral thesis by

Leslie Edward Hasbargen

and have found that it is complete and satisfactory in all respects, and that any and all
revisions required by the final examining committee have been made.

Chris Paola

Name of faculty advisor

Signature of Faculty Adviser

2003 May 29

Date

GRADUATE SCHOOL

Acknowledgments

To the following friends and colleagues: I have immensely enjoyed our conversations about water, sediment, erosion, topography, process, advective-diffusive systems, system behavior, modeling, scaling, and imagination:

Chris Paola, Gary Parker, Efi Foufoula-Georgiou, Victor Saposhnikov, John Swenson, Doug Allen, Dan Doctor, Kelin Whipple, Roger Hooke, Alan Howard, Chris Beaumont, Peter Molnar, Greg R. Hancock, Garry Willgoose, Dave Furbish, Nikki Strong, Michal Tal, Josh Roering, Leonard Sklar, Bill Dietrich, Jeff Niemann, and Alessandro Bigi. A special thanks to Basil Tikoff for teaching me my first FORTRAN syllable!

Thanks to you all for sharing ideas, and invoking new views upon this delightful world!

This thesis could not have been conducted without the unflagging and generous support (both material and intellectual) from the staff at St. Anthony Falls Laboratory. I thank Chris Ellis for creative technical assistance with automated systems design, and Ben Erickson for assistance with digital imagery.

I also acknowledge friends (Ellen Margolis and Ryan Reed, Rob Pierce, Herb and Lynne Fredricksen, Jeff Rosas and Nan Silver, Dave and Lori Tillery, Jennifer Moore, Doug Allen and Kristen Borges) and family (Don and Gladys Hasbargen, Susan and Ty Roland, Lou and Judy Gattoni, Linda and Tom Hering, Judy and Terry Kleman, Mike Hasbargen, and Scott Lindsten) whose faith in my ability supported me through times of doubt, and whose love brought me back from the mental confusion and emotional anguish at the edge of the unknown…

Finally, I thank my advisor, Chris Paola, whose intellectual generosity gave meaning to academic freedom, and whose ideas permeate this thesis.

Dedication

I dedicate this thesis to my life-long partner, Laura Gattoni, whose faith and support kept me going when I really dug myself into a hole. Far beyond the document itself, this thesis required long hours of isolation and work at the laboratory, and engulfed my energy and imagination. While this document can in no way make up for the time lost together and the loneliness of being an academic's partner, it nonetheless stands as a testament to a joint effort and sacrifice. You have my deepest gratitude for encouraging me to explore and follow my passion. You are the *sine qua non*, my dear, and I could not have done this without you!

Abstract

Current numerical landscape evolution models, when forced with steady, uniform uplift and rainfall, evolve from a random initial condition to fully developed drainage basins. In this final state, ridges and valleys cease to evolve, and erosion rate is spatially uniform and everywhere equal to the uplift rate. This thesis project developed a physical experiment to test this proposition.

As a check on published reports of model stability, a stream power erosion law was implemented in a numerical landscape evolution model. Additional terms were added to the erosion law to account for local diffusion, slope aspect driven diffusion, spatial and temporal variation in rainfall, and temporal variation in uplift. Time series of elevation extracted from each run verify that a numerical erosion model based on stream power develop stable, uniformly eroding landforms. The addition of diffusion to the erosion law, and spatial variations in rainfall patterns and temporal variations in uplift did not destabilize the landform.

An erosion facility was constructed to test the proposition that landscape erodes uniformly under steady and uniform forcing conditions. A series of seven runs were conducted where uplift rate and rainfall intensity were varied between runs. While a *statistically* steady form developed for each run, all of the experimental landforms failed to replicate the spatially uniform erosion exhibited by numerical erosion models at long term steady forcing. Intrinsic mass transport processes, such as hillslope failures, deposition, and knickpoint propagation, exhibit nonuniform erosion at both short and intermediate time scales, where the pertinent time scale is that required to erode through a relief of the drainage basin. Experimental landforms experienced migration, extension, and annihilation of drainage divides long after the landform had attained an overall balance between uplift and erosion. A hypothesis derived from this thesis supposes that local, short-term erosional variability coupled with upstream drainage capture develops persistent destabilizing feedback in experimental landscapes, resulting in spatial organization of erosion across the landscape. Similar processes operate in natural settings, and suggest that natural drainage basins may behave in a similar fashion.

TABLE OF CONTENTS

Figures and Tables

xiv

Chapter 1
Introduction To Landform Evolution

A recurrent theme in geomorphology has been the manner in which landscapes evolve over time. The treatment of drainage basin development has a long history, and a variety of landform evolution models, ranging from conceptual to quantitative, have been proposed over the last two centuries (Playfair, 1802; Gilbert, 1877; Davis, 1899; Penck, 1924; Glock 1931; Horton, 1945; Strahler, 1950; Melton, 1958; Hack, 1960; Shreve, 1966; Ahnert, 1970; Hack, 1976; Willgoose et al., 1991; Chase, 1992; Beaumont et al., 1992; Leheny and Nagel, 1993; Kramer and Marder, 1993; Howard, 1994). The recent development of physics-based process modeling, and the rapid advancement and availability of fast computers has sparked renewed interest in landscape evolution. Virtual landscape evolution can now be observed on computer screens. The quantitative results from such visualizations beg for a suitable test.

Tests of theoretical models of drainage basin evolution, however, have been hampered by the long time required to observe significant changes in natural landscapes. Model validation has largely been restricted to statistical comparison with natural drainage basins. A reasonable requirement for comparison between two drainage basins is that they both experience similar conditions for a period of time of sufficient length such that the landscape has adjusted to forcing. This is very difficult to establish in natural settings. We have limited access to storm event distributions, rock uplift, and base level history that would allow us to develop a quantitative simulation of a real world basin. Significant strides are being taken in this direction, but detailed records are not likely to ever be developed on the spatial and temporal scales required for rigorous model testing.

Small scale physical experiments, however, do provide a means of testing these models. Simplifications of erosional processes employed in theoretical models can also be applied to physical experiments. This thesis documents the construction and monitoring of such a physical experiment, and comparisons of dynamic behavior between theoretical and physical experiments will be presented herein.

Numerous variables play a role in landscape form. As mentioned above, uplift of material past a fixed base level, climatic conditions, vegetative cycles, rock erodibility, and time all play a role in setting the form of the landscape. Given the wide range of possible combinations of these fundamental variables, how does one construct a suitable test? Fortunately, a robust and invariant result of the current numerical models is that, under long term uniform and steady forcing, the model landscapes reach a stationary steady state condition. The topographic surface remains fixed as uplift of material past a base level is balanced by erosion at every point in the landscape. Ridges and valleys become fixed spatially, and lateral migration of topographic features ceases. This result implies that dendritic drainage basins do not develop significant destabilizing feedback under steady forcing, a result that a steadily forced physical experiment can readily test.

The thesis is organized as follows. The introduction offers an historical overview of drainage basin erosion studies; a review of current research into erosion in natural landscapes; and an overview of previous work on physical experiments. A recapitulation of the stream power erosion model formulation follows, and a numerical landscape model that typifies steady state topographic stability will be presented. Chapter 2 documents the design and implementation of an experimental erosion facility, discusses data collection methods, and a presents a series of steady state runs at varying uplift and rainfall rate conditions. Chapter 3 examines drainage basin topography via a set of simple statistical measures, and compares experimental, numerical, and natural drainage basins. Chapter 4 offers evidence for divide migration and stochastic erosion rates of forced erosional landscapes, based on physical experiments from this thesis project, and summarizes two attached papers that encapsulate key aspects of landscape dynamics. Chapter 5 discusses larger scale behavior that could influence short term rates, and searches for the source of drainage structure instabilities. Chapter 6 summarizes the results of this thesis, and discusses implications and future directions for research.

Historical Overview of Drainage Basin Research

The systematic arrangement of stream and ridge networks in natural landscapes has long captured the imagination of scientists. Playfair described drainage basins as trees,

with each stream delicately adjusted such that at each joining of streams, the slopes were balanced, neither too large nor too small (Playfair, 1802). He used this observation as direct evidence that the geometry of the landscape was the result of current processes operating within the landscape. The systematic change of slopes within stream networks suggested to Playfair that an equilibrium existed in drainage basins between erosion and sediment transport over the entire basin, and a stable geometry resulted from this balance.

Gilbert (1877) described weathering and erosional processes in landscapes, and linked landscape form to erosional processes. He noted that erosional landforms are convergent stream and divergent ridge networks, and proposed that the typical concave-up profile of streams is due to the increased volume of water moving through downstream sections in the drainage network. He postulated that divides between adjacent streams must migrate toward the stream with a shallower gradient, with stable channel networks achieved once gradients in adjacent streams are similar. Instability of drainage lines could be explained in terms of differential lithologic resistance to erosion, differential uplift, time, and possibly the interaction between stream transport capacity and availability of sediment for transport. Gilbert acknowledged that this model of landscape sculpture was based entirely on flow convergence, and could only produce concave-up profiles with slopes approaching infinity near divides (Gilbert, 1877). To explain the problem of convex hillslopes near divide crests, he considered hillslope processes to be dominated by soil creep forced by contraction and expansion of the soil layer (Gilbert, 1909). He postulated that to maintain a constant erosion rate over the hillslope, mass transport must increase with distance from the divide, and required an increasingly steep slope to do so. Gilbert thus established the conceptual groundwork for the dominant mechanisms operating within erosional landscapes. For Gilbert, the network of streams and hillslopes represented a strongly interactive system. He envisioned that adjustments occurring in any part of the basin propagated throughout the drainage basin. He developed several thought experiments that demonstrate the basic effects of rock resistance, discharge, and abrasion of bedrock by stream load on stream profiles and hillslopes in drainage basins.

At the dawn of the twentieth century Davis (1899) postulated a series of forms that landscapes assume as a function of the age of the landform. This conceptual model is based on observations of a variety of landforms that he organized into a time series (ergodic reasoning, or the substitution of space for time). He assumed that uplift occurs as a single rapid event, and that the response time for streams is shorter than for hillslopes. The short response time allows for initial rapid incision followed by exponential decay of the hillslopes. No constant form exists, and hillslopes and channels are weakly coupled. The landscape reaches a steady state form when a peneplain develops, and erosion approaches nil. He described this evolution as a youthful stage involving incision and channel network extension in response to an uplift event, followed by progressive rounding of the hillslopes and broadening of valleys in a mature stage, to an old age characterized by a peneplain.

Glock (1931) used similar ergodic reasoning in a model of stream network evolution in which streams extend rapidly into a previously undissected region, then experience a removal of streams as master streams incise more rapidly and capture smaller streams. He termed this evolution extension (addition of low order streams) and abstraction (removal of lower order streams). In Glock's view, the landscape continuously evolves toward a stable network dominated by a trunk stream with straight segment branches (i.e., minimized paths to the trunk). Glock's model implies that a static steady state topography is reached after a significant phase of drainage basin reorganization.

Strahler (1950) characterized erosional landscapes as open mass transport systems that adjust their morphology to attain a time-independent form. He measured valley side slope angles from several completely dissected natural drainages, and showed that a given area maintains a characteristic slope with a narrow range of values. The presence of a characteristic slope lends support to the hypothesis of a static steady state landform. However, he also demonstrated that hillslope angles measured from basins of similar size and rock type can have significantly different mean values, while basins of similar size and dissimilar rock types could yield similar hillslope angles. Hence, he thought other factors such as climate or vegetation likely influenced slope angles.

Hack (1960) summarized growing discontent with the Davisian geographic cycle in a paper on dynamic equilibrium in landscapes. He hypothesized that every stream and hillslope is adjusted to each other, and given constant forcing conditions, all elements of the landscape erode at the same rate, similar to Gilbert's dynamic equilibrium (Gilbert, 1877). Changes in topographic form resulted from changes in the forcing conditions, and responses to perturbations were fast enough to restore a dynamic steady state adjusted to the new boundary conditions. He explicitly viewed landscapes as spatial structures with time-invariant forms (under steady forcing). A major assumption is that hillslopes and streams are strongly coupled. Stream incision energizes hillslope processes which respond rapidly to perturbations in the stream network. This view of 'adjustment' between hillslopes and channels leads directly to stability in drainage basin structure. Spatially uniform erosion rates imply a non-evolving topography.

Field Studies of Steady State Landscapes

The possibility that erosion on average keeps pace with uplift (steady state) has been demonstrated for several field sites. Meigs et al. (2002) have shown that on average erosion is balancing uplift of the Santa Monica Mountains in southern California. They utilized reconstructions of folded sedimentary strata, timing of deformation, and current topography to obtain long term erosion rates. They note that field evidence exists for drainage capture, a sign of landscape instability, despite the presence of a sediment flux steady state balance (eroded mass leaving the system balances mass input from uplift). The South Island, New Zealand has experienced longer term tectonic collision and rock exhumation, and mineral cooling histories suggest that a long term balance between exhumation and erosion has been reached (Batt and Braun, 1999). The Olympic Mountains in the Pacific Northwest also exhibit mineral cooling ages and patterns consistent with a long term balance between erosion and exhumation (Brandon et al., 1998; Batt et al., 2001; Willett and Brandon, 2002). For tectonically quiescent regions, such as the Appalachians, erosion rate studies have demonstrated both moderately uniform (Matmon et al., 2001) and variable erosion rates (Harbor, 1996), attributed to stream piracy. Other field studies have documented rather substantial variability in

5

erosion rates, even in adjacent sub-basins (Riebe et al, 2000). Several examples of stream capture in natural settings exist: Spain (Casas-Sainz and Cortes-Gracia, 2002; Mather et al., 2000); The Blue Ridge of the central Appalachians (Harbor, 1996); James River, Appalachians (Erickson and Harbor, 1998; Ries et al., 1998); Swiss and Western Alps (Frisch et al., 1998); Black Hills, USA (Zaprowski et al., 2001); and the northeast Basin and Range, USA (Harbor, 1997). While many of these regions are not experiencing active tectonic uplift, and hence, can not be considered as steady state landscapes, nonetheless, the presence of drainage instability is suggestive that drainage basins may not be driven to stable forms.

Theoretical models of stream incision (described in detail below) and long term erosion offer a useful starting point for deducing dominant erosive processes at various scales within a drainage basin (Snyder et al., 2000; Lague et al., 2000), as well as offering a way of accessing possible changes in landscape form to changes in climatic and tectonic forcing (Moglen and Bras, 1995; Whipple and Tucker, 1999; Whipple, 2001; Stark and Stark, 2001). Insights into the response time of channel networks and hillslopes to changes in forcing have been obtained from these studies, which focus attention on how information is propagated through an eroding drainage basin, a critical issue for understanding dynamic behavior in drainage basins over intermediate to long time scales. What remains unclear, despite excellent research into erosional variability and landscape dynamics, is the degree to which erosional variability is controlled by unsteady forcing from climate and tectonic change, by lithologic variability within the drainage basin, or by intrinsic interactions between hillslope erosion and channel incision.

In summary, recent field tests of the stream power erosion law have focused on calibration of the parameters in the erosion law and model validation, with a nod to expected dynamic behavior of the law when perturbed by uplift. No studies have been conducted to test the fundamental stability of current erosion laws as implemented in numerical landform models. The stationary state of numerical landscapes under steady state uniform forcing could result 1) from the possibility that drainage basin structures are inherently stable structures; and/or 2) from the *implementation* of erosive processes in

numerical schemes. The stability exhibited by numerical models provides support for the concept of a landscape at dynamic steady state, where erosion rate is invariant across a landscape over longer time scales (Hack, 1960). Some researchers have concluded that drainage basins are inherently stable, and represent structures that have minimized energy expenditure throughout the network (Glock, 1931; Rinaldo et al., 1992). The strong negative feedback between erosion rate and relief and slope (that is, increased relief forces higher erosion rates, which in turn lower relief) has been hypothesized to drive landscapes under steady forcing to a stable planform geometry (Willett and Brandon, 2002).

Experimental Studies of Landform Evolution

Physical experiments provide an additional means of observing drainage basin scale erosion over long times. They allow control over substrate properties, initial surface conditions, forcing from uplift and rainfall, and boundaries of the drainage basin system. What follows is a review of published experiments involving erosion in small scale drainage basins.

Parker (1977) employed a rectangular flume (9.1 x 15.2 x 1.8 m) with a single outlet, and applied rainfall (0.83-2.64 in/hr, or 5.8-18.4 μm/s, modal droplet size ~ 1.52 mm, maximum size 3.71 mm) over a substrate composed of silt/clay particles mixed with sand (D_{50} = 3.75 mm). This experiment monitored planform evolution of a drainage basins after stepwise lowering of base level. The erosional response of the basin following base level fall exhibited an exponential decay of the initial perturbation, with increasingly diminished erosion over longer times. In these experiments, a steady state landform is achieved only after the base level drop has propagated through the system, and the erosion rate has decreased to nil. Parker observed changes in drainage density after the network had completely extended to the edges of the basin. Knickpoints in streams were observed as transient features which at times disappeared and at others coalesced to form larger knickpoints. Eroded material from knickpoint propagation was often deposited just downstream of the migrating knickpoint. Parker noted cyclic sediment yields at the outlet following the single stepwise base level drop, and considered this response to be a result

of sediment storage caused by out of phase erosion between hillslopes and streams (i.e., complex response, Parker, 1977). He acknowledged that this cyclicity made it difficult to obtain a simple relation between water discharge and sediment flux from the basin. Parker's work suggests that internal dynamics of the system generate spatially non-uniform erosion under uniform conditions of rainfall when base level is perturbed.

Czirok et al., (1993) explored the evolution of topography by sprinkling rainfall (1500-3000 cm^3/min [sic]) over a smoothed 65 cm linear ridge of silica sand (D_{50} = 150 μm) mixed with organic soil (approximately 1:1), piled on a table. They note that erosion was dominated by landslides of widely varying sizes and entrainment of particles by surface runoff. They measured surface roughness from digitized photographic profiles, and showed that roughness in the model profile compared favorably to the Dolomites in Italy, though the average slope of the Dolomites was substantially larger than their experiment. They also tried a variety of substrates. Blocks of clay and sugar developed roughness on 10-20 cm length scales, much longer than roughness of ~1 mm that they obtained for soil and sand. They suggested that the fractal character of mountainous landscapes was due to surface runoff and the presence of landslides over a range of scales.

Ouchi (1996) constructed a similar test to Czirok et al. (1993). His experiment focused on the evolution of relief. The physical experiment consisted of a 1 x 1 m square table loaded with a block of sediment (D_{50} = 0.12 mm; mixed 15:1 by weight kaolinite) 20 cm high. He applied rainfall at the rate 25-50 mm/hr (7-14 μm/s) for 192 hours, and measured topographic profiles with a point gauge at nine times during the run. He documented initial dissection of the original plateau, with an increase in roughness, followed by exponential decay of relief.

Hancock (1997) developed a physical erosion facility (1.44 x 1.46 x 0.5 m) to explicitly test a numerical landform model with an experimental erosion facility. This experiment focused on building a physical apparatus with suitable network forming capabilities, developing digital elevation models from stereophotographs of the miniature landscape, calibrating the numerical model, and comparing spatial statistics of the output from the experimental and numerical simulations. In this experiment, uplift was

8

simulated as a step-wise drop in base level at the outlet to the basin, similar to Parker's (1977) experiments. Rainfall rates were varied from 8 to 33 μm/s (52 to 118 mm/hr), with droplet size < 270 μm. The substrate consisted of fly ash, a byproduct of coal combustion, with a D_{50} = 81 μm. It was noted that while the qualitative form of the experimental basin differed substantially from the numerical model of Willgoose et al. 1991, certain spatial statistics such as cumulative area draining through a point, the area-slope relationship (values for α, in S = k A^{α}, range from 0.02 to -0.27), and hypsometry compared moderately well. It was further noted that the numerical model did not capture the hillslope form and evolution of the physical experiment very successfully. This work also documented some of the difficulties in developing an experimental facility that suitably tests a numerical model. For instance, the assumption of uniform erodibility was moderately violated by the experimental landscape due to armoring of the surface with larger particle sizes.

Recently, physical experiments that force the landscape with continuous uplift and rainfall conditions have been developed (Hasbargen and Paola, 1998; Hasbargen and Paola, 2000; Crave et al., 2000; Ouchi, 2001; Lague and Davy, 2002; Hasbargen and Paola, 2003). The erosion facility of Crave and Lague consisted of a small rectangular box (0.2 x 0.3 x 0.09 m) containing loess (D_{50} = 50 μm, with 10 % clay, 10 % $CaCO_3$, 80 % silt), with a rainfall generating device above the facility (droplet size 8 μm, rate of 90 mm/hr or 25 μm/s). Sediment and water exited the facility along each edge of the box. Uplift was accomplished by pushing the box past fixed borders using a motor-controlled infinite screw device (rate of 0.1-10 cm/hr, or 2.8-28 μm /s). Hence, each side of the box represents an infinite flux boundary with a constant incision rate. They documented landform evolution from an initial plateau to dissection at constant uplift rate, then a decline in elevation as uplift was shut off. From gridded elevation data, they calculated the exponent (α) for the relationship between upstream area and slope ($S = k\,A^{-\alpha}$) as 0.1, and note that this value is close to the value (0.18) for natural colluvial channels, debris flows, or unchanneled valleys in the Siwalik Hills of India (Lague and Davy, 2002),

though somewhat lower than values for natural alluvial rivers (-0.3 to -0.8) (Lague et al, 2000), and badlands (-0.19) (Howard and Kirby, 1983). Their experiment was too small for truly dendritic drainage patterns to develop, and hence their results are restricted to the evolution of a model hillslope at constant forcing conditions (Lague and Davy, 2002).

The above review of physical experiments demonstrates that small drainage basins can be developed in a variety of substrates (grain sizes range 50 to 3750 μm; varying concentration of sand and clay), and a wide range in rainfall rates (2.8 to 33 μm/s) and precipitation droplet sizes (8 to 3710 μm). Drainage basin surface area varies several orders of magnitude between these experiments, from 0.06 to 138 m^2. Dendritic drainage basins of at least order 3 have been documented for basins down to 1 m^2 (Hancock, 1997).

None of the physical experiments discussed above were designed to test the effects of prolonged constant uplift on drainage network behavior. Long term constant forcing allows us to monitor the internal process interactions and systematic behavior that develops in a landscape in the absence of *changes* in external forcing conditions. Intrinsic variability has been well-documented for braided and meandering river systems, depositional systems such as delta lobes, and river avulsion, but has remained elusive in drainage basin scale erosional studies. This thesis was designed to address this deficiency.

In summary, physical experiments of drainage basin erosion have captured several key elements of natural drainage basins: dendritic drainage networks with well-developed branching structures; surface runoff based erosion; hillslope failures of various sizes; upstream propagating knickpoints in channels; and temporary deposition in valleys. Elements of natural landscapes that are neglected in the physical experiments are the effects of chemical weathering, vegetation and biologic activity, fire, earthquakes, freeze-thaw, to name a few. Physical experiments can offer rigorous tests for numerical formulations of landscape erosion. No inherent scale exists in the stream power model. Grain size is not explicitly treated, and flow conditions are assumed to be uniform and steady. Hence, a physical experiment under steady forcing conditions with a uniform substrate represents a suitable test of the current landscape erosion models.

Numerical Models of Landscape Scale Erosion

A variety of erosion models have been developed in recent years, and while they differ in the degree of simplification of the erosional processes, they all employ an assessment of the controls on mass transport rates in landscapes. In general, erosion is controlled by the resistance of the substrate to applied surface and body forces, and this resistance is in turn a function of rock properties (crystalline structure and chemistry, rock strength or cohesion), vegetative cover, and degree of saturation. The nature of the applied forces varies widely across a landscape: the scratching paws of burrowing animals; the impact of rain drops; the pounding of animal hooves; the torque of bending trees under the wind's impulse; soil expansion during saturating events and freeze-thaw; episodic hillslope failures of oversteepened slopes; the thrashing torrents of streams; and the grinding mass of a sliding glacier, to name a few. The rate of disintegration of crystalline bedrock to smaller particles also sets a limit on the availability of transportable material. Simplification is required at some level to obtain solutions to mass transport through the network.

A pioneering effort in developing a numerical landscape model was developed by Smith and Bretherton (1972), who investigated drainage basin stability with a numerical model of processes operating in drainage basins. They assumed: "1. A drainage basin may be represented as a mathematical surface. 2. The principle of the conservation of mass is applicable to this surface. 3. The transport of sediment at any point on the surface may be adequately described by some function of the local slope and the local discharge of water."(Smith and Bretherton, 1972). Stated formally, sediment transport takes the form $q_s = \mathrm{F}(q, S)$, where q_s is the sediment flux, q is the discharge per unit width, and S is the local topographic gradient, and when placed into a numerical topographic lattice, an erosion rate law takes the general form $\partial z / \partial t = k\, q^m S^n$, where z is elevation above datum, t is time, k accounts for resistance to erosion, and the exponents m and n are model parameters that encapsulate information on the erosion process. They outline a few

implications of this formulation. 1) Concave surfaces are always unstable, that is, flow will always form channels on the surface. This follows from noting that the smallest perturbations on concave surfaces also grow the fastest. 2) Convex surfaces or convex-concave surfaces can be stable. They identify two feedback mechanisms in this model, one that increases instability on concave surfaces (positive feedback) and one that dampens perturbations on convex surfaces (negative feedback). This works only if there is a critical length from the drainage divide to some inflection point on the hillslope profile at which concavity begins. They strongly urge physical experiments be done as tests of the hypothesis that a single transport law is applicable to drainage basin development and evolution.

In the last decade, several models similar in spirit to Smith and Bretherton (1972) have been employed in numerical evolving grids. The simplest of the models assume 1) a uniformly resistant but erodible substrate; and 2) transport down the steepest slope by a process that is not limited in the amount of material it can carry (Willgoose et al, 1991; Chase, 1992). The transport law is fundamentally based on gravitational dominance over the flow field, with adjustments possible for establishing width, depth, and velocity from slope, convergence and continuity. Surprisingly, this formulation develops networks with branching structures similar to natural drainage patterns (Leheny and Nagel, 1993), and even captures the evolutionary behavior of the network envisioned by Glock (1931). Limiting the capacity of the process does not alter the solution significantly (Leheny and Nagel, 1993). These models reach a static steady state landscape under steady forcing from uplift and climate.

The model formulations themselves have evolved, and incorporate treatments of: 1) a spatially varying substrate resistance (Moglen and Bras, 1995); 2) closed form expressions for stream flow velocity, depth, and pressure through the network (Kramer and Marder, 1993; Howard, 1994; Loewenherz-Lawrence, 1994); 3) nonuniform saturation on hillslopes (Dietrich et al., 1993); 4) a range of grain sizes for transportable material (Howard et al., 1994); 5) factors controlling hillslope instability, such as soil thickness, level of saturation, and groundwater flow (Dietrich et al., 1993); 6) coupling

erosion with tectonic and climatic forcing (Beaumont et al., 1992; Howard, 1994); 7) erosion rate is treated as a nonlinear function of shear stress and sediment concentration (Sklar and Dietrich, 1998); and 8) explicit treatment of both horizontal and vertical deformation (Willett et al., 2001).

Models become increasingly less testable with increasing complexity, due to the number of parameters requiring calibration, the difficulty in obtaining functional relationships between applied forces and resistance, and the large number of solutions to the equations. Validation has largely been restricted to comparison with relief, stream profiles or some combination of geometric statistics of natural drainages, such as the number of streams of given order (Horton's law), the length of the trunk stream divided by basin area (Hack's law), the hypsometric curve, plots of contributing (upstream) area against local stream slope, and upstream area draining through a point at a given distance from the basin outlet (the width function). Shreve (1966) showed that the geometric increase in number of streams for decreasing order could be explained by any topologically distinct random channel network, thus discounting Horton's law as a useful measure. The area-slope relation ($S = k\,A^{-\alpha}$) for natural drainage basins has been used to yield the ratio of exponents in the stream power erosion law ($\partial z/\partial t = k\,q^{m}\,S^{n}$), but evaluating the magnitude of individual exponents has remained elusive, particularly the exponent on slope (Whipple and Tucker, 1999; Snyder et al., 2000; Lague and Davy, 2002). Further, the constant of proportionality, k, in the stream power law, appears to be variable in natural settings (Snyder et al., 2000). This coefficient buries information on rock resistance, channel width, runoff, and mass transporting processes, such as debris flows. Attempts to verify that a single process law adequately models landscape scale erosion have not been very successful (Snyder et al, 2000).

Additional work on the dynamics of the stream power law, that is, landscape response to perturbations in climate or tectonics, has also been accomplished. From theoretical considerations, perturbations in uplift rate propagate as a kinematic wave through the network, with the propagation rate set by upstream area and local topographic gradient (Whipple and Tucker, 1999; Snyder et al., 2000; Stark and Stark, 2001). The focus of

these studies has been on the response time of the landscape, that is, the time required for a perturbation to propagate through the drainage basin. In general, response times of natural landscapes are long enough (on the order of 100,000 years or more) to span periods of substantial climate change, effectively hampering the development of steady state topography in natural landscapes, as well as complicating studies in natural drainage basins. Further, application of the stream power-law to digital elevation grids of natural drainage basins has demonstrated that predicted erosion rates vary substantially across landscapes experiencing long-term uplift (Finlayson et al., 2002).

Numerical Model Formulation, Evolution, And Stability

Excellent outlines of the formulation of the stream power erosion law are given in Howard (1994), Whipple and Tucker (1999), and Snyder et al. (2000). The development is recapitulated here.

The volumetric rate of erosion per unit area is hypothesized to be a power law function of fluid shear stress acting on the bed (τ_b):

$$\varepsilon = k_b \; \tau_b^{\alpha}, \tag{1-1}$$

where ε is erosion rate in volume per unit bed area per unit time, k_b is a dimensional constant that represents the resistance of bedrock to erosion. The parameter, k_b, has been treated as a variable by some authors, with a dependence on sediment concentration (Sklar and Dietrich, 1998). The value of the exponent α ranges from 1 (Howard and Kerby, 1983) for a weak substrate to 3 for impact driven erosion into bedrock (Foley, 1980; Hancock et al., 1998; Whipple et al., 2000).

Assuming uniform and steady flow, conservation of momentum yields the bed shear stress (τ_b), given by:

$$\tau_b = \rho \, g \, S \, H = \rho \, C_f^{1/3} \, V^2 \quad , \tag{1-2}$$

where ρ is fluid density, g is gravitational acceleration, S is water surface slope, H is depth normal to the bed, C_f is a dimensionless friction factor, and V is velocity. If the flow through a stream network is steady and uniform (justifiable for a long term average of a large number of storm events across a landscape), then the local average discharge is given by:

$$Q = k_q A^c, \tag{1-3}$$

where k_q is a dimensional constant, relating rainfall with runoff efficiency, and A is upstream area. Empirically-based downstream hydraulic geometry for alluvial streams provides a relation between discharge, Q, and channel width (w) downstream:

$$w = k_w Q^b = k_w [k_q A^c]^b = k_w k_q^b A^{bc}. \tag{1-4}$$

The conservation of water discharge provides:

$$Q = w H V = k_w k_q^b A^{bc} H V. \tag{1-5}$$

To remove H from the system of equations, set

$$g S H = C_f^{1/3} V^2, \text{ and solve for D:}$$

$$D = [C_f^{1/3} V^2] / [g S] \tag{1-6}$$

Since $V = Q / [D w]$, and $Q = k_q A^c$, and $w = k_w k_q^b A^{bc}$

$$V^2 = [Q / H w]^2 = [k_q^2 A^{2c}] [k_w^{-2} k_q^{-2b} A^{-2bc}] D^{-2}$$

then, substituting V^2 into (1-6) yields:

$$D = [C_f^{1/3} k_q^2 A^{2c} D^{-2} k_w^{-2} k_q^{-2b} A^{-2bc}] / [g S] \tag{1-7}$$

Combining exponents:

$$D = [C_f^{1/3} k_q^2 A^{2c(1-b)} D^{-2} k_w^{-2} k_q^{-2b}] / [g S] \tag{1-8}$$

multiplying both sides by D^2

$$D^3 = [C_f^{1/3} k_q^2 A^{2c(1-b)} k_w^{-2} k_q^{-2b}] / [g S] \tag{1-9}$$

taking the cube root of both sides:

$$D = [C_f^{1/9} k_q^{2/3} A^{2/3c(1-b)} k_w^{-2/3} k_q^{-2/3b}] [g^{-1/3} S^{-1/3}] \tag{1-10}$$

Substituting (1-8) into (1-2):

$$\tau_b = \rho g S [C_f^{1/9} k_q^{2/3} A^{2/3c(1-b)} k_w^{-2/3} k_q^{-2/3b}] [g^{-1/3} S^{-1/3}] \tag{1-11}$$

again, combining like variables

$$\tau_b = \rho g^{2/3} S^{2/3} k_w^{-2/3} k_q^{2/3(1-b)} C_f^{1/9} A^{2/3c(1-b)} \tag{1-12}$$

and finally, inserting (12) into (1) yields

$$\varepsilon = k_b \tau_b^a = k_b \rho^a g^{2/3a} S^{2/3a} k_w^{-2/3a} k_q^{2/3a(1-b)} C_f^{1/9a} A^{2/3ac(1-b)} \tag{1-13}$$

which can be simplified to

$$\varepsilon = K A^m S^n \tag{1-14}$$

where

$$K = k_b \, \rho^a \, g^{2/3a} \, k_w^{-2/3a} \, k_q^{2/3a(1-b)} \, C_f^{1/9a},$$

$$m = 2/3ac(1-b)$$

$$n = 2/3a$$

Equation (1-14) represents the general form of erosion as a function of bed shear stress, or unit stream power, and is commonly called the stream power law. Combined with a term for rock uplift, a general equation that describes the time evolution of an eroding landscape becomes:

$$\partial z/\partial t = U - \varepsilon = U - K A^m S^n \tag{1-15}$$

Numerical Model Simulations

What follows is a demonstration of a numerical landscape evolution model based on the stream power erosion law (modified after Howard, 1994):.

$$\partial z/\partial t = U - \varepsilon = U - K_1 Q^m S^n + K_2 S \tag{1-16}$$

where Q is discharge, and other terms as detailed above. Discharge was This equation is approximated by

$$\Delta z_{t+1} = \Delta z_t + \Delta t \, (U - K_1 Q^m S^n + K_2 S) \tag{1-17}$$

where Δt is an arbitrarily small time step, selected such that incremental changes in elevation are small, and numerical stability is ensured for each iteration. This erosion law (Equation 1-17) operates within a regularly spaced elevation field, starting with an initial randomized surface. Each grid node (i.e., cell) represents a unit area, with cell length and width set arbitrarily. At each time step, an increment of uplift is added to the elevation of each cell. Then a specified quantity of rain is assigned to each cell. The slope magnitude is then computed between a cell and each of its 8 adjacent neighbors. Slope is computed as $S = (z_i - z_j)/((x_i - x_j)^2 + (y_i - y_j)^2)^{1/2}$. The steepest slope and direction are recorded for each cell. Then, each cell is visited again, and flow (rainfall * cell area) is routed downslope through the grid to the nearest depression or to the outlet of the basin. The amount of flow that passes through each cell is recorded. Once discharge (total flow through a cell) and the steepest descent slope are known, the amount of erosion is computed using the third term ($\Delta t \, K_1 Q^m S^n$) on the right hand side of Equation (1-17). Mass is not explicitly conserved in this formulation. The assumption is a detachment

limited system, with no deposition of eroded material, and the streams never reach their sediment carrying capacity. A global balance between uplift and erosion is attained, however, if the model is allowed to run for a long enough period of time.

The diffusive term included in the erosion law encapsulates processes that move mass locally, such as rain splash, soil creep, bioturbation, or slope failures. Diffusion is calculated by visiting each cell (cell$_i$), computing steepest descent among the eight adjacent neighbors (cell$_j$), and lowering the elevation of cell$_i$, and raising the elevation of cell$_j$ according to slope magnitude. An alternative method of computing diffusion was implemented, where the change in elevation of cell$_i$ is computed as the sum of slopes to adjacent neighbors. Both methods smooth the surface. An arbitrary coefficient (K_2) scales the magnitude of mass movement. Mass is conserved between cells (what one loses the other gains). An additional novel method of incorporating diffusion involved aspect-driven diffusion, where diffusion varies from nil to a maximum, depending on the angular difference between a hillslope aspect direction and a specified (arbitrary) direction. Aspect-driven diffusion accounts for increases in mass movements due to microclimate, such as rain driven by a persistent wind pattern.

Several numerical experiments were conducted, where the coefficients K_1 and K_2 were varied, or the uplift (U) was varied, or the boundary condition was varied, with either one edge of a rectangular grid treated as the outlet, or with an elliptical no flux boundary except for a single outlet cell (designed for comparison to the experimental erosion facility, which will be described later). Additional terms were added to the erosion law to account for aspect driven diffusion, spatial and temporal variation in rainfall, and temporal variation in uplift. Time series of elevation were extracted from each run to verify that the stream power erosion model developed stable, uniformly eroding landforms (Howard, 1994; Kooi and Beaumont, 1996). The addition of diffusion to the erosion law, and variation in rainfall patterns and gradually varied uplift did not destabilize the landform. These simulated landscapes all go through some evolution after erosion has balanced uplift globally. Howard (1994) noted that his models completely stabilized after eroding through ~3 H_r, though other modelers note stability after ~1 H_r

(Greg Tucker, pers. comm., 2001). Adjustments in the numerical landscape inevitably lead to a more stable structure. Apparently, downstream accumulation of flow overwhelms and dampens perturbations.

Before proceeding with examples of numerical simulations, pertinent scales to facilitate comparison between numerical, experimental, and natural landscapes are here introduced. A horizontal length scale L and vertical length scale H_r are defined in the following fashion:

$$L \sim A^{1/2}$$

(1-18)

$$H_r = Z_{max} - Z_{min}$$

(1-19)

where A is drainage basin area, Z_{max} is the maximum elevation in a steady state drainage basin above datum, and Z_{min} is the minimum elevation above datum. These measures, while not directly implemented in the erosion model formulated above, will appear in subsequent sections where scale is pertinent.

Figure 1-1 (p. 20) displays local adjustments prior to attaining a stationary network, but after a global balance between uplift and erosion has been reached. During this simulation, a single long narrow valley flanked by higher ridges in the center of Figure 1-1 A 'closes' from the valley head downstream in subsequent images (1-1 B, C, D). The eroded distance between sequential grids is 0.33 H_r. Upon closure of this narrow valley, the landscape is stabilized, and ceases to evolve further.

Figure 1-2 (p.21) demonstrates the effect of diffusion on landscape form. Note that the diffusion coefficient ($K_2 = 0.1$) used in the simulation portrayed in Figure 1-2 is much larger than that used in Figure 1-1 ($K_2 = 0.0005$). Small scale roughness (i.e., channels) visible in Figure 1 are absent in Figure 2. See the included CD-ROM for animations of numerical model runs (SupportingData\Index.html, and click on 'Numerical model simulations').

These numerical results provide the prediction that will be tested with a physical experiment: Do physical eroding drainage basins under steady forcing exhibit such

stability? In order to test the erosion model with an experimental erosion facility, several key conditions have to be met. These include runoff based erosion, a homogeneous substrate, and steady uniform forcing from rainfall and uplift. This thesis documents the construction of an erosion facility that allows for steady forcing, and mimics the dominance of surface runoff based erosion contained in theoretical landscape erosion models. The experimental erosion facility developed 3-5 order drainage basins that eroded through several units of relief at demonstrably stable forcing, and thus represents a first order test of the uniformly eroding drainage basin hypothesis. It is worth noting that these physical drainage basin experiments were the first of their kind to enforce continuous uplift for long periods of erosion.

A battery of runs (seven runs are presented here) were conducted at varying rainfall and uplift rates to ensure that results were not dependent on some special conditions. In addition to providing a first order test of the stream power model, this study stands as a sensitivity study of the dependence of landscape form and erosional dynamics on forcing conditions. They offer an unprecedented view into the temporal dynamics of an eroding drainage basin, and open up new research possibilities into process interactions of eroding landscapes.
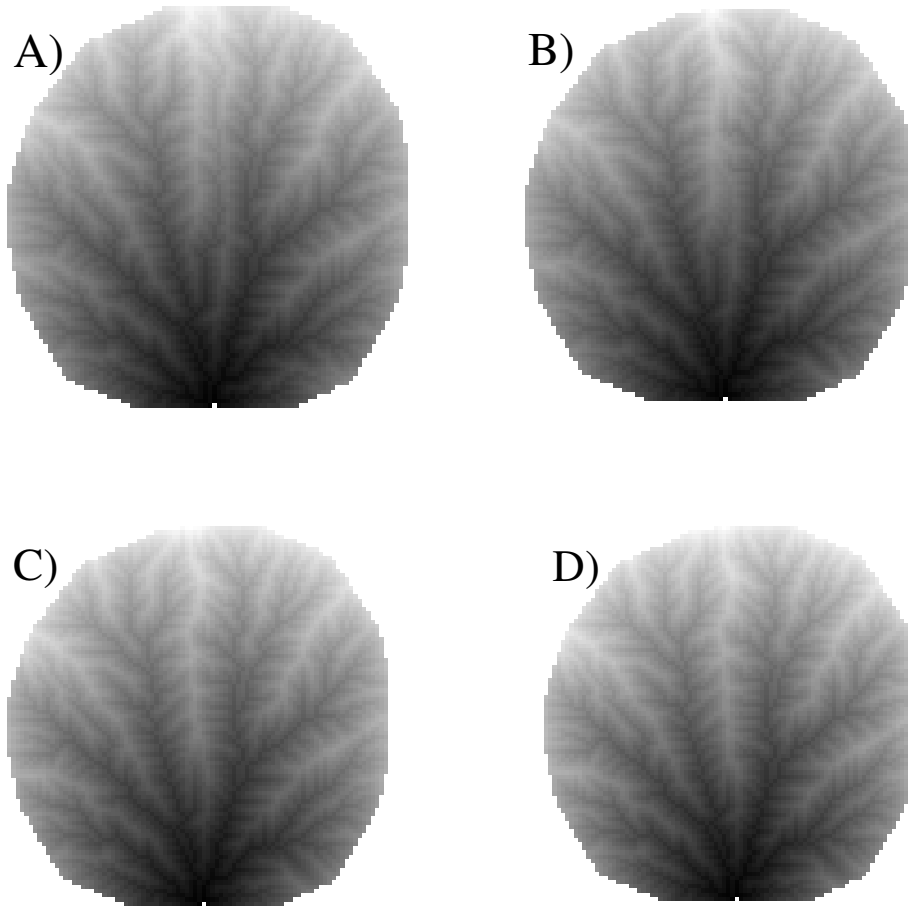
Figure 1-1. Time series elevations demonstrate valley closure in a numerical erosion model. Images are gray-scale elevation maps (white = highs, dark = lows). Width of each image is 89 cm (1.1 L). Grid resolution is 1 cm spacing. Range in elevation for each image is 16 cm (0.2 L = 1 H_r). A) A long narrow linear valley separates main ridges in the center of the image. Subsequent images show the closing of this valley from top to bottom. The rest of the landscape appears unaffected by the divide reorganization. Eroded distance from (A) to (D) is 16 cm (16 cm = 0.18 L, or 1 H_r). Input parameters to the numerical model [$\Delta z_{t+1} = \Delta z_t + \Delta t\ (U - K_1\ Q^m\ S^n + K_2\ S)$]are $K_1 = 0.001$, $m = 0.25$, $n = 1$, $K_2 = 0.0005$, $\Delta t = 50$ s, uplift rate (U) = 0.0001, and rainfall rate = 0.001 (maximum discharge at the outlet = 6.6 cm^3/s). Units of uplift and rainfall are in mm/s.
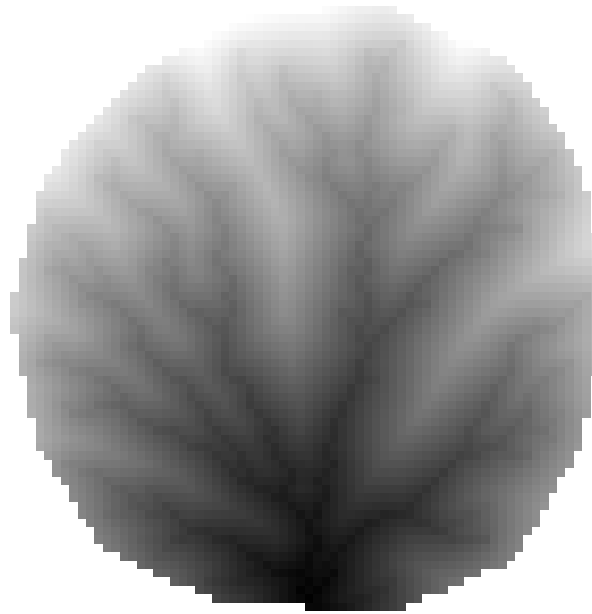
Figure 1-2. Effect of diffusion on numerical landscape. Hillslopes are smooth, and streams do not advance as far up the hillslope. Width of image is 89 cm (1.1 L). Grid resolution is 1.25 cm spacing. Range in elevation for is 14 cm (14 cm = 0.17 L = 1 H_r). Eroded distance since dissection is 1.6 H_r (22 cm). Input parameters to the numerical model [$\Delta z_{t+1} = \Delta z_t + \Delta t (U - K_1 Q^m S^n + K_2 S)$]are $K_1 = 0.001$, $m = 0.25$, $n = 1$, $K_2 = 0.1$, $\Delta t = 50$ s, uplift rate (U) = 0.0001, and rainfall rate = 0.001 (maximum discharge at the outlet = 6.7 cm^3/s). Units of uplift and rainfall are in mm/s.

Chapter 2

Erosion Facility Description, Data Collection, and Run Conditions

This chapter documents the construction of an erosion facility, factors involved in the choice of substrate, calibration of rainfall distribution over the facility, measurement of fluxes leaving the erosion facility, and measurement of topography using stereophotography and time lapse video.

Erosion Facility Design

The physical experiment consists of an oval tank approximately 1m in diameter (surface area of 6470 cm$^{2)}$ and 1m deep with a single outlet dammed by a motor-controlled gate. The motor operates continuously during each run, and drops the outlet at a slow constant rate, in effect uniformly 'uplifting' the basin relative to base level. The height-width ratio of the tank permits relative uplift of 3-6 times the instantaneous steady state drainage relief (H_r). A mist apparatus sprinkles rain (droplet size < 200 μm) over the basin to generate runoff. Two oscillating 22.5 cm diameter fans are used to break up persistent air circulation patterns and promote mixing of rainfall in the facility. See Figure 2-1 (p. 37) for a schematic cross section and Figure 2-2 (p. 38) for photographic views of the erosion facility. A rigid plastic wall encloses the basin, shielding the apparatus from air currents in the laboratory.

In initial tests of suitable conditions to generate model drainage networks, several variables were observed that could affect the formation and stability of the experimental drainage network. These include rainfall rate, cohesion and grain size of the substrate, and rate of base level fall.

The rainfall rate and droplet size affect the development of a model drainage network in the following fashion. Very high precipitation rates (on the order of 40 μm/s) lead to dominance of sheet flow in transporting material out of the basin. Surfaces are smoothed, and drainage density decreases drastically. See Figure 2-3 (p. 39) for a photograph of the ground surface. Large raindrops greatly increase instantaneous diffusion around the drop, both by scattering grains on impact and transferring momentum to the substrate. Grain to grain cohesion weakens, and the region around the impact is mobilized at a lower slope.

The effect of increasing the magnitude of local diffusion causes a reduction in the drainage density. Every effort was made to reduce drips from the facility superstructure.

Grain size limits the fine-scale texture of the model. Initial tests of suitable grain sizes showed that channels on the order of 5-10 grain diameters can develop for grain sizes in the 15-100 μm range, yielding networks with a large number of streams relative to the size of the basin, with continuous interfluve distances on the order of 10^1 to 10^4 grain diameters. For 45 μm silt, 22 grains occupy a linear mm. Current data collection methods can capture distances in the sub-mm range. It is not the purpose of this thesis to investigate single grain interactions, so higher resolution is not required for the thesis to succeed. Grain size also forces a change in the sediment transport mode in model streams. Hancock (1997) noted armoring of the surface due to larger grains in his experiments.

Grain to grain cohesion can be controlled by the presence of a bonding agent in the interstices of the particles. Cohesion increases bulk substrate strength. Larger pieces of the substrate act as a unit with increasing cohesion. Cohesion directly reduces the probability of failure, since a larger shear stress is required to overcome the frictional strength of the material. This effect allows higher relief to develop. Kaolinite was used as the cohesive agent. Cohesion can be varied by changing the concentration of the kaolinite in the substrate. Initial tests indicated that weight ratios of less than 5% (kaolinite/silt) produce landforms eroded by stream networks and hillslope failures.

Uplift rate directly controls the energy potential applied across the basin, and affects slope dependent processes such as hillslope failure and stream erosion. Higher uplift rate energizes both stream transport as well as slope failure. Streams can erode further up the valley side slopes, but whole hillslopes are more likely to fail into rapidly incising second and third order streams. Low order stream incision can be overwhelmed by longer length scale mass transport movements along failures.

The desired experimental network is one spanning several stream orders, and is measurable with current imaging technology. The above variables can be adjusted to yield a suitable network, with a series of runs performed to demonstrate the effects of each on erosional behavior.

Overview of Run Conditions

For each experiment, silica silt ($D_{50} = 45$ μm) is mixed with kaolinite (100:1 by weight) and water in a cement mixer, poured into the basin, and allowed to settle overnight. The dry bulk density of the substrate was computed by recording the total mass of sediment mixed for each run, and measuring the filled depth and surface area of the basin. This yields an average value of 1.75 g/cm^3 , with modest variation between runs ($\pm$ 0.1 g/cm^3). Settling produced a flat surface pocked with small sediment volcanoes (< 4 cm diameter) generated by groundwater overpressuring during loading. The initial runoff pattern on this surface was essentially random, though directed toward the outlet. A typical initial surface is depicted in Fig. 2-4 (p. 40), after draining the reservoir and before the inception of erosion.

Seven runs were conducted at varying rainfall and uplift rate conditions. Each run began by starting the motor-controlled outlet and turning on rainfall. The streams incised from the outlet and extended to the edges of the basin. Trunk streams near the outlet developed knickpoints that migrate upstream, frequently triggering hillslope failures. The outlet location (base level), stereophotographs, time lapse video, and effluent flux rates at the outlet were recorded for each run.

The runs were conducted at extended periods of time under steady forcing from base level fall and rainfall (see Table 3-2, p. 116) for run conditions, and Chapter 3 for detailed run descriptions). As with most physical experiments, perfect uniformity was not possible. Water pressure in the laboratory water lines fluctuated on occasion, and was particularly noticeable for run 5. No statistical tests of pressure fluctuations and its effect on rainfall were conducted. A pressure regulator that limited pressure to less than 35 psi was installed in the water supply for runs 2-7 to place an upper limit on fluctuations. Other minor perturbations include minor stick-slip sliding of the motor-controlled outlet; rehydration of runs 1 and 7 after being shut down overnight; and possibly variable substrate resistance due to incomplete mixing of sediment and kaolinite. Measured displacements from stick-sliding were never larger than 1 mm, and were typically on the order of 0.1 mm. Runs 1 and 7 were turned off overnight, and the substrate dehydrated.

Sediment yields often overshot the steady state flux upon rehydration, but rapidly returned to a steady state condition, usually within 1 hour of start up (see sediment flux for Run 1, Fig. 2-15, p. 54).

The ratio of average rainfall/uplift mass flux rate, r/u, or the water-to-rock ratio, ($r/u = r\, \rho_r / u\, \rho_s$, where r is rainfall rate, u is uplift rate (both in volume per unit area per time), ρ is density, and r and s refer to rainfall and substrate respectively), is a simple and useful framework by which to compare the various runs. As an initial hypothesis, a large r/u should develop a basin with a large number of streams, as surface runoff dominates erosional processes. A small r/u should develop a landscape with fewer streams, as mass flows dominate erosion at smaller scales. The various experiments were meant to explore the topographic form and dynamic behavior of the model landscapes for a range of uplift and rainfall conditions. Substrate properties remained the same between each run. As such, they should be taken together as a sensitivity study of experimental landforms under steady forcing.

Rainfall Calibration

As mentioned above, rainfall droplet size can have a pronounced effect on experimental topography. A variety of mist generating nozzles were tested. The effects of mister droplet size, while not directly measured, were observed, and misters with droplets that displaced material on impact, or developed excessive drips were rejected. Two different styles of misters were used for the runs reported in this thesis. One employed a jet that impinged on a flat plate, generating a radial pattern. This style of mister was used for runs 1 through 4. Runs 5 and 6 used two 4-nozzle arrangements, separated by 15 cm. The nozzles generated laterally directed cones of spray, and when arranged in 4 orthogonal directions, developed a moderately uniform rainfall distribution. A great deal of effort was expended in arranging the misters in different locations, and measuring rainfall spatial distributions. A uniform spatial distribution of rainfall is very difficult to obtain with fixed mister locations, because vertical air circulation cells develop in the enclosed facility. Ultimately, two oscillating fans were utilized to break up persistent circulation patterns that developed in the erosion facility.

Prior to each run, small pans were placed on a platform on top of the erosion basin, and rainfall was collected for varying lengths of time, from 1.5 to 120 minutes. As one might expect, shorter collection times produced larger spatial variation in rainfall. Larger collection pans (larger surface area) also reduce variability (see run 3 rainfall distribution, Table 3-3, p. 120). Collection time for run 3 was very much longer (7275 seconds) than the rest. An additional measure of runoff temporal variability was established for run 6, when the pre-erosion runoff was measured at the outlet (prior to inception of uplift) using the automated water and sediment flux measurement device. The temporal coefficient of variation in runoff over a 5000 s period was 6% (n = 200; beginning part of run 6). In general, the spatial variability of rainfall is ~10% ($\sigma/\mu * 100$) for runs 1-6. An exception is run 7, where significantly greater spatial patterns were imposed. In addition to the measured spatial patterns, some runs experienced substantial temporal variation in rainfall, as measured by the fluxometer. The reader is referred to the next chapter for details concerning each run.

Measuring Fluxes at the Basin Outlet

Initially (that is, for the first two runs), mass fluxes were determined by capturing effluent at the outlet with a hand-held graduated cylinder, measuring the time required to fill the cylinder, noting the volume, and weighing the cylinder to obtain the mass of the bulk volume. Because some runs would require continuous operation for up to three weeks, an automated device was developed to measure sediment and water fluxes at the outlet to the erosion facility (Fig. 2-5, p. 42). The device consists of a cylinder resting on a thin beam load cell, with a self-actuating siphon to evacuate the cylinder. Voltage across two electrodes set in the cylinder at different locations were monitored continuously with a datalogger, and when fluid contacted each electrode, time and mass were recorded. The volume between electrodes and the load cell output voltage were calibrated prior to each run. With known volume, and measured mass and time at electrode closure, both a volumetric flow rate and bulk density of the fluid/sediment mixture is recorded. Sediment flux and water flux can be deconvolved from this record, if the density of fluid (water

~1.0 g/cm^3) and density of the solid particles (quartz, 2.65 g/cm^3) are known. Equations for mixing relations are developed below.

The device ("flux-o-meter") required two calibrations, one for the load cell, and another for the volume between electrodes. The load cell is a thin beam half-bridge design (model LDL-816, purchased from Omega), and was calibrated prior to each run to determine the scaling between observed voltage and mass. A sample calibration curve for the load cell is shown below (Fig. 2-6, p. 43). The fluxometer also required calibration of the volume between the two electrodes. The volume was calibrated by measuring the mass of clear water at the low and high electrodes over several cycles, averaging the mass, and converting to a volume using a temperature correction for the density of pure water. Typically, a calibration volume of ~100 ml was used. Volume flow rates at run conditions ranged from 5 to 30 ml/s. This results in a flux measurement every ~10-30 s, as cycle time also includes the time to evacuate the fluxometer. Each measurement represents a flux averaged over the time required to fill the calibration volume.

The equations for mixing of two components of differing density can be developed from the conservation of mass:

$$\rho_1 \, V_1 + \rho_2 \, V_2 = m_t \tag{2-1}$$

where ρ_1 and ρ_2 are the densities of the two components, V_1 and V_2 are the volumes of the two components, and m_t is the total mass of the mixture. Further, the total volume of the system is known:

$$V_1 + V_2 = V_t \tag{2-2}$$

where V_1 and V_2 are the corresponding volumes of the two components in the system. Rearranging the equation (2-2) for V_1

$$V_1 = V_t - V_2 \tag{2-3}$$

and substituting this into the conservation of mass:

$$\rho_1(V_t - V_2) + \rho_2 \, V_2 = m_t \tag{2-4}$$

Solving for V_2:

$$\rho_1(V_t - V_2) + \rho_2 \, V_2 = m_t$$

$$\rho_1 \, V_t - \rho_1 \, V_2 + \rho_2 \, V_2 = m_t$$

$$V_2 (\rho_2 - \rho_1) + \rho_1 V_t = m_t$$

$$V_2 (\rho_2 - \rho_1) = m_t - \rho_1 V_t$$

$$V_2 = (m_t - \rho_1 V_t) / (\rho_2 - \rho_1) \tag{2-5}$$

Further, $m_t = \rho_t V_t$. $\tag{2-6}$

So, substitution of (2-6) into (2-5) yields

$$V_2 = (\rho_t V_t - \rho_1 V_t) / (\rho_2 - \rho_1) \tag{2-7}$$

or

$$V_2 = V_t (\rho_t - \rho_1) / (\rho_2 - \rho_1). \tag{2-8}$$

Once V_2 is known, V_1 can be solved for using equation (2-3), and the respective masses for each component using equation (2-6). Rates are computed by dividing mass by the collection time. This approach differs from the standard method of measuring the solid mass in a fluid mixture, accomplished by weighing the total mass, then drying the mixture and measuring the residue to obtain the solid component.

Below is a plot of bulk density and volume flow rate ($n = 1420$), and prior to the inception of erosion (Fig. 2-7, p. 44). The early part of the signal ($t = 0$ to 12,500 s) records the draining of the initial reservoir from the erosion facility. The outlet is dropping continuously at its prescribed fall rate (early increase in flow rate reflects fall rate adjustment), and rainfall is being applied as well. Minor peaks in the smooth part of the flow rate result from minor stick-slip sliding of the outlet, with consequent increases in flow from ponded water in the basin. The increase in flow rate fluctuations after $t = $ 12,500 s document the change from reservoir flow to runoff over the ground surface. Erosion is negligible during this part of the run. Hence, fluctuations in flow rate are most likely reflecting runoff variability over the substrate. The abrupt drops ('spikes') in flow rate after $t = 15,000$ likely capture the cycling of timed rainfall shut-off for time lapse imagery (rain is shut off for 7 s every 500 s). Bulk density, a measure of mass, does not exhibit any corresponding change in the level of noise. Hence, the fluctuations in bulk density probably reflect electronic noise in the load cell, or momentum fluxes of fluid entering the fluxometer. The 'noise level' exhibited by the fluxometer prior to the inception of erosion places constraints on the significance of variability exhibited during

steady state erosion, and gives a measure of fluxometer sensitivity. Flow rates can be measured to within ±1%, and mass flux rates to within ±2% (2 σ). In general, volume and time can be measured more accurately than mass, and the level of variability increases with the onset of erosion.

Time Lapse Video

In order to collect a detailed record of changes in the topographic surface, an automated time lapse video capture system (a modified Sharp VHS video camera) was devised. For a list of sampling rates, see Table 2-1. For runs 1 and 2, the video captured imagery while the mist apparatus was operating. For all other runs, an automated shutoff valve was installed and used to turn off rainfall a few seconds before video recording, in order to eliminate mist. After each run, the analog VHS signal was captured and transferred to a digital signal. One frame per second of video (of 30 frames per second) was extracted from the video recording, and compiled into a movie viewable on a computer monitor. Time lapse recordings reveal activity that is not readily seen in real time. The highest transport rates are clearly those associated with runoff. Particle transport can be seen in real time (though it would be more visible if slowed down). Slower mass transporting processes are more difficult to detect in real time, but readily show up in time lapse recordings. Hillslope failure activity appears as abrupt changes in ridge crest locations. Knickpoints can easily be monitored as they propagate upstream.

Topographic Measurements

Observations must be capable of resolving first order topographic changes within the experimental basin. Current digital cameras capable of detecting part per thousand changes of the largest basin scale are readily available . For the experimental apparatus, the basin area A is 6470 cm^2 , which yields a length scale $L = 80.3$ cm ($L \sim A^{1/2}$), or roughly 100 cm. Observed macroscopic changes in landform features are on the order of 0.1-10.0 cm, or $10^{-3}L$ to $10^{-1}L$. Recent advances in digital photography enable rapid collection of spatial data at a high resolution, allowing for length determinations of $10^{-4}L$ on a routine basis (Lane et al., 1994). Observed hillslope lengths within the physical apparatus are $10^{-2}L$ to $10^{-1}L$. Maximum relief in the experimental landscapes is ~0.25L,

and local valley-to-ridge relief is ~0.1L. Hillslope tangents ($\Delta z/\Delta x$) at the hillslope scale in the apparatus can range up to 5:1, but typically are ~1:2 (50% slope). Channel slopes are ~1:5 (20% slope). Flow velocities range up to $10^{-1}L/$ s (10 cm/s), channel widths to $10^{-2}L$ (1 cm) and channel depths to $10^{-3}L$ (1-5 mm). The smallest length scale in the basin is grain size, and grains 10 to 100 μm yield 10^{-5} L and 10^{-4} L respectively. Length measurements with imaging tools available to this thesis project can reliably be made to $10^{-3}L$ (~1 mm), which places a lower limit on channel identification from imagery. This is not an unreasonable detection limit. The individual spatial elements detectable at this level are areas with sides of roughly 20 grain diameters. The range of scales for the basin is thus determined by grain size and basin length. For the experimental apparatus, this range is of order 4-5. Detection reduces the observational range to order 3. This is considered more than adequate to answer first order questions regarding landscape stability.

Photogrammetric Methods

In order to measure landscape form, stereo digital photographs (taken by a Nikon CoolPix 900, with 1280 x 960 pixels) were used to develop gridded elevation models of the landform. The process involves several steps. First, the photographs are rotated 90 degrees into rough parallelism with the basin reference frame, and converted to gray scale pixel values (range 0-255). Photographic coordinates of measured benchmarks on the basin walls were collected for each photograph. The stereo pairs were then cropped, and automatically correlated at an arbitrary grid spacing, usually every 2-4 pixels.

To assist with automated point pair collection, a two dimensional *projective* transformation (Wolf, 1983) was calculated for reference points appearing in both photographs:

$$x_2 = (a_{1,1} * x_1 + a_{1,2} * y_1 + c_1) / (a_{3,1} * x_1 + a_{3,2} * y_1 + 1) \qquad \text{(2-9, a)}$$

$$y_2 = (a_{2,1} * x_1 + a_{2,2} * y_1 + c_2) / (a_{3,1} * x_1 + a_{3,2} * y_1 + 1), \qquad \text{(2-9, b)}$$

where $a_{i,j}$ are elements in a scaling matrix, c_1 and c_2 are translation constants. Given at least 4 correlated points in each photograph, the 8 transformation parameters can be computed with a least squares inversion algorithm to determine the transformation

parameters. Typically, 15 or more correlated points were collected by hand. As a side note, a two dimensional *conformal* (involves rotation, scaling, and translation) transformation was tried initially, but this transform only works for photographic planes that are parallel to each other, and does not account well for arbitrarily oriented photographs. Additionally, the elevation field calculated (via collinearity) from a plane and a *projective* transform of that plane results in another plane. The elevation field calculated from a plane and a *conformal* transform of that plane is a curved surface. The residual difference between measured correlated coordinates and transformed coordinates is substantially smaller for a projective transform (~1-5 pixels) as opposed to a conformal transform (~5-10 pixels). Further, the residuals are minimized in one direction with a projective transform, with most of the variability contained in the camera offset direction. This fact allows for smaller search regions in the target photograph during correlation, and corresponding reductions in computing time.

The correlation proceeds by projecting the photographic coordinates of one photograph onto the second photograph. Then, averaged pixel values for the moving window are computed for each photograph. This reduces recalculation during correlation. Then, a moving window is stepped across the first photograph, and correlation coefficients (these vary between -1 and 1) are computed between windows in each photo (the moving window searches in the second photograph). The point in the second photograph with the highest correlation number is stored. During initial tests, it was discovered that an improved correlation could be obtained by searching in the photographic offset direction (i.e., the flight line direction), instead of searching in all directions around the target pixel. The flight line direction can be calculated using a projective transform from the ground reference frame to the target photograph, projecting camera ground x and y coordinates onto the photograph, and calculating the direction between camera coordinates in the photographic reference frame. This method of correlation works moderately well, but is not fail proof. Correlations also depend on search window dimensions. Trial and error suggests that a window of 16 x 16 pixels and maximum search distances ~10 pixels generate reasonable correlations in most cases.

After correlated points have been collected, camera orientations are computed using photographic coordinates and corresponding ground control points that appear in both photographs. This is accomplished with the well-known collinearity equations (see Wolf, 1983 for an excellent derivation), which describe the transformation to go from an arbitrary ground to a photographic reference frame:

$$x_p = f * (A_{11} * \Delta x + A_{12} * \Delta y + A_{13} * \Delta z) / (A_{31} * \Delta x + A_{32} * \Delta y + A_{33} * \Delta z) \quad (2\text{-}10, \text{a})$$

$$y_p = f * (A_{21} * \Delta x + A_{22} * \Delta y + A_{23} * \Delta z) / (A_{31} * \Delta x + A_{32} * \Delta y + A_{33} * \Delta z), \quad (2\text{-}10, \text{b})$$

where

$$\Delta x = (x_g - x_{ci})$$

$$\Delta y = (y_g - y_{ci})$$

$$\Delta z = (z_g - z_{ci}).$$

For the subscripts, p refers to photographic coordinates, g refers to ground reference frame coordinates, c_i refers to camera location coordinates in the ground reference frame, f is effective camera focal length in dimensions of ground reference frame, and A_{ij} is the 3 x 3 rotation matrix,

$$A_{11} = Cos(\phi) * Cos(\kappa)$$

$$A_{12} = Cos(\omega) * Sin(\kappa) + Sin(\omega) * Sin(\phi) * Cos(\kappa)$$

$$A_{13} = Sin(\omega) * Sin(\kappa) - Cos(\omega) * Sin(\phi) * Cos(\kappa)$$

$$A_{21} = -Cos(\phi) * Sin(\kappa)$$

$$A_{22} = -Sin(\omega) * Sin(\phi) * Sin(\kappa) + Cos(\omega) * Cos(\kappa)$$

$$A_{23} = Cos(\omega) * Sin(\phi) * Sin(\kappa) + Sin(\omega) * Cos(\kappa)$$

$$A_{31} = Sin(\phi)$$

$$A_{32} = -Sin(\omega) * Cos(\phi)$$

$$A_{33} = Cos(\omega) * Cos(\phi),$$

where ω is rotation around the x axis, ϕ is rotation around the y axis, and κ is rotation around the z axis. Angles are in radians. Positive rotations indicate counterclockwise rotation when looking down the axis toward the origin. The rotation matrix accounts for the rotations to go from the one reference frame to another, that is, the photographic to the ground reference frame. A set of collinearity equations can be written for any point

appearing in a photograph. The collinearity equations contain twelve variables. If measured ground control and photographic points and camera locations are known, then four unknowns remain: the three rotations and effective camera focal length. These can be determined if at least two ground control points are known (i.e., two points yield four equations in four unknowns). Since the collinearity equations are nonlinear, a numerical scheme (Newton-Raphson's method) that approximates a solution to the collinearity equations was employed, and iterated until changes in the unknowns were negligible. The numerical scheme involves writing out the partial derivatives of each equation with respect to the unknown variables, evaluating the collinearity equations and partial differentials of the equations at initial approximations for the unknowns, and using a least squares method to solve for the unknown corrections to the approximations. The corrections are added to the unknowns, and the solution is iterated until corrections are small (Wolf, 1983).

Once the camera parameters have been determined, ground x-y-z coordinates of correlated points can be computed, again by solving the collinearity equations (Equations 2-10). The ground coordinates are then read into an arbitrarily spaced grid (usually at 7 mm horizontal grid spacing), and filtered for extreme or missing values. The precision of photogrammetric solutions using a 1280 x 960 pixel resolution camera is somewhat modest. Elevation ranges calculated for single pixel shifts are in the range from 7 to 20 mm (~0.01L), depending on the distance between the ground surface and camera, and the field of view. Nonetheless, a fair amount of detail can be discriminated from the elevation fields derived from this method (Fig. 2-8, p. 45). The main ridges are clearly visible. Local ridge relief is ~7 cm in this case, and the maximum relief is ~22 cm.

Topographic Statistics

For this thesis to succeed as a test of drainage basin stability, essentially a binary outcome is required. Do topographic features remain laterally fixed under steady state erosional conditions? A time series visual representation of drainage structure over long times under steady forcing is sufficient to answer that question. However, quantitative measures that may yield insight into functional relationships between forcing,

topographic form, and behavior can be constructed from detailed elevation measurements of surface topography through time. As described in the photogrammetric section, calibrated stereophotographs (that is, known camera locations and viewing orientations) can be used to obtain elevation data sets of topography. Statistical measures of landscape form, as well as measures of spatial erosion rates and flow path changes, can be derived from such data sets. Numerous sets of stereophotographs (from 9 to 71) were collected over the course of each run. Discrete spatially referenced elevation data points were collected from many of the pairs, and read into a grid (Fig. 2-8, p. 45).

Geomorphic measures could then be extracted from the elevation fields. These include maximum and local relief, hypsometric curve, average steepest descent slope, cumulative flow through a cell in the grid, and local relative height. Each of these measures will be detailed below, and diagrams for each measure from a representative data set for run 2 are presented to clarify the process. Maximum relief is just the range in elevation of a surface. Local relief is a statistical measure computed by calculating the mean standard deviation of elevation as a function of distance from the outlet (Fig. 2-9, p. 46). Regional slope can be extracted from the slope of a linear regression through a plot of average elevation versus distance from the outlet (Fig. 2-9, p. 46), and local slope computed from the distribution of steepest descent slopes. Local relative height ranks a point in the grid based on neighboring elevations, and the global distribution of relative height counts locations that are likely to be peaks, divides, valleys, and depressions. These measures are detailed below.

The hypsometric curve is essentially a normalized cumulative frequency distribution of elevation (Strahler, 1954). This curve is constructed by summing the number of data points higher than incremental thresholds of elevation, starting at the maximum elevation. The threshold elevation (h) is normalized to the range in elevation (H), and the number of points above the threshold (a) is normalized to the total number of points (A). For an object with rectangular boundaries, this measure captures continuous elevation change of the object over the incremental spacing of the threshold. This measure is not sensitive to surface roughness, but it is sensitive to locally clumped elevations, such as a plateau.

Smooth sloping curves indicate continuous changes in elevation. It is not straightforward to compare different shaped objects with this measure, but it is useful in mapping curvature for similarly bounded objects. A simple comparison between curves is to note the value of a/A at $h/H = 0.5$. This yields the fractional number of points above the midpoint of elevation. Hence, it is a crude measure of the center of mass. In the diagram below (Fig. 2-10, p. 47), the value of a/A at $h/H = 0.5$ is about 0.47, indicating that 47% of the elevations are higher than the midpoint of elevation.

Steepest descent slope is calculated by computing the slope ($\Delta z/\Delta x = (z_i - z_j)/((x_i - x_j)^2 + (y_i - y_j)^2)^{1/2}$) to all neighboring cells, and recording the steepest slope and direction. Once the steepest descent vectors have been determined, flow can be routed through the grid, and cumulative upstream area draining through a cell can be compiled. A map of unit runoff (that is, contributing area) that has been logarithmically transformed appears in Fig. 2-11 (p. 48). Flow paths are clearly defined, implying that elevations derived from stereophotogrammetric methods outlined above adequately capture the structure of the drainage basin. Contributing area-slope plots can then be constructed (Fig. 2-12, p. 49). Such plots are frequently used to describe drainage basin structure, and offer a measure of the degree of concavity in stream profiles.

Local relative height is a essentially a ranking algorithm that characterizes a location based on its height relative to local surrounding elevations. This rank is a simple indicator of whether the location is likely to be a peak (all neighbors are lower), a depression (all neighbors are higher) or somewhere in between. The algorithm counts the number of cells in a moving window lower than the center cell, and normalizes the cell's value to the total number of cells in the window. Possible values for relative height range from 1 (all nearby points are lower, location is a peak) to 0 (all nearby points are higher, location is a depression). When plotted as a gray scale map, this algorithm details ridges quite well and valleys moderately well (Fig. 2-13, p. 50). The increments of relative height value are set by the size of the moving window. For a 3 x 3 pixel window, the possible values are 0/8, 1/8, 2/8, 3/8 etc., and for a 5 x 5 window 0/24, 1/24, 2/24 etc. The frequency distribution of local relative height can be used to compute the number of cells that are

35

likely to be valleys and ridges (Fig. 2-14, p. 51). Some arbitrary threshold of relative height must be set in order to compute the area occupied by a ridge or a valley. Valley fractional area (number of cells with values < threshold, divided by total number of cells in elevation grid) is a proxy for drainage density, normally computed as the total stream length divided by basin area.

Landscape dynamics can be characterized if time series data sets are available. Direct measures of landscape activity and stability include spatial erosion rate maps constructed by differencing time series of elevation grids and dividing by the separation time between grids, and changes in steepest descent flow directions between grids to assess flow path stability. Erosion rate variability and flow path stability will be presented in a subsequent chapter on landscape dynamics. In summary, the methods of monitoring the erosion facility include stereo photography and topography, time lapse video, and fluxes of water and sediment leaving the erosion facility. Digitized time lapse video for the runs reported in this thesis are available for viewing in a CD-ROM attached to this thesis (SupportingData\index.html). Outlet elevation was also recorded during the course of each run, and these observations are presented along with individual run descriptions in the next section.
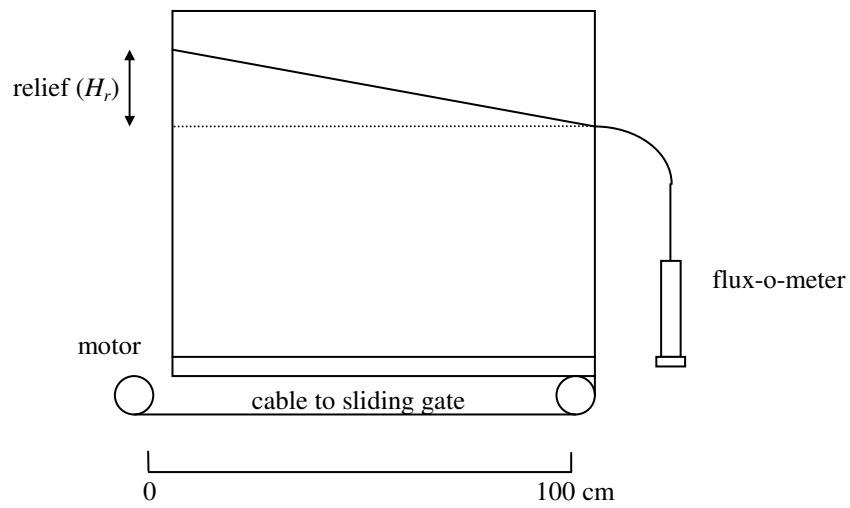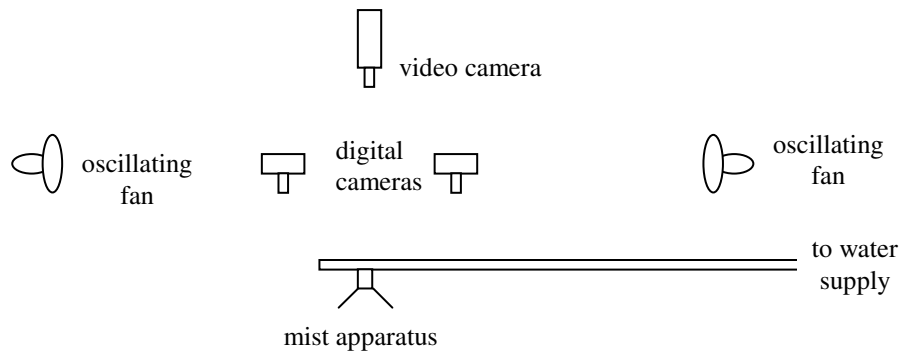
Figure 2-1. Schematic cross section of erosion facility. Scale is approximate.
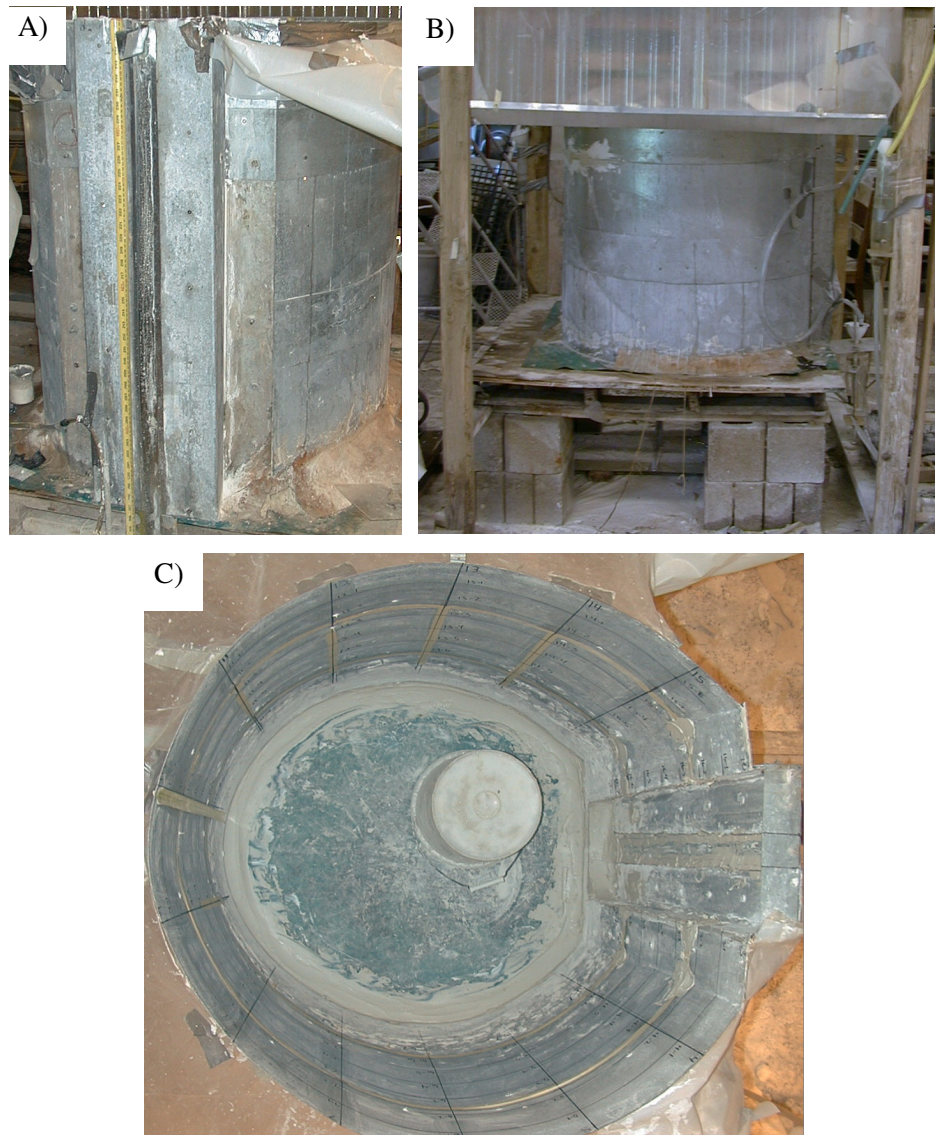
Figure 2-2. A) Front, B) side, and C) top view of tank. Tank depth is 100 cm, length is 99 cm, and width is 87 cm. Lines on tank rim and interior walls were used for ground reference points. Kaolinite was used as a seal around interior floor and along sliding outlet (right side of C).

Figure 2-3. Sheet flow reduces relief and smoothes the surface. Width of image is 17 cm. Note the knickpoint in the lower right.

Figure 2-4. Initial surface condition prior to erosion. Outlet to basin is on the right. Smoothed mounds are remnant mud volcanoes. Holes are from persistent drips during rainfall calibration. An initial stream pattern has developed in a few places. Basin length (from left to right) is 99 cm.

Table 2-1 Time lapse video settings and stereo photograph collection

run id.	run duration (s)	eroded distance (cm)	number of stereo photos	video sample rate (s per s of runtime)	rain shutoff duration for video (s)
1	145206	43.8	11	2/120	0
2	220245	84.8	10	2/300	0
3	64520	82.9	3	1/300,1/200	7
4	1371600	88.1	10	1/250	6
5	584160	81.4	15	1/500	6
6	932400	88.9	33	1/500	6
7	584160	86.8	71	1/200	5
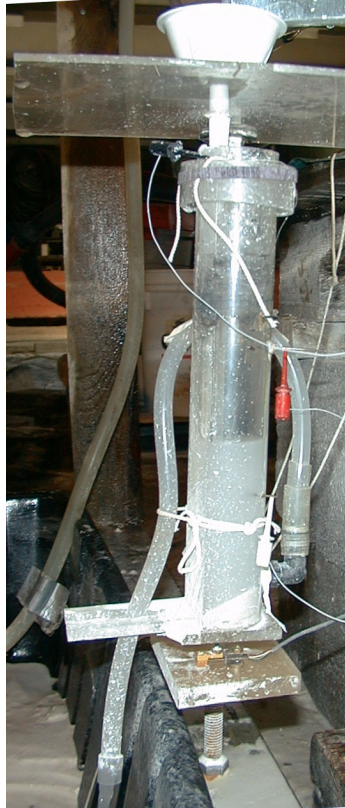
Figure 2-5. Sediment and water flux measurement device ("flux-o-meter"). Wire leading to the black clip at the top of the cylinder is the ground, red clip on right side of cylinder is the upper circuit, white clip is the lower circuit. A datalogger monitors voltage across the electrodes, and records time and mass when each electrode closes. Load cell is visible as a bronze fixture beneath the plexiglass cylinder. Effluent is flushing through the siphon in this photograph. Measurement errors for volume flow rate are ± 1 %, and for mass rate ± 2%.
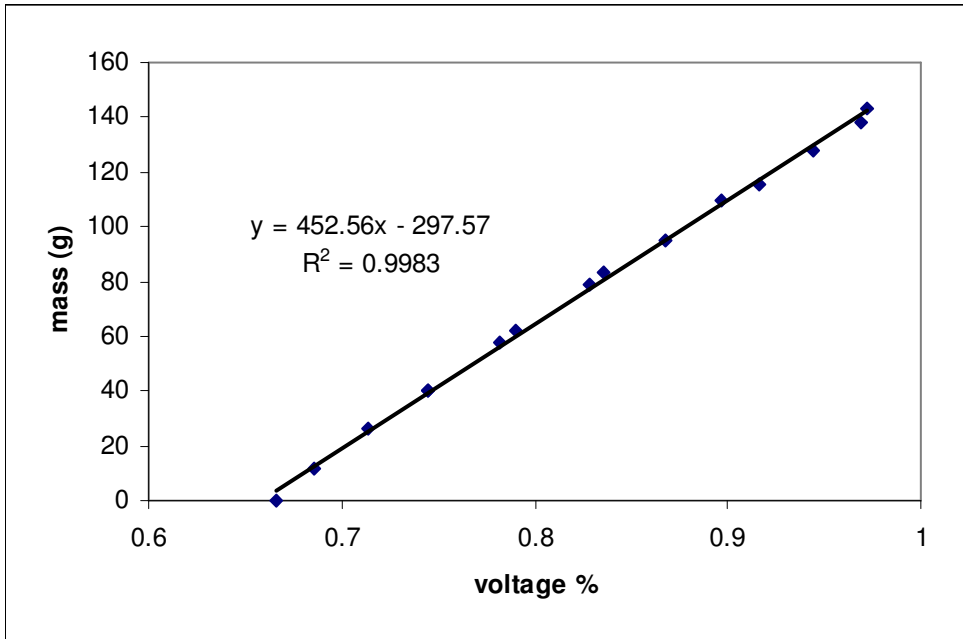
Figure 2-6. Calibration curve for thin beam load cell. Known masses of water were added to the fluxometer, and the voltage, normalized to the excitation voltage, was recorded.
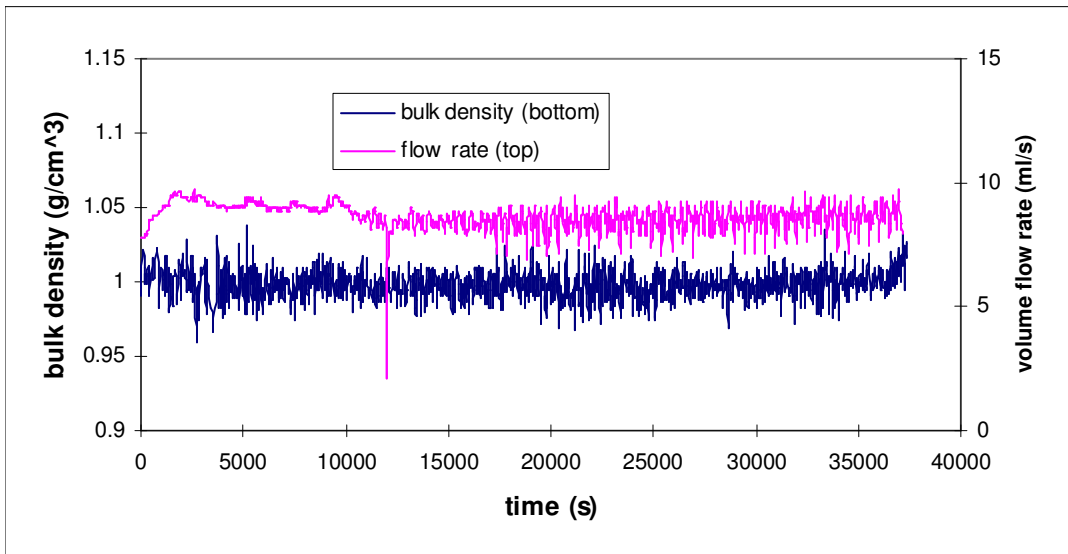
Figure 2-7. Sources and scale of fluctuations in flow rate and bulk density measurements. The time from 0 to 12,500 represents draining of the reservoir over the substrate with a constant falling base level (early in run 6). The abrupt drop in flow rate marks the emergence of the ground surface. Erosion is still negligible during this time, so the increased level of noise in flow rate is partly due to runoff over the surface. The noticeable low values in flow rate beyond 20,000 s is due to rainfall cessation for 6 s every 250 s during time lapse video collection.
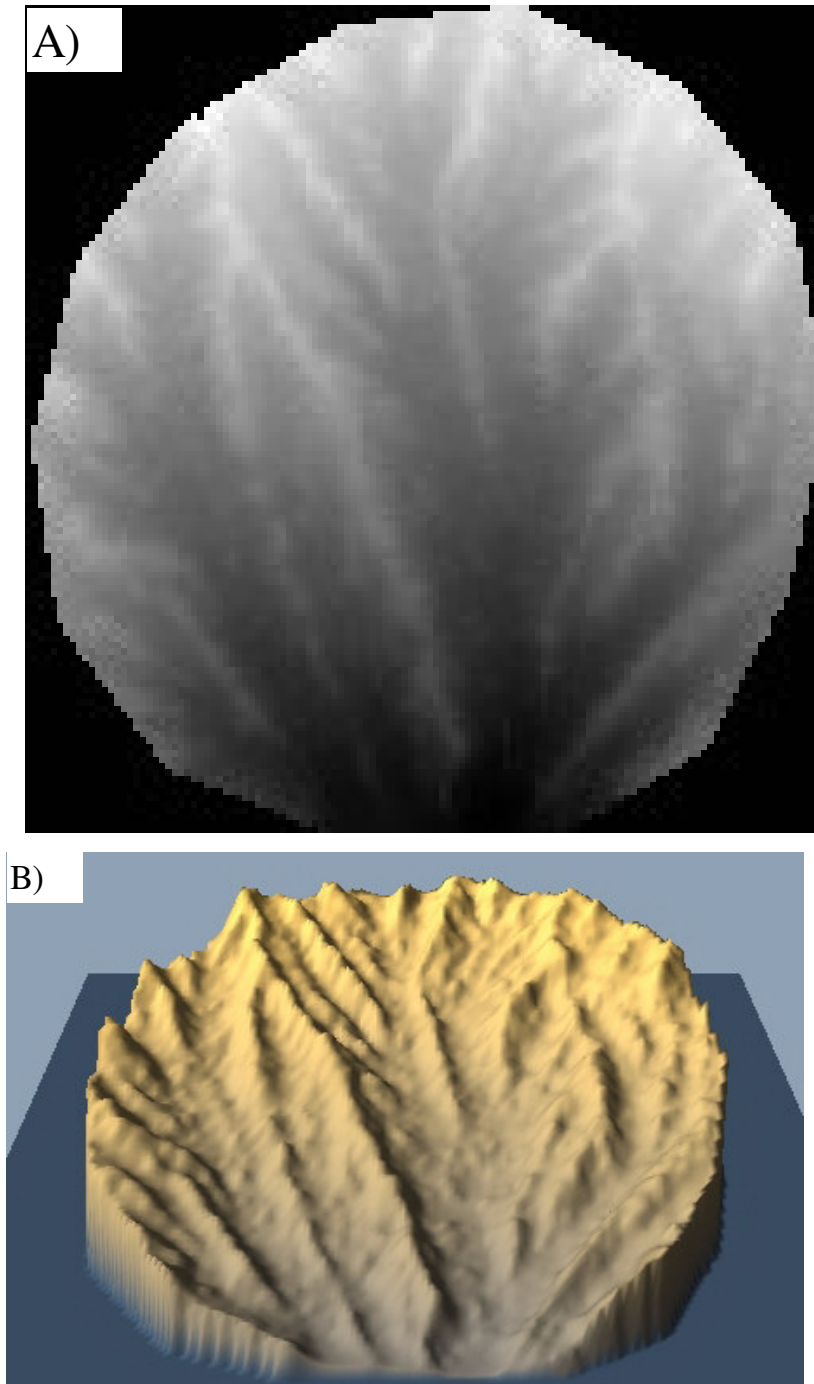
Figure 2-8. A) Gridded elevation data set, plotted as a gray-scaled height map. Elevation range is 21.9 cm. Width of image is 87 cm. Grid spacing is 7 mm, with 12,770 data points in the grid. Original *xyz* data consisted of 37,017 points, which are averaged as they are read into the grid. Basin boundaries are enforced by cropping the data set to known ground control points on the basin wall. B) Perspective view of surface.
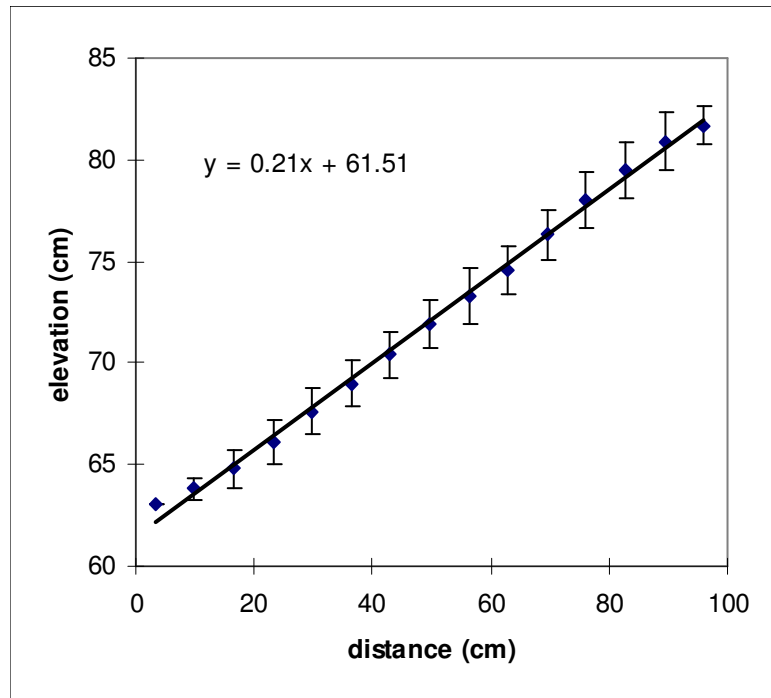
Figure 2-9. Average elevation plotted against distance from the outlet. Error bars represent 1σ ranges in elevation at each binned distance. Averaged deviations yield a value for local relief, in this case, 1.3 cm. The slope of the trend line, 0.21, is used herein as the regional slope of the surface.
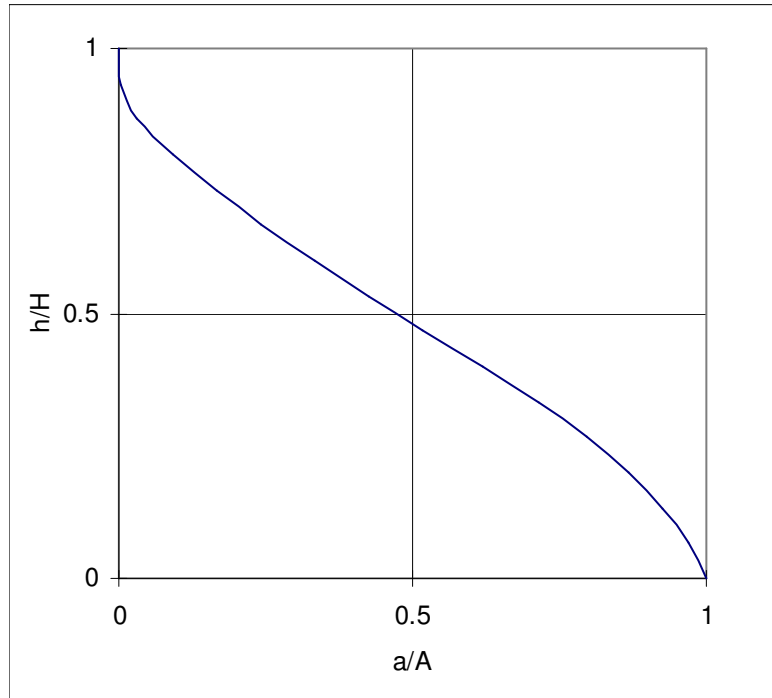
Figure 2-10. Cumulative distribution of elevation lower than a threshold elevation (15 binned intervals). H is maximum relief; h is threshold elevation subtracted from the maximum elevation. A is the total number of points; a is the number of points below the threshold elevation. The value of a/A at $h/H = 0.5$ is close to 0.5, indicating a nearly rectilinear sloping surface.
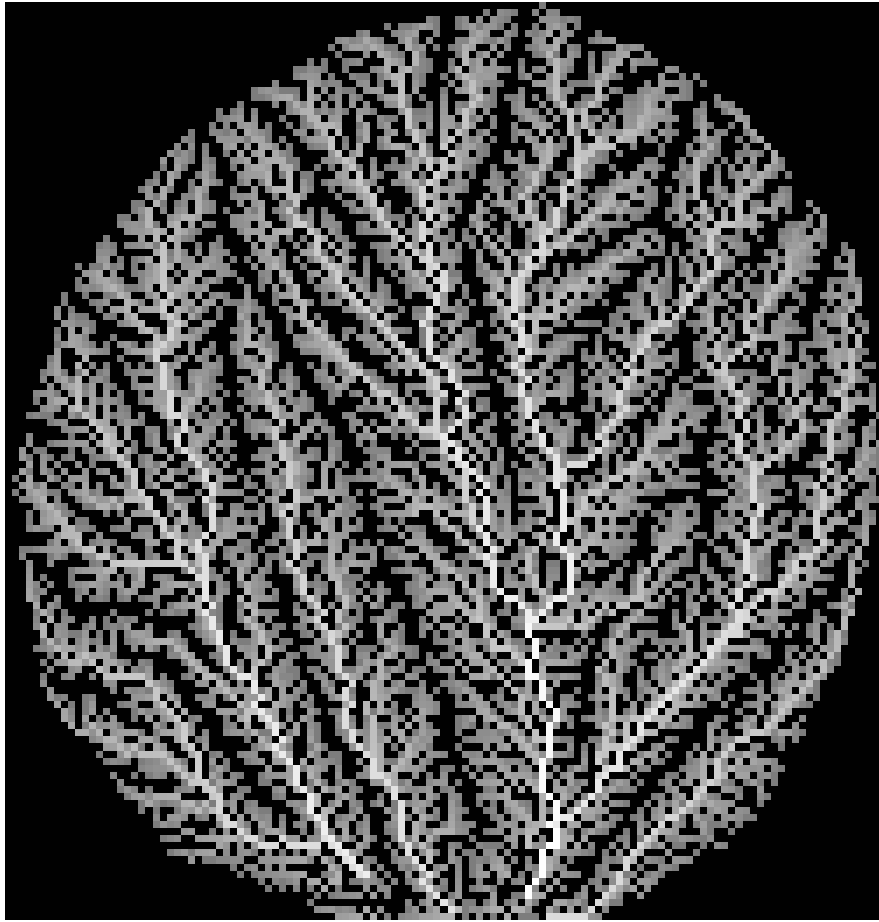
Figure 2-11. Cumulative drainage area upstream from each cell in the grid, converted to log values of area, and plotted as a gray-scaled height map. Maximum value of contributing area for this grid is 3606 cm^2. Grid spacing is 7 mm, with 12,770 data points in the grid. Dark values indicate ridge locations.
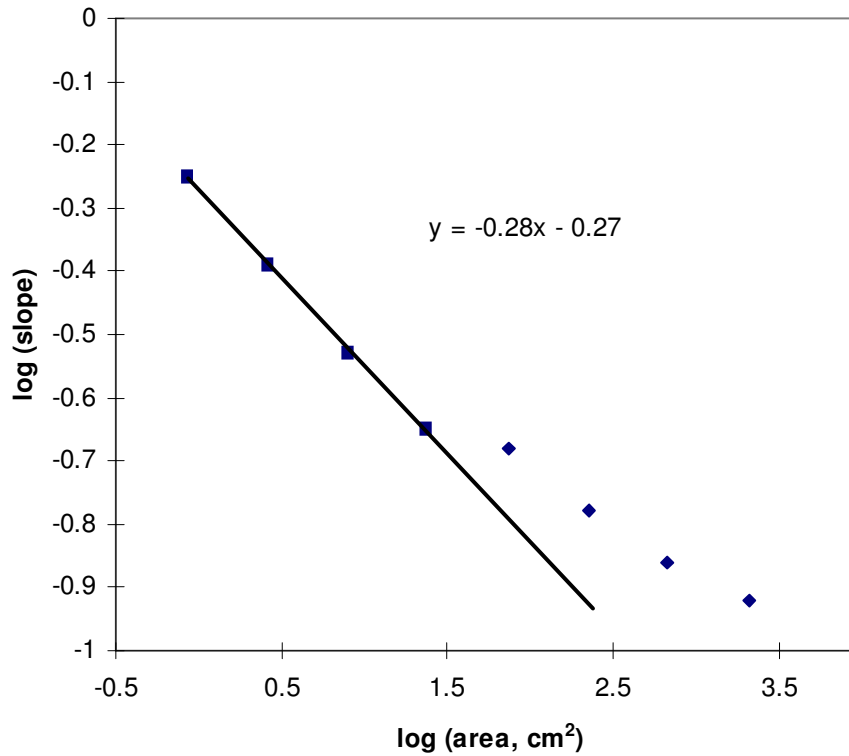
Figure 2-12. Area-slope relation, plotted in logarithmic space. A trend line has been plotted through values less than log (A) = 1.5 (A = 31.6 cm^2), which marks a distinct break in the area-slope relation. Similar breaks in scaling have been noted for natural drainage basins. The exponent θ (in the relation $S = kA^{-\theta}$, where S is slope magnitude, and A is contributing area) is 0.27, and k = -0.26 (slope = 55% for a contributing area of 1 cm^2).

Figure 2-13. Local relative height plotted as a gray-scaled height map. White represents points that are higher than their adjacent neighbors (peaks). Dark values represent locations that are lower than their neighbors (depressions). Moving window size is 7 x 7 pixels (4.9 x 4.9 cm). Local relative height captures the ridge structure of the topographic surface. Valleys are less well defined. Grid spacing is 7 mm, with 12,770 data points in the grid.
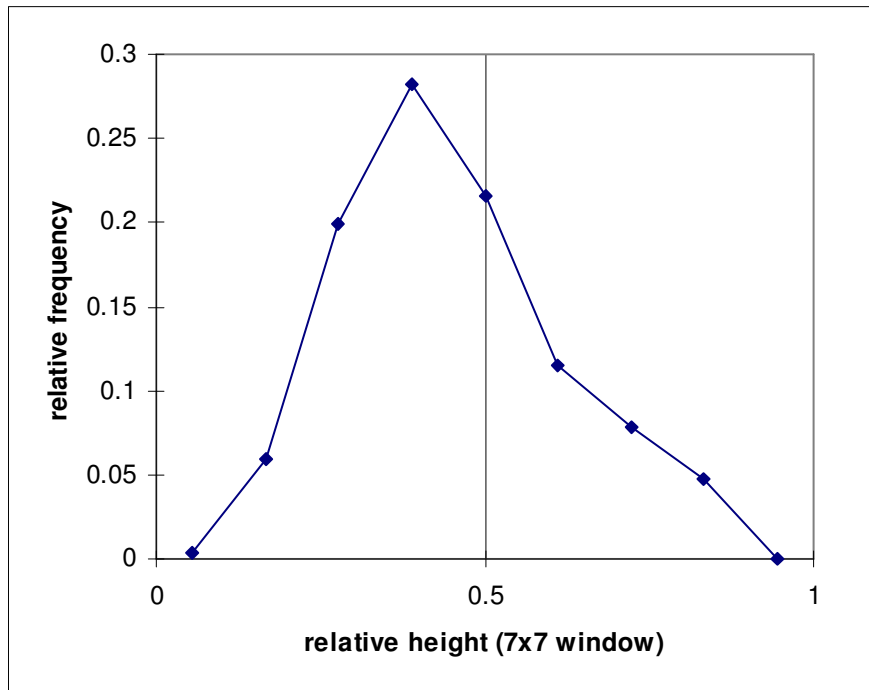
Figure 2-14. Frequency distribution of relative height values for a 7 x 7 pixel moving window. No absolute peaks or depressions are present in the distribution, with most values falling near 0.4 (40% of the neighbors are lower) indicating that the surface is dominated by locations that are likely to be places with convergent flow. Note there are 8 bins of relative height. Summing the distribution from 0 to 3/8 yields a value of 0.26, and summing the distribution from 5/8 to 1 yields 0.12. Hence, about 26% of the surface is likely to be strongly convergent, and about 12% is strongly divergent flow.

Run Descriptions

This section documents the forcing conditions of base level and runoff for seven runs, presented in chronological order. Rainfall and/or uplift rates were varied between runs, and diagrams of base level elevation, fluxes at the outlet, and maximum relief document forcing conditions and general landscape change for each run. Spatial rainfall calibrations were performed prior to each run, and tables of measurements are given below. A diagram of the run conditions will be presented for each run, followed by a brief discussion of problems encountered during the run. Qualitative visual observations of the topographic form and erosional processes at steady state conditions are documented with photographs of the surface.

Overall, continuous steady forcing from base level fall and rainfall intensity was maintained over extensive periods of erosion (> 1 H_r) for five of the runs. Two of the runs experienced significant temporal (runs 5 and 7) and spatial variations (run 7) in rainfall rate.

Run 1

The first run was conducted in July, 1998. This experiment represents an exploratory test of drainage basin development. All prior tests of small scale landscapes had not employed a steady base level fall, and the effect of this boundary condition on the relief and slope that would develop in the landscape was essentially unknown. A *r/u* of ~1 was chosen (r = 3.8 µm/s; u = 2.3 µm/s). A single radial mist apparatus placed over the center of the basin supplied rainfall. Sediment (D_{50} = 45 µm) and kaolinite were mixed (1 wt. %) in a cement mixer with water, and poured into the basin (dry bulk density = 1.88 g/cm^3). Then, the spatial distribution of rainfall was measured. The substrate was not allowed to settle overnight for this run. The run was conducted over a period of 5 days, and turned off overnight. No significant problems were encountered with this run. Minor stick-slip behavior of the sliding outlet was noted, visible in the base level record at ~ 25,000 s. Later (from 110,000 to 125,000 s), the substrate was locally perturbed by a sampling procedure, inducing local slope failure to occur. Minor fluctuations in sediment yield were noted for this time period . Overall, forcing from base level fall and runoff

were demonstrably steady (Fig. 2-15, p. 54). Rainfall spatial distribution was moderately uniform, with spatial coefficient of variation of 11% ($\sigma/\mu * 100$; Table 2-2, p. 57). Sediment flux at the outlet exhibited significant fluctuations during rehydration, but the total response time to dehydration is a small fraction of the total run time, on the order of 5-10 %. Dominant erosional processes during the run include frequent knickpoint development and migration upstream, and hillslope failures. Temporary sediment storage in valleys is also quite visible in time lapse video of the run.

A set of three vertical photographs (Fig. 2-16, p. 55) shows the initial surface, the surface nearing complete dissection, and the surface at the end of the run. Approximately 13 cm of relief have been eroded after complete dissection was achieved, or ~0.5 H_r. Measurements of sediment flux at the outlet indicate that uplift is on average balanced by erosion at complete dissection. Topographic structure continued to evolve, however, after complete dissection. Ridges in the left hand side of the basin have extended and developed higher local relief. Smooth valley floors visible in the lower part of photograph (Fig. 2-16, C) are indicative of temporary sediment storage. An oblique photo taken prior to complete dissection (Fig. 2-17, p. 56) shows the smoothed nature of valley floors, as well as evidence for slumping (lower right, Fig. 2-17).
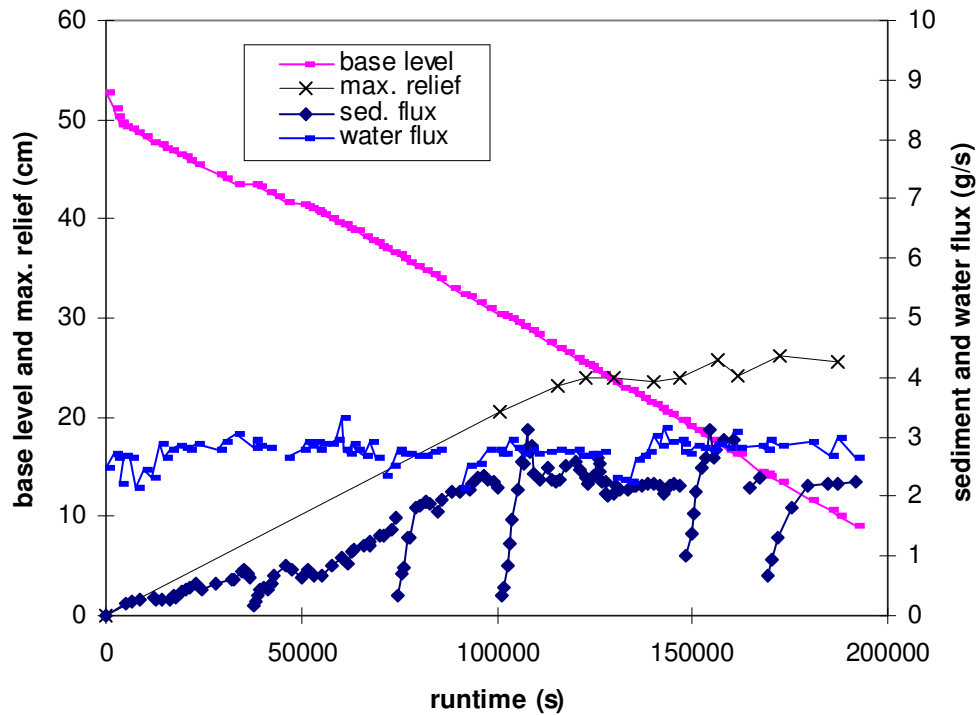
Figure 2-15. Forcing conditions, outlet fluxes, and relief for run 1. Flux measurements were determined by weighing effluent captured in a 100 ml graduated cylinder at the outlet, and recording the time to fill a known volume. Measurement errors (2 σ) for fluxes are ~3%, for base level measurements 0.2 mm, and for relief 1 cm. Complete dissection was reached at 123,000 s, with a corresponding relief of 21.9 cm. Note the steady state average relief is 24 cm. Slightly less than 1 H_r of the landscape was eroded after complete dissection. Note the obvious breaks in sediment flux. These record the beginning of a new day, and document the response of the landscape to rehydration. Minor stick-sliding of the outlet occurred early in the run.
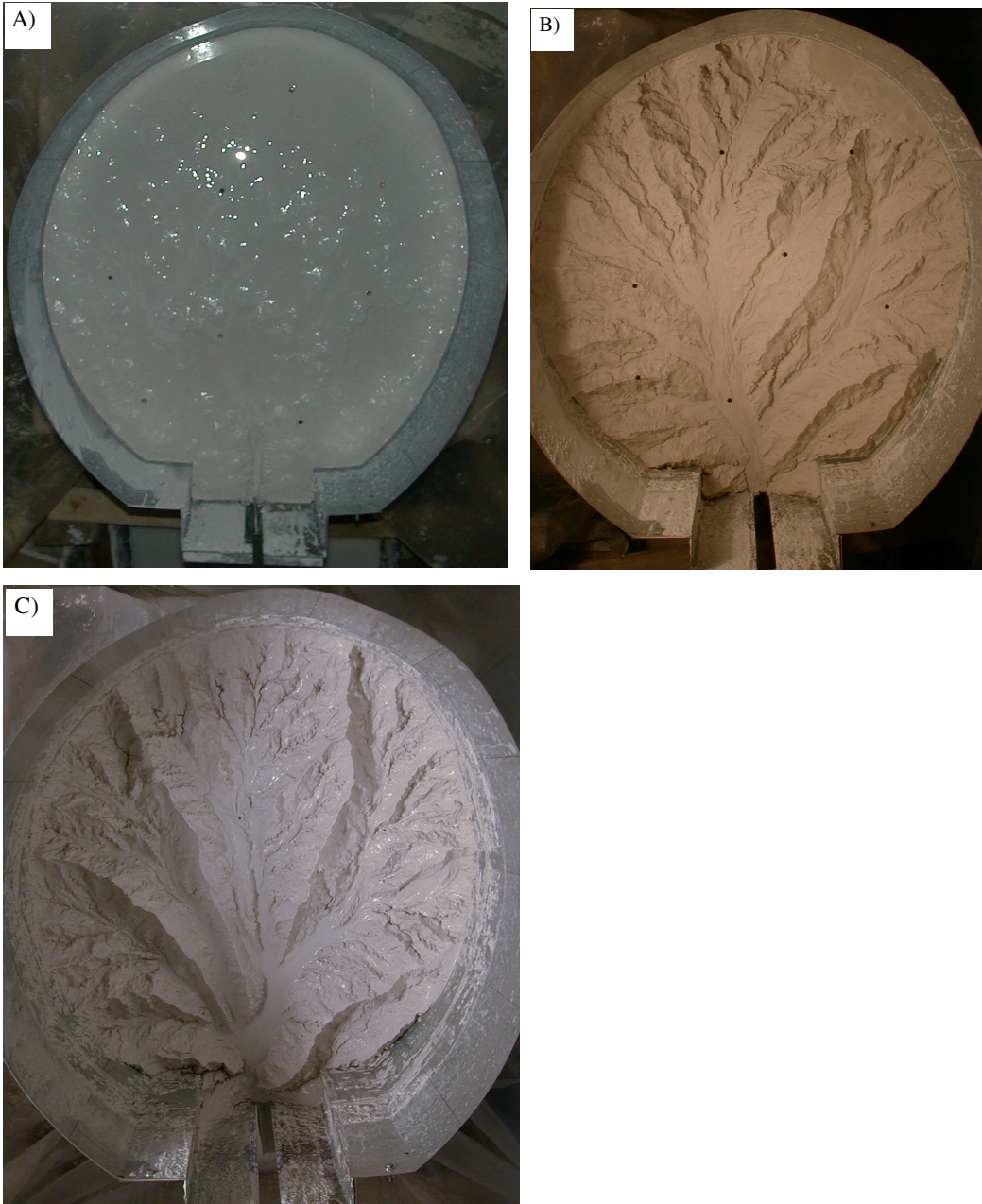
Figure 2-16. A) Initial flat surface before the inception of base level fall and rainfall. B) Surface nearing complete dissection. A remnant of the initial plateau is visible in the upper left. C) Surface at the end of the run. Note the growth of long divides on the left hand side of the basin by the end of the run. Also visible is a smooth valley in the lower center, diagnostic of temporary sediment storage.

Figure 2-17. Oblique view of surface prior to complete dissection. Width of image is ~40 cm. Slumping is apparent in the lower right of the image. Ridges and valleys are relatively smooth.

Table 2-2 Run 1 Rainfall Spatial Distribution

average (μm/s): 3.8

standard deviation (μm/s): 0.42

coefficient of variation: 0.11

collection time: 420 seconds

pan area = 38.5 cm^2 ($n = 25$)

x ground coordinate across top row, cm

y ground coordinate down left column, cm

for reference, outlet is located at $x = 45$, $y = 0$

	0	10	20	30	40	50	60	70	80
0					3.8				
10			3.2				3.6		
20		3.4			3.4			4.0	
30				3.5			3.3		3.7
40	4.7				3.2				
50			4.0			3.1		3.4	4.0
60		4.6			3.6				
70				4.1			3.7		4.0
80			4.0		4.0			4.1	
90						4.0	4.0		

Run 2

For run 2, and all subsequent runs, the depth of the tank was increased by 20 cm (from 80 cm to 100 cm), to allow for the landscape to erode through a greater number of relief distances (H_r). Run 2 was conducted in October, 1998, with *r/u* of 0.8. Rainfall rate was about the same as in run 1 (3.9 µm/s, or 3% greater), and a slightly higher base level fall rate was applied (2.8 µm/s, or 22% greater). Rainfall spatial distribution was moderately uniform, with spatial coefficient of variation of 12% (σ/μ * 100; Table 2-3, p. 63). Sediment (D_{50} = 45 µm) and kaolinite were mixed (100:1 by weight) in a cement mixer with water, and poured into the basin (bulk dry density = 1.78 g/cm^3), and allowed to settle overnight. A minor leak near the front of the basin occurred during settling, and some of the substrate escaped, forming a minor depression in the basin surface. This low spot initially captured flow, but no evidence of this initial low could be seen in the surface at complete dissection. Run 2 was conducted continuously overnight, and lasted for 5 days, and eroded through 3 H_r after dissection. Sediment flux at the outlet fluctuates around an average value shortly after complete dissection of the original flat surface. Average maximum relief after dissection was 24.1 cm. The 'missing data' portions of the forcing record occurred as the operator went home for the night. Steady forcing was less demonstrable for this run (Fig. 2-18, p. 59), due to the lack of data collection during operator absence. Dominant erosional processes during run 2 included frequent knickpoint development and propagation, and hillslope failures. Temporary sediment storage in valleys is quite visible in time lapse video of the run, and in still photographs (Fig. 2-19, p. 60-61). Ridge growth and annihilation, as well as ridge migration, were documented for this run (see Chapter 4, Landscape Instability). Terraces are visible along the lower reach of the trunk stream in Figs. 2-19 B and 2-20 (p. 62).
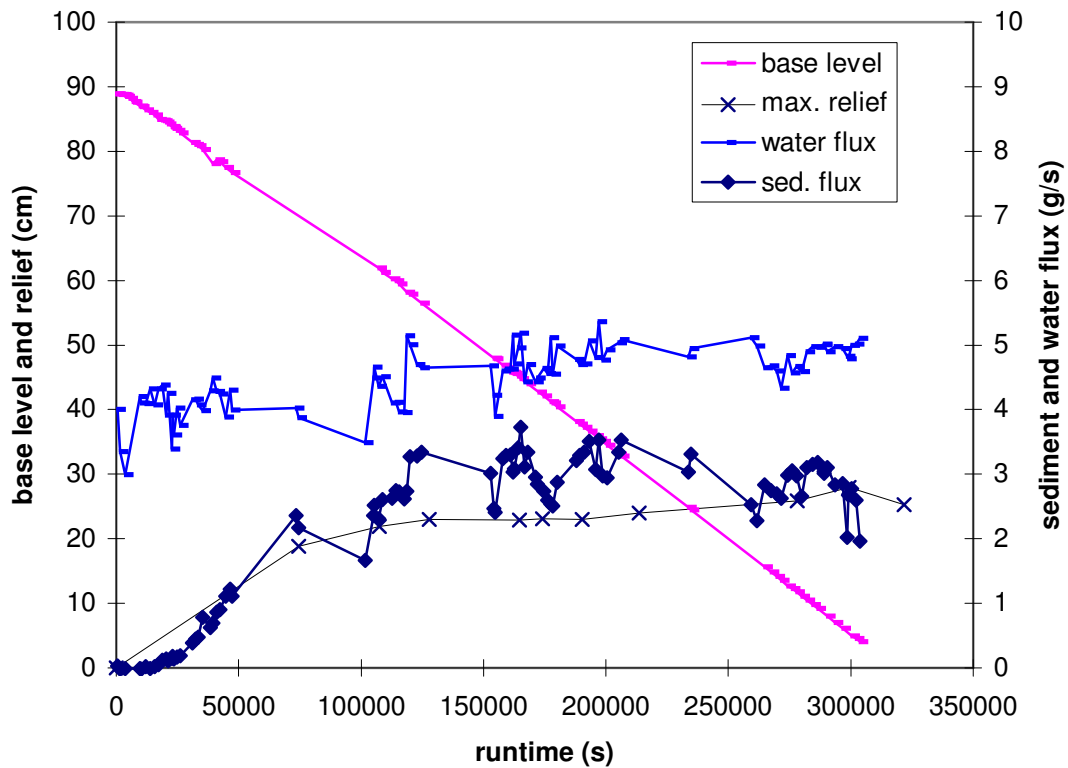
Figure 2-18. Forcing conditions, outlet fluxes, and relief for run 2. Flux measurements were determined by weighing effluent captured in a 100 or 250 ml graduated cylinder at the outlet, and recording the time to fill a known volume. Measurement errors (2 σ) for fluxes are ~3%, for base level measurements 0.2 mm, and for relief 1 cm. Very minor stick-sliding of the outlet was observed early in the run. Complete dissection was reached at 74,000 s, with a corresponding relief of 21.9 cm. Note the steady state average relief is 24.1 cm. Three relief units (H_r) of the landscape were eroded after complete dissection.

Figure 2-19. Vertical photographs of A) surface at complete dissection; and B) surface at the end of the run, after ~3 H_r of erosion. Basin width is 87 cm. Note the poor correspondence of ridge locations between the two images.

Figure 2-19. Vertical photographs of A) surface at complete dissection; and B) surface at the end of the run, after ~3 H_r of erosion. Basin width is 87 cm. Note the poor correspondence of ridge locations between the two images.

Figure 2-20. Sub-vertical view of surface after 18 cm of erosion since complete dissection (0.75 H_r). Several hillslope failures are visible as scalloped sections along ridges. White lines in lower left are projected parallel lines from a slide projector above the tank. Width of image is ~50 cm. Terraces are visible along the lower right hand side trunk stream. The valley floors tend to be quite smooth, with poorly defined channels.

Table 2-3 Run 2 Rainfall Spatial Distribution

average (μm/s): 3.86

standard deviation (μm/s): 0.49

coefficient of variation: 0.12

collection time: 420 seconds

pan area = 14.0 cm^2 ($n = 90$)

x ground coordinate across top row, cm

y ground coordinate down left column, cm

for reference, outlet is located at $x = 45$, $y = 0$

	5	15	25	35	45	55	65	75	85	95
5					3.7	4.1	4.2	4.6	4.8	
15		3.8	3.7	3.8	4.1	4.2	4.4	4.5	5.0	
25		3.9	3.7	3.8	4.0	4.2	4.3	4.3	4.8	5.0
35		3.9	3.7	3.8	4.2	4.8	4.5	4.2	4.6	4.6
45		3.9	3.8	3.7	4.2	4.3	4.6	3.6	4.4	4.4
55	4.2	3.9	3.7	3.7	4.0	4.0	4.1	4.0	4.1	4.0
65	4.2	3.8	3.6	3.5	3.5	3.0	3.7	3.8	3.9	3.9
75	4.3	3.8	3.6	3.4	3.4	3.0	3.5	3.6	3.8	
85		3.7	3.6	3.3	3.3	2.9	3.4	3.4	3.5	
95			3.4	3.4	3.2	3.4	3.2	3.2	3.3	
105			3.5	3.1	3.1	3.3	3.1	3.2		

Run 3

Run 3 was conducted during May and June, 1999, with *r/u* of 0.6. This run represents conditions where surface runoff is very low relative to base level fall. Rainfall rate was significantly higher than in previous runs (6.1 μm/s), and a higher base level fall rate was applied (6.0 μm/s). Rainfall spatial distribution was uniform, with spatial coefficient of variation of 5% (σ/μ * 100; Table 2-4, p. 69). Sediment (D_{50} = 45 μm) and kaolinite were mixed (100:1 by weight) in a cement mixer with water, and poured into the basin (bulk dry density = 1.75 g/cm^3), and allowed to settle overnight. Mud volcanoes pock-marked the surface upon draining the reservoir. Rainfall spatial distribution was collected, and the run was initiated the following day (substrate sat for two days after mixing). Prior to the run, an automated sediment and water flux measurement device ("flux-o-meter") was constructed to provide a continuous record of runoff and sediment yield (Fig. 2-21, p. 66). The flux-o-meter experienced some difficulty, as sediment concentration in the flow was high enough to incapacitate the self-actuating siphon. Additional noise in the flux record comes from momentum flux as effluent entered the fluxometer. This run represents an extreme condition, where sediment flux actually exceeds the contribution to runoff from rainfall and pore water.

Run 3 was conducted continuously overnight, and lasted for 45 hours. Large mass movements occurred after dissection, but early in the run. Time lapse video recorded only 30-40 % of the run, as circuitry was damaged by mist from the rainfall apparatus. Time lapse video reveals that up to 25% of the basin area was flowing at one point, substantiating the hypothesis that lower *r/u* enhances mass movements. The effect of such movements was to reduce local relief. Large movements were not evident later in the run, perhaps from increased substrate strength due to compaction. Relatively large (2 cm) knickpoints were common during this run, and are readily visible in Fig. 2-22 (p. 67-68). Note the relatively close spacing between the knickpoints. Hillslope failures are visible as scalloped sections of ridges, notable along the long ridge in the left center of Fig. 2-22 (B). Terraces are visible in the lower right of Fig. 2-22 (B). Only 3 topographic data sets at steady state conditions were collected for this run. Average relief was 25.4 cm. Run 3

was allowed to erode to a near nil erosion rate at the end of the run, after the outlet

reached the base of the tank and the motor-controlled outlet was turned off.

Figure 2-21. Forcing conditions, outlet fluxes, and relief for run 3. Flux measurements were determined by an automated sediment and water flux measurement device. Measurement errors for fluxes are ~2%, for base level measurements 0.2 mm, and for relief 1 cm. Complete dissection was reached at 39,000 s, with a corresponding relief of 24.0 cm. Note the steady state average relief was 25.5 cm. Three relief units (3 H_r) of the landscape were eroded after complete dissection.
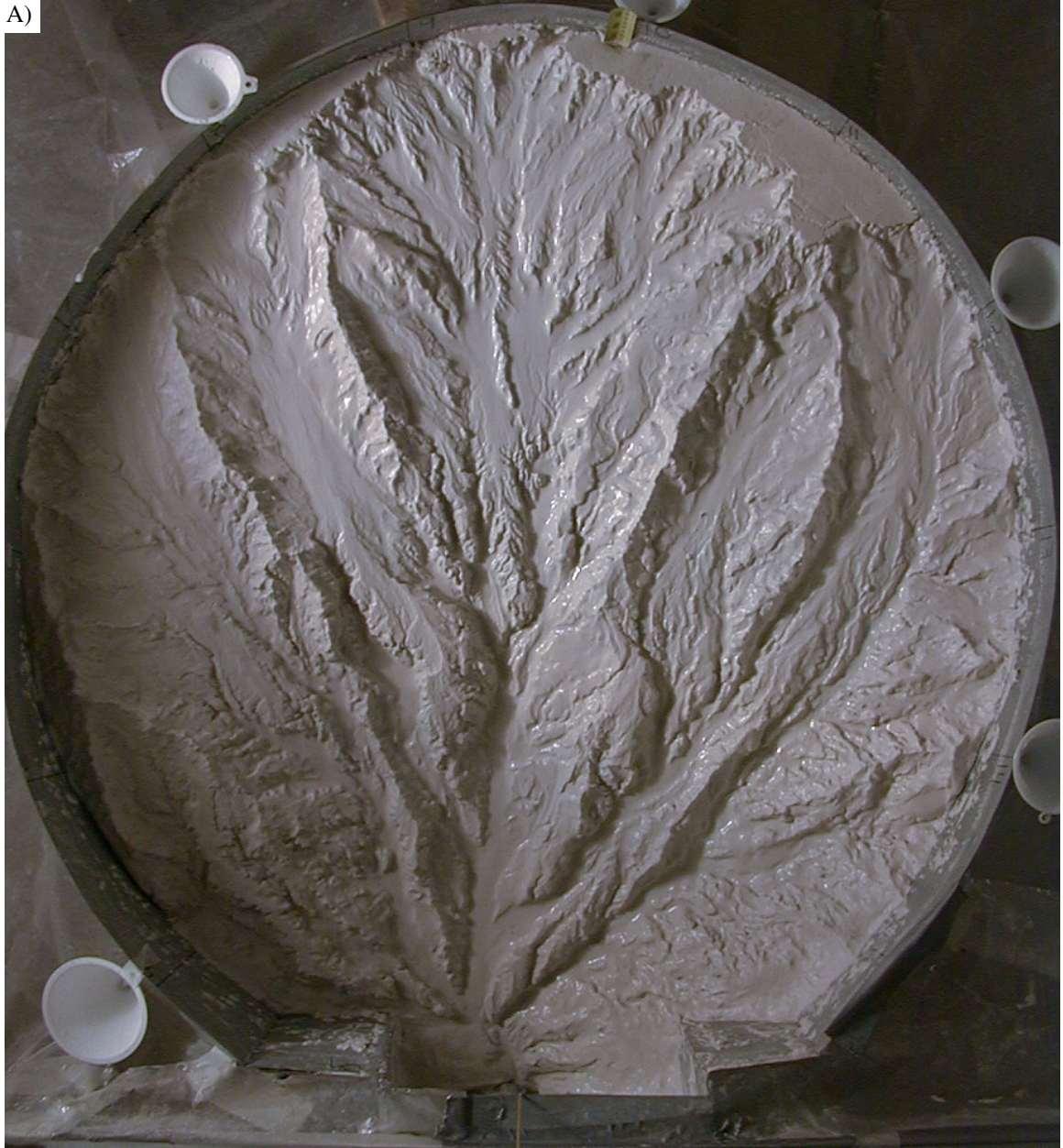
Figure 2-22. A) Surface nearing complete dissection. Basin width is 87 cm. Three major knickpoints are visible, one near the top of the photograph, another just above center, and a final one just below center.

Figure 2-22. B) Surface after additional 1 relief unit of erosion. Two knickpoints are visible below center and another closer to the outlet. Scalloped ridge crests, indicative of hillslope failures, are visible along the longer ridge in the left of the photograph. Terraces are visible in the lower right hand drainage.

Table 2-4 Run 3 Rainfall Spatial Distribution

average (μm/s): 6.1

standard deviation (μm/s): 0.3

coefficient of variation: 0.05

collection time: 7275 seconds

beaker area = 37.4 cm^2 (*n* = 30)

x ground coordinate across top row, cm

y ground coordinate down left column, cm

for reference, outlet is located at *x* = 45, *y* = 0

	10	26	41	57	72
10	6.0	5.6	5.9	6.6	5.9
26	5.8	5.7	6.1	6.3	6.5
41	5.7	5.9	5.9	6.3	6.1
57	6.2	6.2	6.1	6.2	6.2
72	6.1	6.4	5.8	6.2	6.6
88	5.6	5.9	6.0	6.1	6.7

Run 4

   Run 4 represents a case where rainfall rate ($r = 6.2$ μm/s) exceeds uplift rate ($u = 0.55$ μm/s) by a significant amount ($r/u = 6.6$). Uplift rate was substantially lower than previous runs.

   Sediment ($D_{50} = 45$ μm) and kaolinite were mixed (100:1 by weight) in a cement mixer with water, and poured into the basin (dry bulk density = 1.69 g/cm^3), and allowed to settle for 2 days. Rainfall spatial distribution was collected, and the run was initiated the following day (substrate sat for three days after mixing). Rainfall spatial distribution was moderately uniform, with spatial coefficient of variation of 8% ($\sigma/\mu * 100$; Table 2-5, p. 75). Over three units of steady state relief (3.4 H_r) were eroded after complete dissection of the initial flat surface.

   The experiment ran continuously from July 31 to September 17, 1999. Initial dissection occurred during a fixed base level after the outlet had lowered 9 cm, as repairs were conducted on the gearbox for the motor-controlled outlet. Relief at dissection was ~9 cm. Relief increased upon initiation of base level fall, and a steady relief was achieved after an additional 9 cm of erosion. After this initial problem, the run was conducted at quite stable forcing conditions (Fig. 2-23, p. 71), and runoff, sediment flux, and relief exhibited minor variability. Some variability in base level fall occurred ~ 510,000 s, a result of stick-sliding of the outlet. A new load cell for the fluxometer was installed at time = 1,270,000 s, or base level = 25.8 cm, due to unstable mass measurements. The noticeable peak late in the run is due to a piece of angle iron falling into the basin like a spear. Following this disruption, valleys widened substantially as parts of the substrate started to flow. No topographic data sets reported herein were taken following the perturbation.

   Visual inspection of photographs (Fig. 2-24, p. 72-74) taken during this run reveal a landscape with highly irregular ridge crests, and numerous well-defined sub-basins. Trunk valleys are narrower than prior runs, and streams often occupied narrow channels within the valley. Occasional hillslope failures were observed. One slump clearly dammed a channel (Fig. 2-24, C).
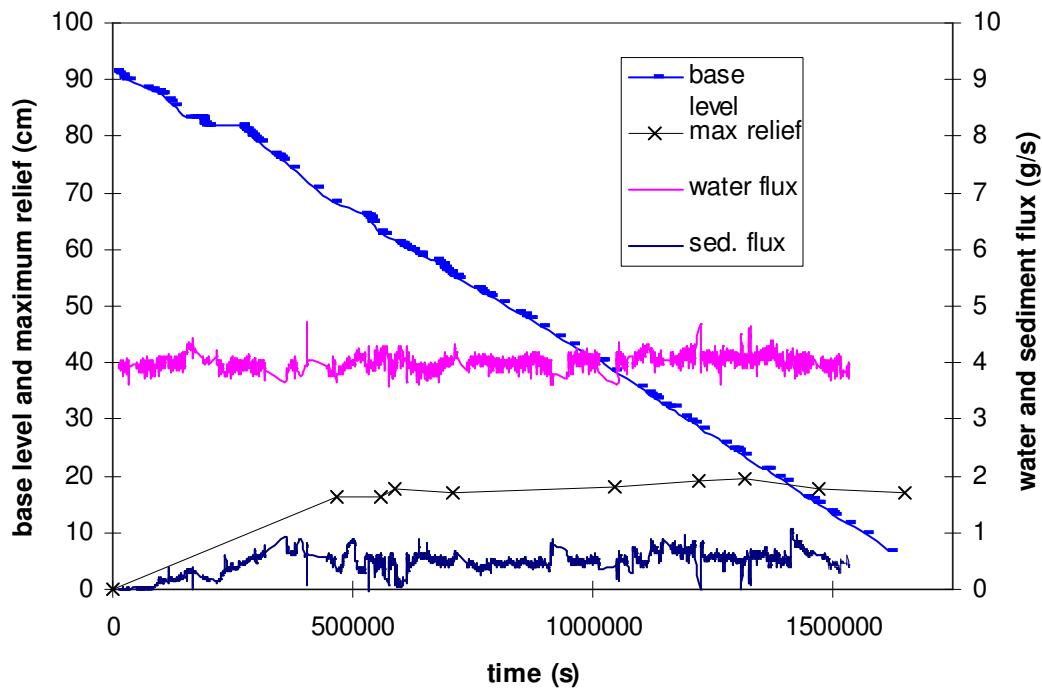
Figure 2-23. Forcing conditions, outlet fluxes, and relief for run 4. Flux measurements were determined by an automated sediment and water flux measurement device. Measurement errors (2 σ) for fluxes are ~2%, for base level measurements 0.2 mm, and for relief 1 cm. Minor stick-sliding of the outlet occurred early in the run, prior to complete dissection. Steady state conditions, marked by the development of constant relief (17.7 cm), were reached at 490,000 s. Over three relief units (3.4 H_r) of the landscape were eroded after reaching steady state conditions.

Figure 2-24. A) Surface nearing complete dissection, run 4. Hillslopes appear rather smooth, with concave hollows at valley heads. Width of the basin is 87 cm.

Figure 2-24. B) Surface after an additional 22 cm of erosion (1.3 H_r).

Figure 2-24. C) Surface after additional 18 cm of erosion (1 H_r), run 4. Drainage divides are irregular and crenulated. Many channels appear quite narrow. A long narrow terrace has formed in the lower left center trunk stream. A hillslope failure is visible (smooth 'creamy' area, long left center ridge) that has dammed a channel. Width of the basin is 87 cm.

Table 2-5 Run 4 Rainfall Spatial Distribution

average (µm/s): 6.2

standard deviation (µm/s): 0.5

coefficient of variation: 0.08

collection time: 1200 seconds

pan area = 22.9 cm^2 (n = 56)

x ground coordinate across top row, cm

y ground coordinate down left column, cm

for reference, outlet is located at $x = 45$, $y = 0$

	5	16	27	38	49	60	71	82
15			6.3	7.1	7.4	7.2		
26		6.8	7.1	7.1	7.1	7.1	6.7	
37	6.0	6.5	6.5	6.7	6.7	6.6	6.0	5.2
48	6.2	6.5	6.5	6.5	6.7	6.8	6.2	5.6
59	6.1	6.0	5.9	6.1	6.1	6.2	6.0	5.4
70	6.0	6.0	5.8	5.9	6.1	6.3	6.2	5.5
81	5.6	5.9	5.9	5.9	6.1	6.3	6.2	5.8
92		5.3	5.6	5.7	5.9	6.0	5.8	

Run 5

Run 5, conducted discontinuously over a period of time from May 19 to June 4, 2000, was designed to test whether similar landforms develop with similar r/u numbers, while the magnitude of the rates of rainfall and uplift differ between experiments. A new mist apparatus was installed to generate higher rates of rainfall ($r = 13.5$ μm/s). Rainfall spatial distribution was moderately uniform, with spatial coefficient of variation of 11% ($\sigma/\mu * 100$; Table 2-6, p. 83). Uplift rate ($u = 1.2$ μm/s) was adjusted to match the water-to-rock ratio for run 4 ($r/u = 6.6$ for run 4; $r/u = 6.5$ for run 5). The magnitude of the forcing was approximately double that for run 4.

Sediment ($D_{50} = 45$ μm) and kaolinite were mixed (100:1 by weight) in a cement mixer with water, and poured into the basin (dry bulk density = 1.69 g/cm^3), and allowed to settle for 3 days. Rainfall spatial distribution was collected in pans distributed over the top of the basin, and the run was initiated the following day (substrate sat for four days after mixing). Over four units of average relief (4.6 H_r) were eroded after complete dissection of the initial flat surface.

This run experienced large unplanned temporal variations in the applied rainfall (time = 350,000 to 450,000 s; Fig. 2-25, p. 77), due to extreme fluctuations in laboratory water pressure. Further, the early part of the run experienced stick-sliding of the outlet, and a very low relief drainage basin developed (Fig. 2-26, p. 78-80; relief = 14.2 cm). Additionally, an unplanned stepwise base level fall occurred in this run (time = 330,000 s; Fig. 2-25).

The latter portion of this run, however, did experience uniform rainfall and baselevel fall conditions for ~1 H_r. Photographs of the surface at the end of the run (Fig. 2-27, p.81; Fig. 2-28, p. 82) show ridges that are rough and crenulated, similar to run 4. Maximum relief is very similar between the runs. However, the valleys are smoother and wider than in run 4. Hillslope failure scars are not readily observable on photographs from this run. Knickpoint development and propagation, however, was quite common, especially in the latter portion of this run.
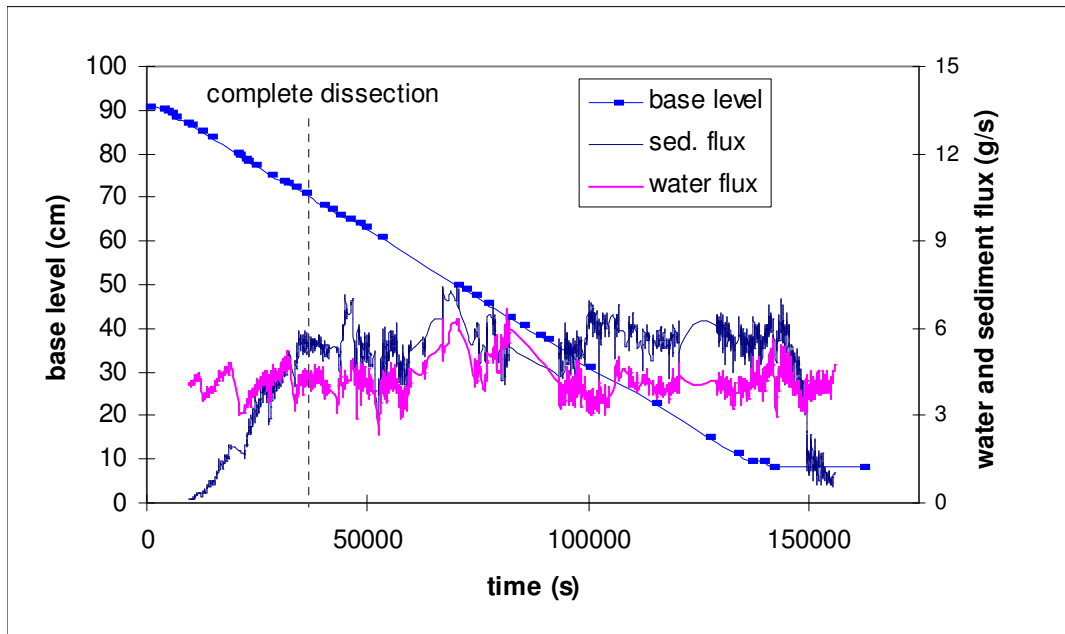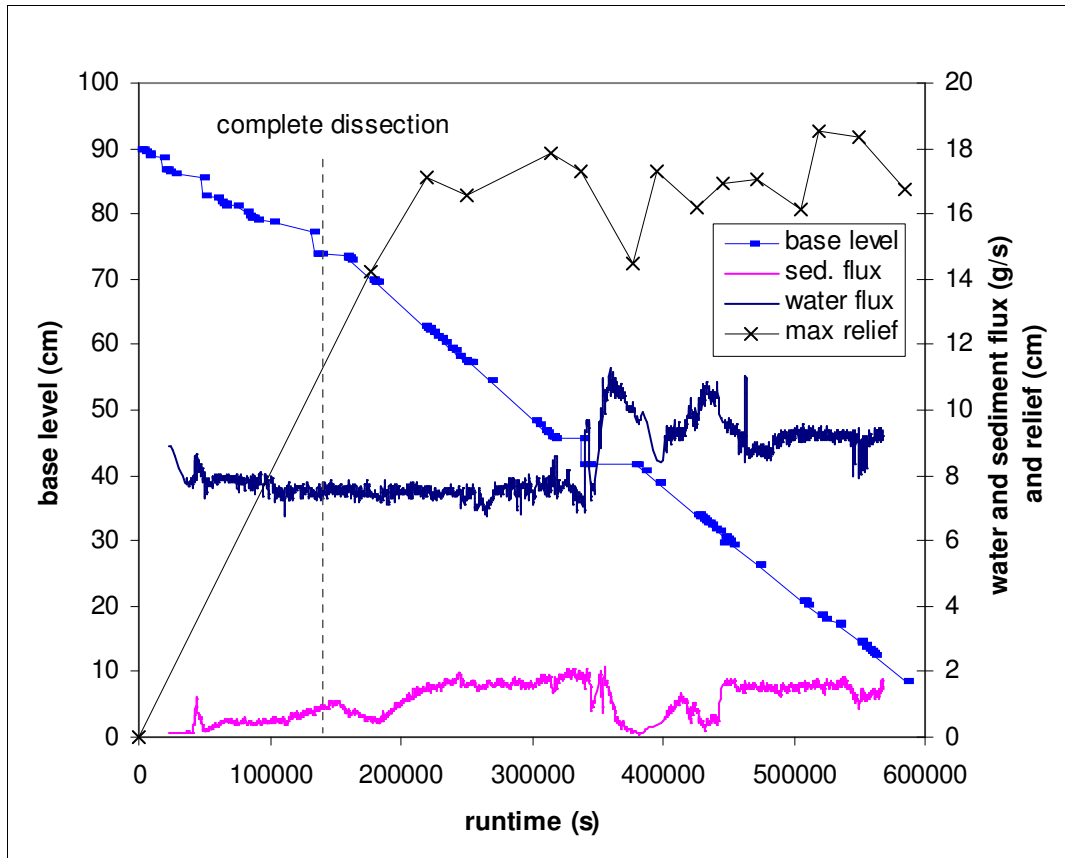
Figure 2-25. Forcing conditions, outlet fluxes, and relief for run 5. Flux measurements were determined by an automated sediment and water flux measurement device. Measurement errors (2 σ) for fluxes are ~2%, for base level measurements 0.2 mm, and for relief 1 cm. Nearly four relief units (3.8 H_r) of the landscape were eroded after complete dissection. However, only the latter portion of the run represented truly stable forcing, and ~1 H_r was eroded during that time. Relief oscillated significantly in response to changes in rainfall and base level fall conditions.

Figure 2-26. A) Surface at complete dissection, run 5. Hillslopes are smooth. Flow directions are strongly directed toward the outlet. Maximum relief is 14.2 cm. Width of basin is 87 cm.

Figure 2-26. B) Surface after an additional 20 cm of erosion (1.2 H_r), a long pause in base level fall, and subsequent initiation of steady run conditions (time = 395,000; Fig. 2-25). Maximum relief is 17.2 cm.

Figure 2-26. C) Surface at the end of the run, run 5. Ridges are rough and crenulated. Maximum relief is 18.3 cm.

Figure 2-27. Low angle photograph of surface at the end of run 5. Width of image is approximately 30 cm. Note tape measure at top left. Numbers on left of tape are inches and on right of tape are cm. A knickpoint is visible in the main channel on the left side of the photograph. Terrace-like structures were left in the wake of the knickpoint. Note the 'peaky' nature of the ridges, and the smooth valley floors.

Figure 2-28. Oblique view of the surface at the end of run 5, demonstrating the crenulated, rough character of the ridges. Width of view is approximately 50 cm. A knickpoint is barely discernible in the bottom right center. This same knickpoint is seen more clearly in Fig. 2-27.

Table 2-6 Run 5 Rainfall Spatial Distribution

average (μm/s): 13.5

standard deviation (μm/s): 1.4

coefficient of variation: 0.11

collection time: 480 seconds

pan area = 22.9 cm^2 ($n = 25$)

x ground coordinate across top row, cm

y ground coordinate down left column, cm

for reference, outlet is located at $x = 45$, $y = 0$

	0	20	40	60	80
10	10.1	12.8	15.2	15.2	13.4
30	11.6	13.4	15.1	15.3	12.5
50	11.6	12.8	13.8	14.3	12.3
70	13.4	13.7	13.5	14.7	12.5
90	16.5	14.8	12.6	13.4	12.4

Run 6

This run was designed to duplicate run 5, minus the perturbations. The base level fall rate (u = 1.0 μm/s) was ~83% of the rate in run 5, while the rainfall rate (r = 13.4 μm/s) was unchanged, yielding r/u = 8.4. The experiment was conducted from July 27, 2000 to August 7, 2000, and ran continuously. Stable forcing from uplift and rainfall for long time periods is demonstrated by the base level curve, and sediment and water fluxes at the outlet (Fig. 2-29). Rainfall spatial distribution was moderately uniform, with spatial coefficient of variation of 13% (σ/μ * 100; Table 2-7, p. 91). Minor stick-sliding of the outlet occurred at 225,000 and 360,000 s (Fig. 2-29, p. 85), and a minor abrupt drop in base level occurred near the end of the run (~1 cm), due to clearing of an obstruction in the outlet weir. The surface was completely dissected at ~160,000 (see Fig. 2-30 A for a photograph of surface, p. 86). An average balance between erosion and uplift was achieved by 250,000 s, and a steady state relief was achieved at ~360,000 (Fig. 2-29, p. 85). Nearly four relief units (3.8 H_r) were eroded at steady state relief conditions. Representative vertical (Fig. 2-30, B and C, p. 87-88) and low angle (Fig. 2-31, p. 89) photographs of the surface under steady relief conditions document smooth valleys, and pronounced profile concavity near ridge crests. After the outlet had reached the base of the tank, the landscape was eroded to a negligible erosion rate. A skeletal framework of drainage divides and smooth valleys developed (Fig. 2-32, p. 90).

The dominant erosion process was surface runoff and knickpoint development and propagation. Few hillslopes failures are observable from time lapse video and photographic records. Overall, the surface appears smoother in this run, compared to runs 4 and 5. Ridge migration was a significant aspect of this run. Comparison between Fig 2-30 B and C shows that a valley trending across the basin center to the upper right has experienced encroachment from adjacent divides that resulted in valley annihilation. A ridge now occupies the former valley location.
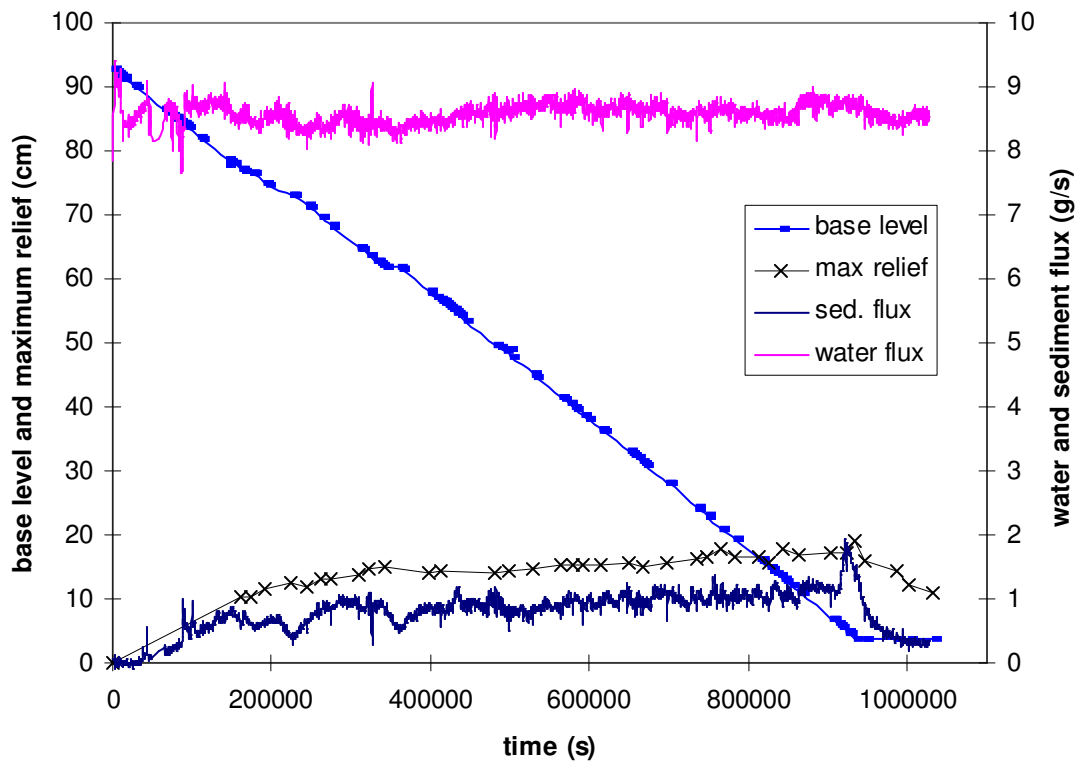
Figure 2-29. Forcing conditions, outlet fluxes, and relief for run 6. Flux measurements were determined by an automated sediment and water flux measurement device. Measurement errors (2 σ) for fluxes are ~2%, for base level measurements 0.2 mm, and for relief 1 cm. The surface achieved complete dissection at ~160,000s. Steady relief developed by ~275,000 s. Nearly four (~3.8) relief units (H_r) of the landscape were eroded at steady relief conditions. Large spike in sediment flux near the end of the run is due to a 1 cm drop in base level as material stuck in the outlet weir was removed. Maximum relief at the end of the run, when erosion approached nil, was 10 cm.

Figure 2-30. A) Surface nearing complete dissection, run 6. Note the remnant plateau at the top of the photograph. Maximum relief is 12.7 cm. Basin width is 87 cm.

Figure 2-30. B) Surface after an additional 22 cm of erosion, run 6. Maximum relief is 14.3 cm.

Figure 2-30. C) Surface at the end of the steady forcing portion of run 6. Maximum relief is 16.8 cm.

Figure 2-31. Close-up view of surface at steady forcing from rainfall and uplift, nearing the end of the run. Lines are projected from a slide projector. Width of view is approximately 40 cm. Surface is relatively smooth.

Figure 2-32. Declining relief phase at fixed base level, run 6. Width of image is ~40 cm. Surface is very smooth, with a skeletal ridge network. Local relief is 1-2 cm, and the maximum relief is ~11 cm.

Table 2-7 Run 6 Rainfall Spatial Distribution

average (μm/s): 14.3

standard deviation (μm/s): 1.9

coefficient of variation: 0.13

collection time: 670 seconds

pan area = 22.9 cm^2 ($n = 48$)

x ground coordinate across top row, cm

y ground coordinate down left column, cm

for reference, outlet is located at $x = 45$, $y = 0$

	10	20	30	40	50	60	70
6		13.9	14.6	16.5	13.3		
18		15.3	14.9	14.3	13.7	12.6	
30	15.2	14.5	13.9	13.8	13.3	11.8	10.4
42	15.5	15.2	15.1	14.9	13.7	12.5	10.2
54	15.5	15.7	16.0	15.9	14.1	12.3	9.6
66	15.9	15.6	15.9	15.1	14.5	12.7	10.0
78		16.3	16.4	16.1	14.9	13.8	11.1
90		16.3	16.5	17.3	16.7	15.0	

Run 7

This run was designed to investigate the effect of high and spatially variable rainfall rates on landscape form and erosional behavior. In prior runs, increasing runoff appeared to generate wider valley floors. Hence, an extreme case of runoff would place an upper limit on drainage basin form and erosional process activity for the substrate. All of the previous runs had developed streams with laminar flow, and the plan was to raise the Reynolds number to turbulent conditions for this run by increasing runoff.

A new rainfall mist arrangement was constructed, with a line of misters on opposing sides of the tank (Fig. 2-33, p. 95). Substantial variation in spatial rainfall patterns resulted from the new arrangement. The average rate was varied deliberately during the course of the run by changing mist nozzle sizes, and the rate further varied due to pressure oscillations in the lab water supply. Table 2-8 (p. 101) lists the pertinent uplift and rainfall rates and duration of the conditions. Rainfall rate was computed by taking advantage of the runoff record from the flux-o-meter. The runoff rate (in g/s) was multiplied by the density of water, and divided by the basin area. Groundwater is a component of the runoff leaving the tank, as the landscapes erodes material containing solid particles and interstitial water. An adjustment for the contribution of groundwater was made as follows. The uplift rate was multiplied by the difference between the density for quartz (2.65 g/cm^3) and the bulk density of the substrate (1.75 g/cm^3), then multiplied by the density of water, divided by basin area, and subtracted from the total runoff rate. Spatial variation in rainfall was measured at the beginning of the run (Table 2-9, p. 102), at t = 137,000 s during the run (Table 2-10, p. 103), and after the run was finished (Table 2-11, p. 104). The initial mister configuration exhibited a spatial coefficient of variation of 39%, with a range in rainfall rates from 12 to 110 μm/s. The adjusted configuration (from 66,000 s to the end of the run) exhibited a coefficient of variation ~55% ($n = 29$), with a range in rainfall rates from 13 to 77 μm/s. The highest rates (~100 μm/s) developed in the upper center of the basin, and the lowest rates (~10 μm/s) occurred near the outlet.

The base level fall rate was initially set at 4.2 μm/s (r/u = 6.7), and was then reduced to 2.9 μm/s from 60,000 to 180,000 s to maintain an approximately similar r/u as the initial portion of the run. The uplift rate was later increased again to 5.5 μm/s at 180,000 s for the duration of the run (see Fig. 2-34 for base level curve, maximum relief, sediment, and water flux time series, p. 96).

Erosional processes were dominated by surface runoff, though a few significant mass movements (~30-50 cm^2) on hillslopes were observed. Scour holes occasionally developed in trunk streams during this run, with visible vortices in the flow. Streams often had standing wave trains with ~1 mm wave heights. Epicycles of temporary sediment storage followed by knickpoint development and migration was a significant aspect of this run. Knickpoint migration rates of ~ 1-10 mm/s were observed during the run. Knickpoint propagation varied, at times extending only short distances (10-20 cm) up trunk streams before dissipating, at others propagating to the farthest upstream reaches. Estimates of Reynolds and Froude numbers at the outlet weir indicate turbulent and supercritical flow conditions (*Re* of 6270; *Fr* of 1.7).

Maximum relief for this run was recorded from a tape measure appearing on the rear (upstream) wall of the basin, and the location of the outlet. At no period does the relief attain a constant value for this run (Fig. 2-34). After a rapid increase in relief during dissection of the initial flat surface, the relief continued to grow and oscillate. Following a 36% decrease in base level fall rate and a coincident 25% decrease in rainfall rate at 60,000 s, the relief continues to grow. The relief curve is marked by an increasing rate of growth at 180,000 s as the base level fall rate was increased by 53%. Clearly this run never reached a statistical steady state, either in terms of attaining a constant relief, or in terms of a steady erosional flux at the outlet.

The photographic record reveals several interesting aspects of erosion in this run. Two dominant valleys formed early in the run, with a long ridge running down the center of the tank (Fig. 2-35, p. 97). The right hand sub-basin (viewed upstream from the outlet) was initially somewhat larger than the left, and the upper reaches in basin were smooth with low relief (Fig. 2-35, p. 97, Fig. 2-36, p. 98). After decreasing the rainfall (26%) and

base level fall rate (36%) at 60,000 s, the central divide rapidly migrated from left to right (Fig. 2-37, p. 99). Subsequently, a small sub-basin formed in the center of the tank by the outlet, and slowly extended upward into the basin for the remainder of the run. The two larger sub-basins gradually shifted toward the edges of the basin (Fig. 2-38, p. 100).

Figure 2-33. Rainfall apparatus arrangement, run 7. Four misters on the left and five on the right side (not in view) of erosion facility generated a higher intensity rainfall. Two different nozzle orifices were used. Changing the orifice size changed both the intensity and spatial distribution of rainfall.
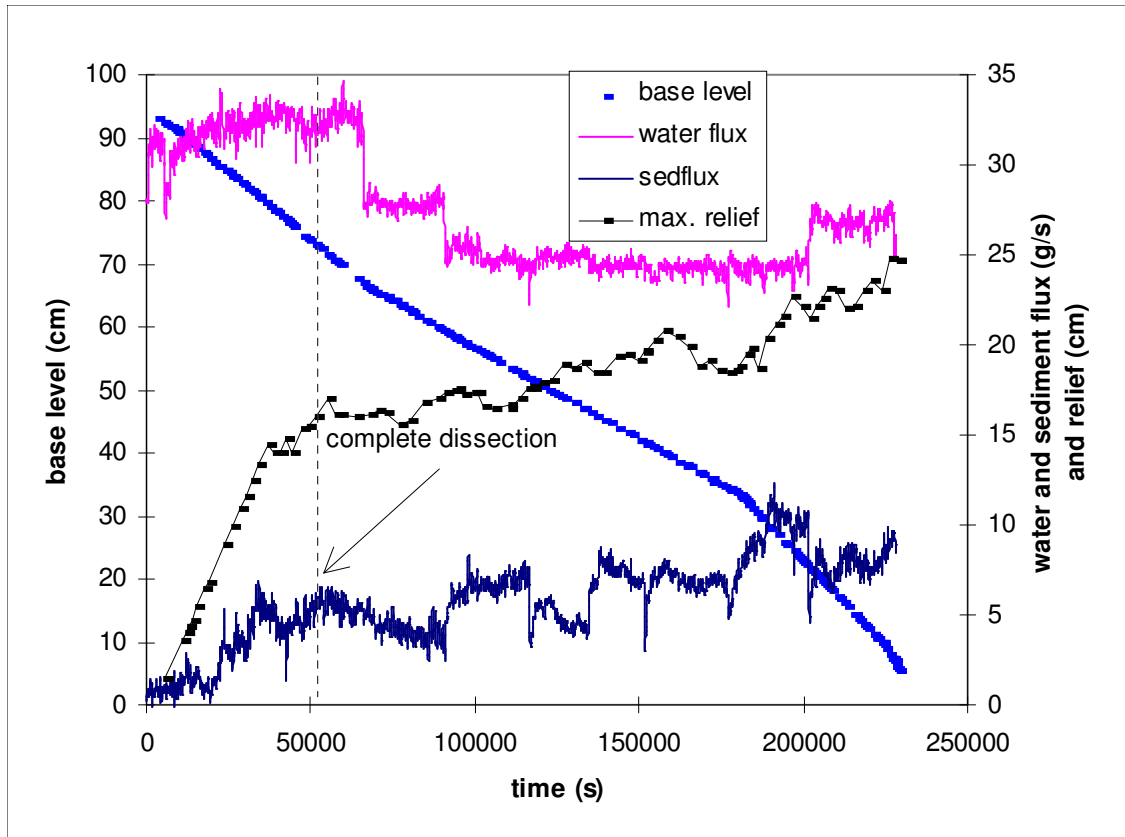
Figure 2-34. Forcing conditions, maximum relief, and sediment flux for run 7. Flux measurements were determined by the flux-o-meter, with 2% measurement errors (2 σ). Three separate base level fall rates were imposed (note breaks at ~60,000 and 170,000 s), and the mist apparatus was altered a single time at ~60,000s (at the abrupt drop in the water flux curve). Subsequent stepwise changes in the water flux curve (a drop at ~90,000 and abrupt rise at ~210,000 s) are not readily explained. Sediment flux oscillations are only somewhat correlated with stepwise changes in the water flux record.

Figure 2-35. Surface at complete dissection, and prior to the adjustment to the mist apparatus at t = 66,000 s. Width of basin is 87 cm. Two main sub-basins have developed. Knickpoints are visible in both main trunks in the center of the basin. Note the smooth character of the surface upstream from the knickpoints. Large spatial variation in rainfall rates exist for this run, with the highest rates (~100 μm/s) in the upper center of the basin, and the lowest rates (~10 μm/s) occurring near the outlet.

Figure 2-36. Surface just prior to the mist apparatus adjustment at $t = 66,000$ s, run 7. Note the smooth character of the right side sub-basin. A scour hole is visible in the right side trunk stream where flow converges from several sub-basins. In general, the roughest regions correspond to the lowest rainfall rates.

Figure 2-37. Surface after mist apparatus adjustment, run 7 (~3 cm of erosion has occurred). Width of basin is 87 cm. The center ridge has migrated toward the right side of basin, which has roughened considerably. The upper left of the basin has smoothed.

Figure 2-38. Surface just prior to cessation of base level fall, run 7. Width of basin is 87 cm. Lower center portion of basin has roughened considerably as a new sub-basin has grown upstream from the outlet. The two large trunk streams have migrated toward the edges of the basin. Smoothest regions of topography also mark the locations with the highest rainfall rates.

Table 2-8 Forcing conditions for Run 7

runtime (start, s)	runtime (stop, s)	uplift rate (mm/s)	rainfall rate (mm/s)	r/u	eroded distance (cm)
0	66000	4.3	47.1	6.3	25.7
66000	90700	2.9	41.3	8.0	7.2
90700	103780	2.9	37.3	7.3	3.8
103780	180300	2.9	36.1	7.0	22.3
180300	201600	5.5	34.3	3.5	11.7
201600	227600	5.5	38.3	3.9	14.2

Table 2-9 Run 7 Rainfall Spatial Distribution, beginning of run

average (μm/s): 49

standard deviation (μm/s): 21

coefficient of variation: 0.42

collection time: 120 seconds

pan area = 24.6 cm^2 ($n = 42$)

x ground coordinate across top row, cm

y ground coordinate down left column, cm

for reference, outlet is located at $x = 45$, $y = 0$

	0	15	30	45	60	75	90
0			33	42	50		
15		42	50	67	58	50	42
30		42	58	75	67	58	42
45	17	33	50	75	83	58	50
60	33	42	50	67	75	58	42
75	17	42	42	58	117	46	42
90		17	25	42	83	42	33

Table 2-10 Run 7 Rainfall Spatial Distribution, during run at t = 132600 to 136560 sec.

average (μm/s): 35.2

standard deviation (μm/s): 17.4

coefficient of variation: 0.50

collection time: 100-150 seconds

pan area = 46.6 cm^2 (*n* = 21)

x ground coordinate across top row, cm

y ground coordinate down left column, cm

for reference, outlet is located at *x* = 45, *y* = 0

	10	20	40	60	80
15			12.9		
20		14.3	15.7	15.7	
30	19.3	17.2	20.0	25.8	27.2
50	45.1	45.1	42.9	42.9	35.4
70	50.1	63.5	77.3	51.5	36.5
85				38.7	
90			40.8		

Table 2-11 Run 7 Rainfall Spatial Distribution, end of run

average (μm/s): 26.7

standard deviation (μm/s): 14.7

coefficient of variation: 0.55

collection time: 100-150 seconds

pan area = 46.6 cm^2 (n = 30)

x ground coordinate across top row, cm

y ground coordinate down left column, cm

for reference, outlet is located at $x = 45$, $y = 0$

	0	20	40	60	80	90
0	5.2	14.6	27.2	30.4	12.5	
20	13.4	16.5	14.3	14.3	20.6	
40	19.7	26.6	26.8	28.6	27.5	26.8
60	28.6	57.3	60.8	51.9	36.7	24.8
80	20.6	77.8	64.4	46.5	39.4	
90		34.9	38.5	42.1		

Chapter 3

Topographic Form of Eroding Landscapes

Introduction

This chapter presents statistical measures of eroding topography. The first section will cover a comparison of elevation fields derived from the experimental landforms. The purpose here is two-fold: document the range in form of eroding landforms under steady forcing (that is, how variable is a landform during each run), and note the changes in form due to forcing conditions. The following section will compare elevation fields from the numerical erosion model and selected natural drainage basins against the physical experiments. The intent of this chapter is to examine the range of form in eroding landscapes, place some constraints on the utility of statistical comparison, and identify both the features these landforms share, as well as differences.

Run Comparison

In the run description section, differences in gross topographic form were noted between runs with different forcing conditions. Maximum relief for steady state conditions varied from 16 to 28 cm. Qualitative observations of local relief and surface roughness, channel shape, and drainage density suggest that these features are sensitive to applied uplift and rainfall rates. The dominant erosion processes include surface runoff, hillslope failures, and upstream migrating knickpoints. The size and frequency of hillslope failures, and knickpoint characteristics, such as height, recurrence, and migration rate appeared to vary between runs. For runs with smaller water-to-rock ratios (r/u), hillslope failures increase in size and occurrence. The fastest recorded knickpoint migration rates (~ cm/s) occurred for high sustained flow rates (~30 cm^3/s). Unfortunately, this thesis was not focused on measuring process activity, and detailed data sets of process activity can not be presented. Instead, topography and statistics derived therefrom (maximum and local relief, local relative height, slope, upstream drainage area) will be presented.

The data sets are taken during times of steady forcing and depict steady landscape forms, and allow both a comparison between landscapes at different forcing conditions,

as well as a measure of landscape variability at steady forcing conditions (see Table 3-1 for the number of data sets for each run, p. 115). Chapter 2 presents the methodology behind the derivation of the elevation fields and statistical measures. The statistics reported below capture various aspects of the landform. Such measures, when plotted against the forcing conditions, yield some insight into both the form, and the behavior of eroding steady state landscapes.

Hypsometric Curves

Hypsometric curves for runs 1-7 are plotted in Fig. 3-1 (p. 118). Each curve represents the run-averaged distribution over each bin interval (15 bins) of elevation (elevation range is divided into 15 bins, and the number of points higher than the bin midpoint are counted, and normalized to the total number of points). The curves have been organized such that they follow the order in the legend (i.e., run 3 is the top curve, run 1 the bottom). Each run exhibited some variability in hypsometry. Error bars of the standard deviation of the frequency for each binned interval are plotted on the curve for run 4. Other runs exhibited similar ranges for the hypsometric curve. The range in hypsometry implies minor changes in the mass distribution of the landform during the course of a run, and could be a result of temporary sediment storage, or knickpoint migration through the network. A useful summary statistic that can be taken from each curve is the value of a/A at $h/H = 0.5$. This number was recorded for each run, and has been plotted together with other summary statistics against the forcing conditions later in this chapter. Overall, hypsometry reveals a continuous change in elevation over the experimental basin. No plateau or other clumping of elevations is evident in the curves.

Local Relative Height Distributions

Local relative height is a measure that ranks each cell according to its height amongst its neighbors. This form of ranking, when plotted as a gray scale bitmap, captures the ridge and valley structure of the surface. The measure is sensitive to random roughness, and larger windows are required to elucidate structure for very rough surfaces. As a reference, a random height field yields an even distribution of relative height values (no central peak in the distribution). Distributions of relative height values were computed for

each data set, and the average local relative height distribution for each run appears in Fig. 3-2 (p. 119). Within run variability is modest, with a coefficient of variation (σ/μ) of 0.04 for each bin interval. The distributions represent surfaces with more neighbors that are higher than lower (average value is 0.45, meaning that on average 55% of the neighboring cells in the moving window are higher). This implies a surface with converging flow. The legend is ordered from top to bottom according to peak values (run 3 has a larger number of cells with values ~0.45, run 7 has a smaller number of cells with values ~0.45). Thus ordered, the sequence is different than that observed for hypsometry, suggesting the two statistics are capturing different information. The general trend is a decrease in distribution peak frequency with *r/u*.

One can integrate the local height frequency distribution over appropriate ranges to obtain the fractional area of the surface occupied by cells likely to be stream locations (most neighbors are higher) and ridges (most neighbors are lower). Arbitrary ranges were chosen for valleys (all values < 3/8) and ridges (all values > 5/8). Changes in the total numbers of ridges and valleys, thus defined, give an indication of changes in drainage density (Fig. 3-5, p. 122).

Slope Distributions

Average slope distribution curves for each run appear in Fig. 3-3 (p. 120). The distributions are slightly asymmetric, with longer tails at larger slope values. Slope distributions vary systematically between runs. Runs 1-3 have broader distributions, with greater numbers of steep slopes. These runs all were conducted at *r/u* <1. Runs 4-7 have narrower slope distributions (*r/u* >5). Error bars on run 4 represent one standard deviation ranges in bin midpoints and relative frequency (n = 9). Other runs exhibit similar variability in slope distributions. In general, slope decreases with *r/u*, with the number of lower slopes increasing at the expense of steeper slopes. Slope is very sensitive to the quality of the data. Data derived from photogrammetric methods exhibit abrupt steps in elevation. The smallest change detectable is ~0.5 to 1.5 cm (depending on camera height and field of view). Smoothing the data sets to eliminate steps blurs detail, and substantially effects slope distributions. This issue can not be resolved. However, because

the same set of elevation extraction methods were applied to all runs, systematic changes in slope distributions between runs are real. The absolute values of slope, however, are still somewhat uncertain. The distributions reported here are for data sets with a minimal amount of processing. Extreme slopes (locations with slopes > 200% and < 1%) have been filtered and elevations replaced with local averages. Filtered locations tend to occur in valley areas, and could result from faulty stereo photographic correlations around reflections off water surfaces.

Area-Slope Relation

Area-slope curves are a commonly used relation to describe the drainage structure of natural drainage basins. They capture the decrease in slope in downstream sections of the drainage basin. For each elevation data set, steepest descent slopes were computed on a cell by cell basis, then a routing algorithm starting at each cell followed the steepest descent direction to a depression. A running sum was kept of the number of times a cell was visited during the routing process. Because this algorithm halts at a depression, the total flow through a cell can sometimes be underestimated. An additional routing routine was employed that moves past the depression to the nearest cell not draining back into the depression. The outlet should represent a single depression for the erosion facility. In practice, the region near the outlet was not included in the extracted elevation grid. Often two or more streams would enter the area near the outlet, in effect creating two or three real depressions. Stereophotographic correlation and gridding artifacts also contribute to the formation of depressions. Of course, it is also possible that some depressions are real. For instance, run 7 developed small scour holes (~1 cm diameter) in trunk streams. Hillslope failures that form dams in streams are also real possibilities.

Once upstream contributing area has been determined, logarithmic values of upstream area and slope were computed and binned (8 intervals). The average value of area and slope are then plotted against each other (Fig. 3-4, p. 121). For runs 1-3, the curves appear to be straight lines. For the rest of the runs, the curves are not straight lines, but rather, exhibit increasing concavity in the relation. As a summary measure, trend lines were plotted for contributing areas < 1.5 log units, and the area-slope coefficient *(k)* and area-

slope exponent (θ) in the relation $S = kA^{-\theta}$ were extracted from the relation. While this threshold for area is somewhat arbitrary, individual data sets exhibit sharper breaks (See Fig. 2-12, p. 49, for a representative data set). Note, each slope value plotted in Figure 3-4 represents a binned average (in log space) for the contributing area. Bin averaging tends to smooth the relation.

Topographic Measures Plotted Against Forcing Conditions

Thus far the measures have just been arranged according to run identification number. In general, runs with similar water-to-rock ratios (r/u) shared similar statistical distributions. Initially, summary statistics were plotted solely against uplift rate or rainfall rate, but no clear relationship existed between topographic measures and forcing when plotted in this fashion. When plotted against r/u, however, systematic changes in measures become clearer (Fig. 3-5, p. 122). Summary statistics represent averages of the various measures for each run. Ranges (one standard deviation) in the measure appear as error bars in Fig. 3-5, and are listed in Table 3-2 (p. 116). The following summary statistics were collected and plotted:

1) the value of the hypsometric curve (a/A) at the elevation midpoint ($h/H = 0.5$);

2) maximum relief (H_r), defined by the range in elevation;

3) regional slope, defined by the linear regression coefficient for average elevation as a function of distance from the outlet;

4) local slope, computed as the steepest descent slope magnitude; averaged for each grid, then averaged again over the number of data sets for the run;

5) area-slope coefficient (k) in the relation $S = kA^{-\theta}$, where S is slope magnitude, A is contributing area;

6) area-slope exponent (θ) in the relation $S = kA^{-\theta}$;

7) valley area, in units of fractional basin area; and

8) ridge area, in units of fractional basin area.

Relief and slope capture related information in the landform, and both variables closely track each other when plotted against forcing conditions. The hypsometric curve value (a/A at $h/H = 0.5$) shows a marked decrease with r/u, then a gradual increase. This value

does not track any other variable, and hence is capturing a different aspect of the landform, namely, the topographic center of mass. Essentially, the topographic center of mass moves toward the outlet for higher *r/u* numbers. Valley and ridge area co-vary, with a general increase in with *r/u*. Comparing the decline in regional slope to the increase in valley and ridge area suggests that at lower *r/u* numbers, the surface is steeper, but less roughened by small valleys and ridges. Changes in valley area, while modest, nonetheless support qualitative observations of roughening at higher water-to-rock ratios. Values for measures are listed in Table 3-2 (p. 116), and ranges (the coefficient of variation, σ/μ) in reported values are given in Table 3-3 (p. 117).

It is worth noting that run 7 data does not appear in the plot of summary statistics (Fig. 3-5, p. 122) against forcing. This is because run 7 experienced a very large spatial range in long term rainfall rates, and hence it is not meaningful to plot against *r/u*. Indeed, run 7 data sets exhibit higher variability than the other runs (see Table 3-3).

The area-slope relation, based solely on topography, offers a means of extracting part (only the *ratio* of *m* and *n*) of the information required to calibrate an erosion law for a given landscape. At steady state conditions where erosion balances uplift, the stream power erosion law can be solved to obtain an equilibrium slope as follows:

$$\delta z / \delta t = U - k_e\, A^m\, S^n = 0 \tag{3-1}$$

rearranging and solving for S:

$$S = [U / (k_e\, A^m)]^{1/n} \tag{3-2}$$

and isolating *A*:

$$S = [U / k_e]^{1/n}\ A^{-m/n} \tag{3-3}$$

$$S = k\, A^{-\theta} \tag{3–4}$$

Equating exponents and coefficients in equations (3-3) and (3-4) yields

$$\theta = m/n \tag{3-5}$$

$$k = [U / k_e]^{1/n}$$

One test of the appropriateness of using the stream power law for a given landform is the lack of dependence of *m* and *n* on uplift (U) and the erosion coefficient, k_e. This test can be accomplished by extracting θ from the area-slope relation for steady state landscapes.

Breaks in the relation would imply that a single erosion law can not account for the downstream changes in slope. Several of the runs with higher water-to-rock ratios exhibit such a break in the area-slope relation. Additionally, the exponent θ should not vary between runs, or at least not systematically. However, the exponent θ varies between runs, and in systematic fashion (Fig. 3-6, p. 123). Values for θ range from 0.19 to 0.3 for $A < 50$ cm^2, and from 0.07 to 0.23 for $A > 50$ cm^2, implying that *m/n* is changing.

Comparing Models and Natural Drainage Basins

Investigating changes between erosion facility runs is a fruitful exercise, in that changes between runs can only be due to changes in the forcing conditions. However, an additional comparative study between physical and numerical models and examples from natural settings can also highlight aspects of similarity and difference. This section presents a topographic comparison between model landscapes and two drainage basins in the Sierra Madre Mountains of southern California. The natural drainage basins were selected visually based on their similar shape (elliptical), and completely dissected nature. Numerical model runs were selected based on one criterion, namely, that the relief attained in the model landscape approximated the relief in physical experiments.

As noted in Chapter 1, a numerical model was developed with similar boundary conditions as the physical experiment. A series of runs were conducted where uplift rates, rainfall rates, erosion law implementation, and erodibility of the substrate were varied between runs. The goal of this modeling effort was to demonstrate the stability achieved by numerical landscapes, and the sensitivity of the landscape form to forcing and erosion law implementation. Some of the numerical runs were not conducted for sufficiently long times to achieve the static steady landscape condition (most were run for only ~ 1 H_r of erosion after complete dissection). There is always a period of drainage structure rearrangement, often accompanied by divide migration, during the early phase of evolution (note: the initial surface is a randomly rough sloping surface). These adjustments always lead to a more stable configuration.

Elevation fields were extracted from two numerical model runs over the course of their evolution to stationary steady state. The simulations were identical except for that one of

the runs had a much larger diffusion coefficient. The same operations performed for all of the experimental data sets were applied to a data set from numerical model output. These model runs eroded through > 1 H_r of erosion after complete dissection. The numerical boundaries coincided with the physical experiment (dimensions in cm). Parameters in the erosion law $[\Delta z_{t+1} = \Delta z_t + \Delta t\ (U - K_1\ Q^m\ S^n + K_2\ S)]$ are $K_1 = 0.001$, $m = 0.25$, $n = 1$, $K_2 = 0.1$, $\Delta t = 50$ s, uplift rate (U) = 0.0001, and rainfall rate = 0.001 (maximum discharge at the outlet = 6.7 cm^3/s). Units of uplift and rainfall are in mm/s. These input parameters are of the same order of magnitude as the physical experiments. The exponents in the erosion law were chosen such that m/n =0.25, with $n = 1$, to approximate the downstream changes in slope observed in the area-slope relation from physical experiments. No constraints on n existed, so n was arbitrarily set equal to unity. The numerical landscapes developed a steady state relief (14 cm; A ~6400 cm^2; $L = 80$ cm; $H = 14\ /\ 80 = 0.18\ L$) approximately at the time of complete dissection. Gray scale maps of elevation from the numerical simulations (Fig. 3-7, p. 124; Fig. 3-8, p. 125) demonstrate a branching pattern, similar in appearance to elevation models of the physical experiment (Fig. 3-9, p. 126). The numerical model run with stronger diffusion developed higher relief and smoother hillslopes with lower drainage density.

Shaded perspective and gray scale elevation maps of mountainous drainage basins in the Sierra Madre Mountains of southern California, show dendritic structures similar to model landforms. The two basins are referenced herein as Madulce Peak (Fig. 3-10, p. 127) and Cuyama Peak (Fig. 3-11, p. 128). Data are freely available USGS 7.5 minute Digital Elevation Models (DEMs). Grid spacing is 30 m, relief for both basins is ~ 500 m, and there are > 10,000 data points in each basin (A ~10 km^2; $L = 3314$ m; $H = 500\ /\ 3300 = 0.15\ L$).

At first glance, these surfaces are quite similar. Relief, expressed as a fraction of the square of drainage basin area (L), ranges from 0.15 to 0.2 for the various data sets. All exhibit a branching stream network of approximately the same order. Numerical model data sets contained roughly one quarter of the points in both the natural and experimental

data sets, so some scale of observation issues exist for this comparison. How well do these data sets compare statistically?

Slope, hypsometry, local relative height, and area-slope relations were computed for the numerical model and natural drainage basins, and plotted next to data from physical experiments. The mass distribution exhibited by the hypsometric curve (Fig. 3-12, p. 129) shows that the experimental and numerical data are quite similar. The natural drainage basins exhibit a broader range in distributions than all of the experimental landforms, which clearly fall within the range of natural drainage distributions. While maximum relief and hypsometric curves compare favorably, such similarity is not replicated in other statistical measures.

The numerical landform local relative height distributions (Fig. 3-13, p. 130) more closely resemble the natural drainage basins. The peak in the distribution is clearly shifted to lower values for physical experiments, suggesting a slightly different structure to the surface overall. Whereas the average location in the physical experiment is a valley, (more highs surround the point), the average point in the numerical and natural basins is positioned with equal numbers of higher and lower points as neighbors.

Slope distributions (Fig. 3-14, p. 131) and area-slope relations (Fig. 3-15, p. 132) show that while the average slope in the numerical landform compares favorably with the physical experiments, the range in slope in the numerical landform is much narrower, lower slopes exist for the numerical run. The long tail in the physical experiments' slope distributions is absent in the numerical output, which is abruptly truncated. In fact, the slope distribution is more normally distributed for numerical data. Plots of the area-slope relation significantly overlap, though again with overall lower slopes in the numerical model. Of the natural drainage basins, Madulce Peak exhibits a similar slope distribution to the physical experiments, and Cuyama Peak shows a higher mean slope, with a longer tail for lower slope values. Both natural drainages show decreases in slope at downstream locations ($\theta \sim 0.27$) similar to model landforms ($\theta \sim 0.2\text{-}0.3$).

Overall, the striking visual similarity between these landforms is only partly borne out by statistical comparison. The most obvious difference is the limited range of slope

values for the numerical landforms. This could be an artifact of grid size, since they have less than half the numbers of points of the other landform data sets. Despite this limited range in slope, downstream changes in slope clearly are similar to the physical experiments, with only a slightly lower value of θ than natural landforms. The discrepancy in mean peak values in local relative height distributions between physical experiments on the one hand and numerical and natural basins on the other is curious. Apparently, hillslopes are the dominant landscape element for the latter, while mildly convergent flow regions are dominant in the former.

Summary of Topographic Comparison

For experimental data sets from the erosion facility, these measures of topographic form indicate that a *statistically* stable form develops for each run. This implies that the topography is adjusted to forcing conditions. In general, slope and relief decrease with r/u, and the area occupied by ridges and valleys increases with r/u, signaling an increase in drainage density. Local slope varies the most within a given run ($\sigma/\mu \sim 10\%$). Other measures exhibit less variability. Note run 7 exhibits the greatest variability in topographic measures. This is due to large variability in rainfall, as well as changes in uplift rate during the run.

Comparison of numerical, experimental, and natural drainage basins demonstrates that hypsometry and maximum relief, when scaled to the square root of basin area, can not distinguish differences between the data sets. Area-slope relations also have limited use in discriminating between the landforms. All data sets exhibit decreasing slopes downstream, and approximately in the same fashion, as θ varies only a small amount between data sets. The numerical landforms have slope distributions that are much more narrowly distributed (smaller range in slope), though this could be an artifact of grid resolution. Local relative height distributions, however, display some difference between the data sets. Mean local relative height values imply that valley-type locations dominate experimental landforms, while hillslopes are more common in numerical and natural drainage basins. The shift in mean values is small, but clearly outside the range of values for experimental landforms.

114

Table 3-1 Number of gridded data sets for each run, with run duration and base level fall.

run id.	run duration (s)	eroded distance (cm)	number of data sets
1	145206	43.8	10
2	220245	84.8	9
3	64520	82.9	3
4	1371600	88.1	9
5	584160	81.4	7
6	932400	88.9	15
7	584160	86.8	12

Table 3-2 Run conditions and topographic measures

run id.	r/u	r	u	H_r	a/A	local slope	valley area	ridge area	h'	reg. slope	θ_a	θ_b	log(k)	k
run 3	0.59	6.10	6.00	25.5	0.57	0.58	0.238	0.099	1.48	0.25	0.21	0.07	-0.26	0.55
run 2	0.80	3.86	2.80	24.1	0.50	0.58	0.250	0.114	1.33	0.23	0.25	0.23	-0.26	0.55
run 1	0.96	3.78	2.30	24.1	0.42	0.60	0.230	0.105	1.60	0.22	0.19	0.14	-0.26	0.55
run 5	4.97	13.47	1.58	17.1	0.53	0.47	0.281	0.136	0.91	0.18	0.24	0.12	-0.36	0.44
run 4	6.61	6.23	0.55	17.7	0.57	0.50	0.275	0.132	1.04	0.17	0.26	0.14	-0.34	0.46
run 6	7.82	13.40	1.00	16.5	0.57	0.42	0.277	0.127	0.97	0.16	0.31	0.14	-0.41	0.39
run 7	6.49	38.90	3.50	13.8	0.46	0.36	0.266	0.139	1.02	0.12	0.27	0.17	-0.51	0.31

h' is the mean standard deviation of elevation as a function of distance from the outlet.

valley area threshold < 3/8; ridge area threshold > 5/8.

θ_a is the exponent in the area-slope relation computed for $A < 50$ cm^2.

θ_b is the exponent in the area-slope relation computed for $A > 50$ cm^2.

k is the coefficient in the area-slope relation for θ_a, in units of slope.

r/u for run 7 is the average forcing for the run.

Table 3-3 Coefficients of variation (σ/μ) for topographic measures

	H_r	a/A	slope	valley area	ridge area	h'	reg. slope
run 3	0.057	0.031	0.082	0.050	0.021	0.164	0.060
run 2	0.079	0.148	0.067	0.044	0.066	0.130	0.088
run 1	0.066	0.072	0.094	0.036	0.061	0.129	0.048
run 5	0.055	0.041	0.050	0.020	0.022	0.087	0.016
run 4	0.068	0.086	0.108	0.023	0.050	0.165	0.059
run 6	0.059	0.066	0.102	0.013	0.042	0.084	0.074
run 7	0.117	0.269	0.142	0.030	0.038	0.228	0.032
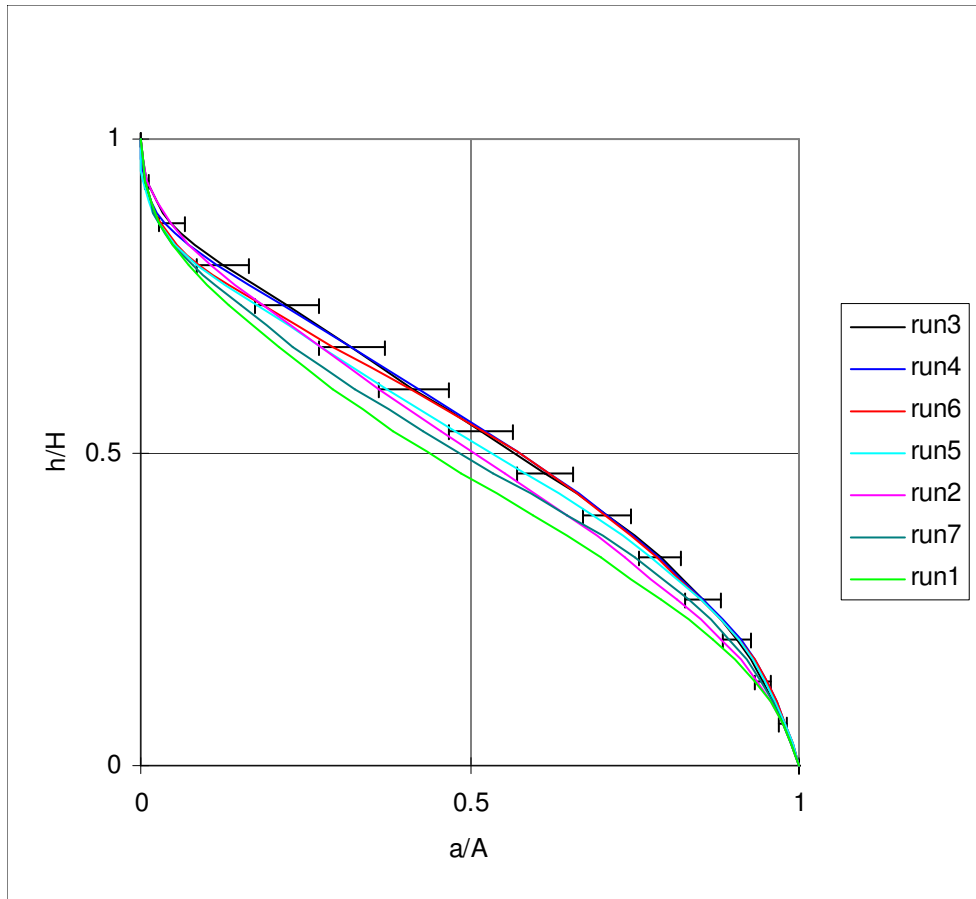
Figure 3-1. Hypsometric curves for experimental landforms. Each curve represents the run averaged distribution over each bin interval (15 bins) of elevation (elevation range is divided into 15 bins, and the number of points higher than the bin midpoint are counted, and normalized to the total number of points). The curves have been organized such that they follow the order in the legend (i.e., run 3 is the top curve, run 1 the bottom). Range within a given run is represented by the error bars for run 4. Error bars represent 1 standard deviation of a/A for each bin interval of h/H. Other runs exhibit similar variability in hypsometry, and depict a uniform mass distribution.
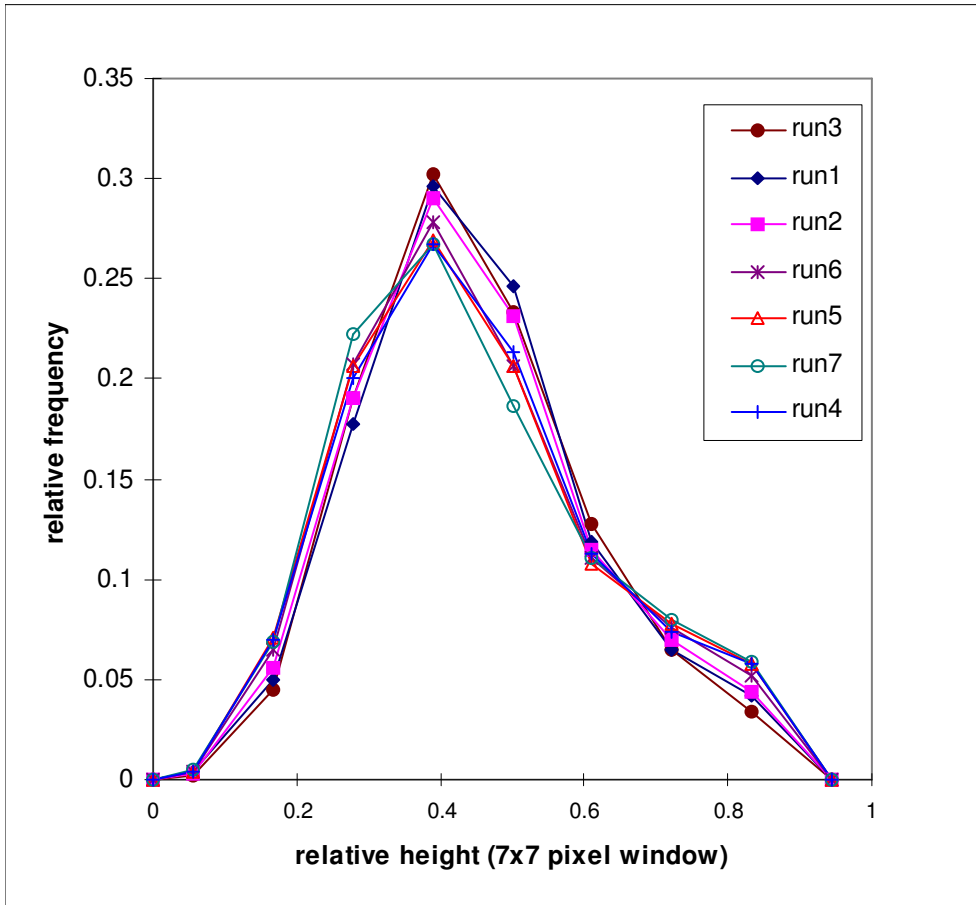
Figure 3-2. Relative height frequency distribution curves for experimental landforms. Experimental landform curves represent the run averaged distribution over each bin interval (15 bins) of relative height. The number of cells in a 7 x 7 pixel window lower than the center cell in the window are counted, and normalized to the total number of cells in the window. Values of relative height characterize the likelihood that a location is a ridge, valley, or hillslope. The within run variability is quite small, with a 4% variation (σ/μ) in the value for each bin interval. Note, the legend is ordered by peak height.
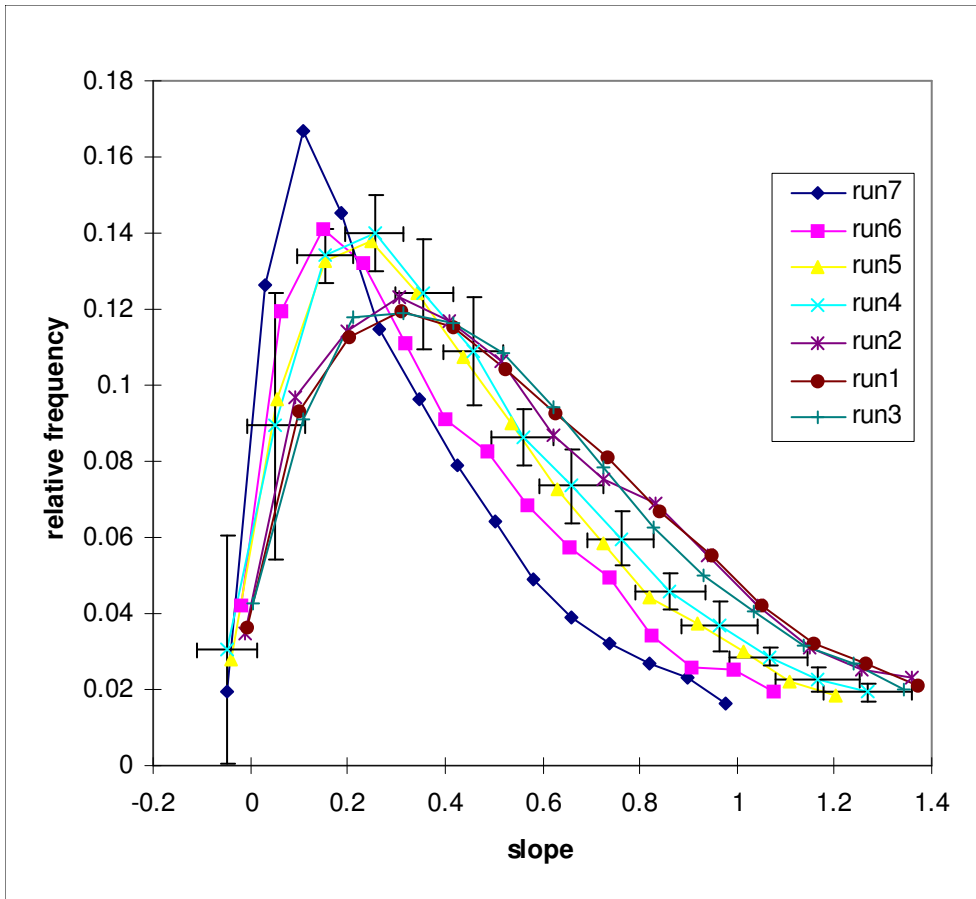
Figure 3-3. Steepest descent slope frequency distribution curves for experimental landforms. Each curve represents the run averaged distribution over each bin interval (15 bins) of slope. Error bars on run 4 represent one standard deviation ranges in bin midpoints and frequency (n = 9). Other runs exhibit similar variability in slope distributions. Note the stretching of the distribution that occurs for the ordering listed in the legend.
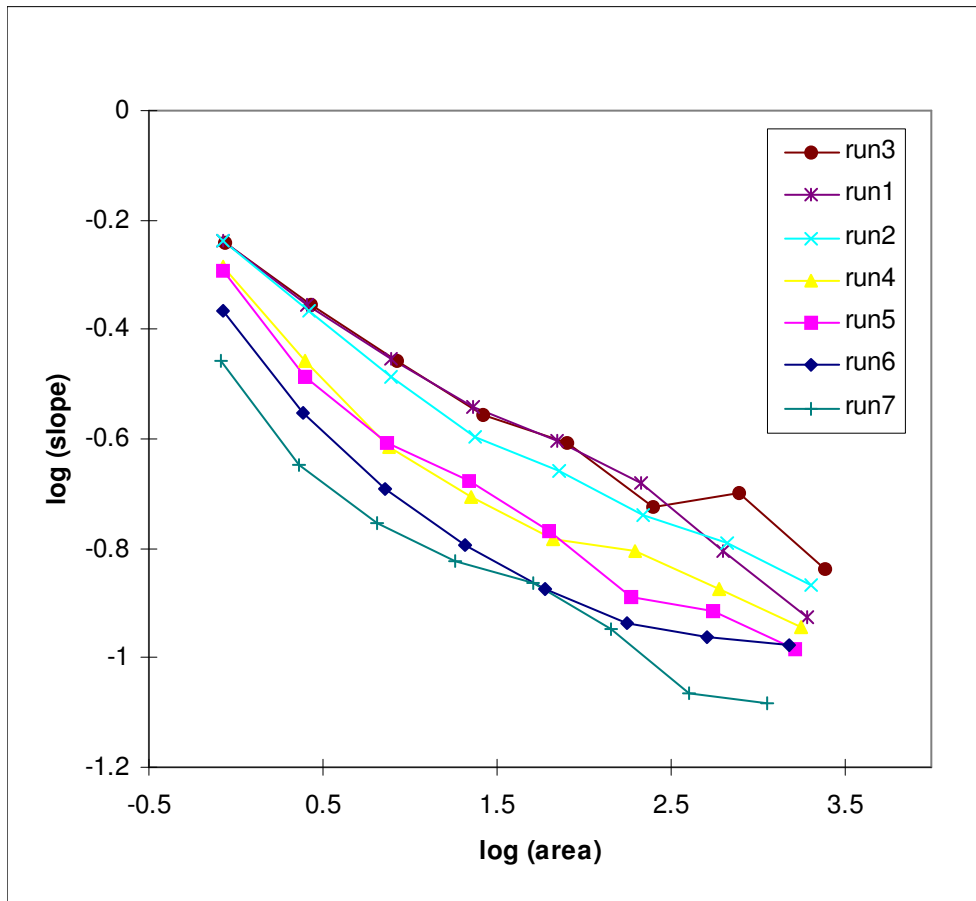
Figure 3-4. Area-slope curves for experimental landforms. Note, each plotted slope value represents a binned average (in log space) for the contributing area. Legend is organized from top curve (run 3) to bottom (run 7).
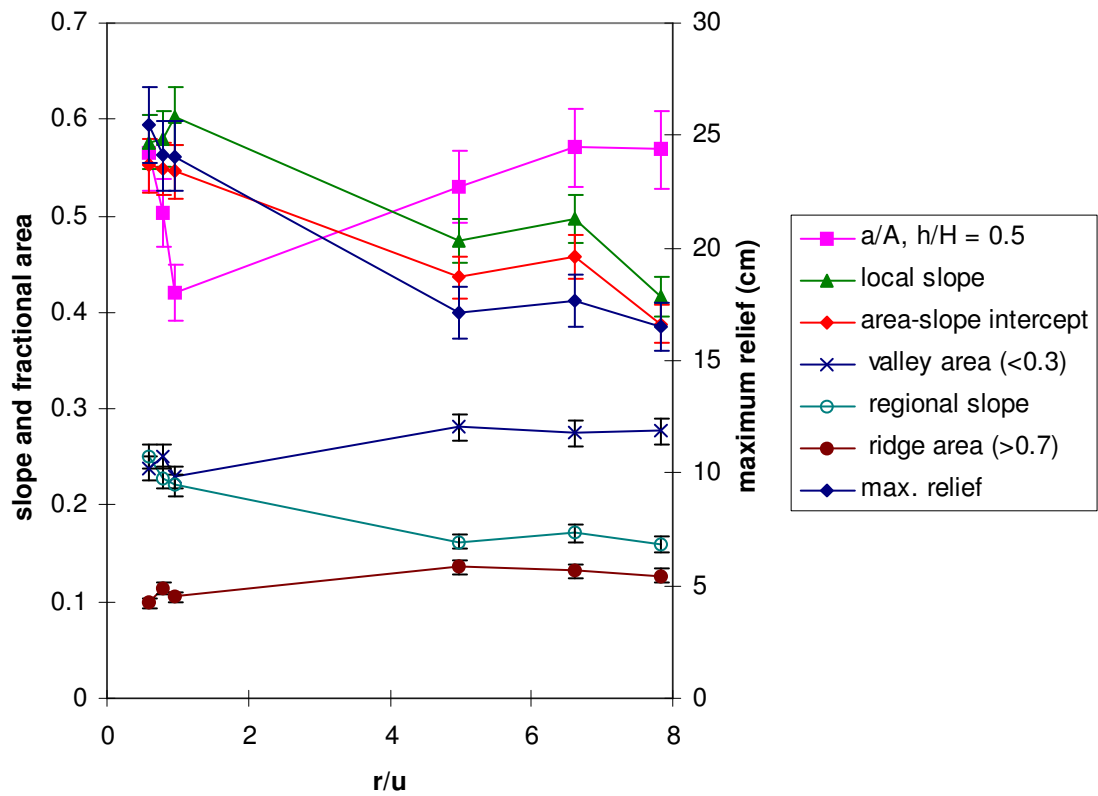
Figure 3-5. Summary topographic measures plotted against the water-to-rock ratio, *r/u*. Both slope and relief measures closely track each other. Hypsometry appears to capture information that is independent of both slope and relief, and exhibits a rather nonlinear response to forcing conditions. Error bars represent a range of one standard deviation for each of the measures (see Table 3-1 for the number of data sets for each measure). Both valley and ridge fractional area closely track each other, and in general increase as regional slope decreases.
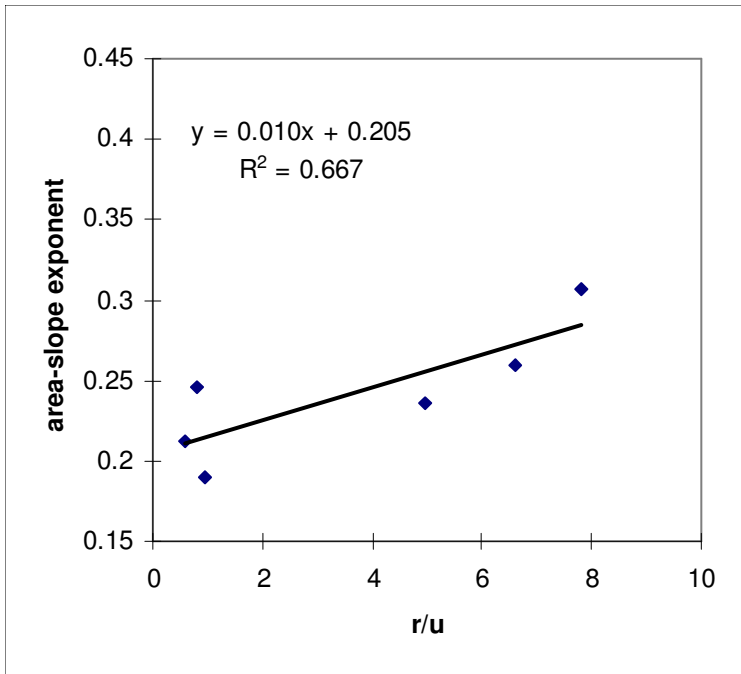
Figure 3-6. Area-slope exponent (θ) in the relation $S = kA^{-\theta}$, where S is slope magnitude, and A is contributing area (determined for $A < 50 \text{ cm}^2$), plotted against the forcing parameter, r/u. Theoretical considerations suggest θ should not depend on uplift or runoff rates. Here, values of θ vary between 0.19 and 0.3 for various runs, and show a weak relationship to the forcing parameter, r/u.
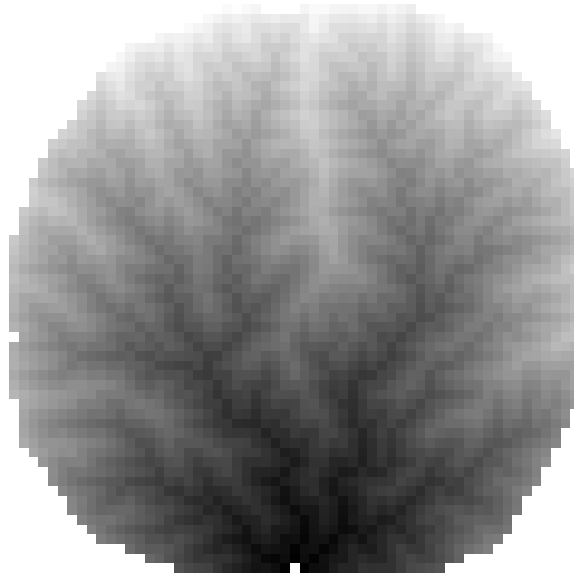
Figure 3-7. Numerical model elevation field at static steady state. Maximum relief is 14 cm. The numerical boundaries coincided with the physical experiment (width is 90 cm), grid spacing is 1.5 cm. Parameters in the erosion law[$\Delta z_{t+1} = \Delta z_t + \Delta t \, (U - K_1 \, Q^m \, S^n + K_2 \, S)$]are $K_1 = 0.001$, $m = 0.25$, $n = 1$, $K_2 = 0$, $\Delta t = 50$ s, uplift rate (U) = 0.0001, and rainfall rate = 0.001 (maximum discharge at the outlet = 6.6 cm^3/s). Units of uplift and rainfall are in mm/s, and roughly correspond to rates observed in physical experiments.
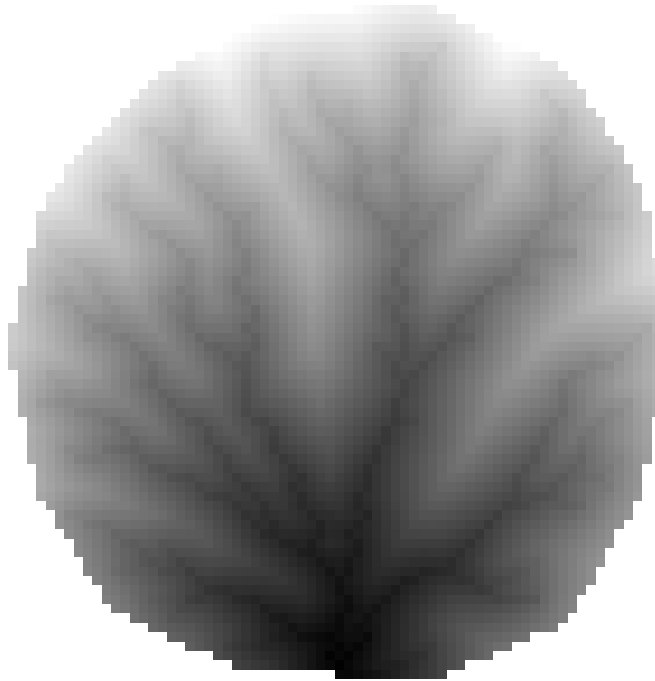
Figure 3-8. Numerical model elevation field with diffusive mass transport at static steady state, after 1.6 H_r (22 cm) units of eroded relief, measured from complete dissection. Width of image is 89 cm (1.1 L). Grid resolution is 1.25 cm spacing. Range in elevation for is 14 cm (14 cm = 0.17 L = 1 H_r). Input parameters to the numerical model [$\Delta z_{t+1} = \Delta z_t + \Delta t\ (U - K_1\ Q^m\ S^n + K_2\ S)$]are $K_1 = 0.001$, $m = 0.25$, $n = 1$, $K_2 = 0.1$, $\Delta t = 50$ s, uplift rate (U) = 0.0001, and rainfall rate = 0.001 (maximum discharge at the outlet = 6.7 cm³/s). Units of uplift and rainfall are in mm/s. These input parameters are of the same order of magnitude as the physical experiments. Relief is higher in this run, compared to the landform in Fig. 3-7.
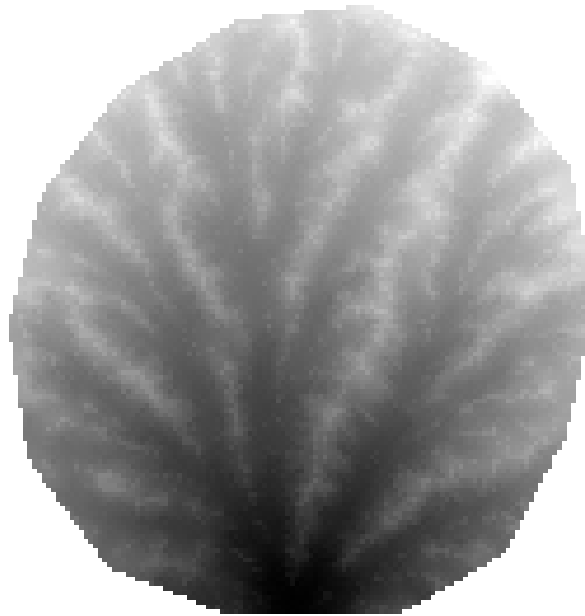
Figure 3-9. Example gray scale elevation map from erosion facility (from run 4). Width of image is 87 cm. Grid spacing is 0.7 cm.
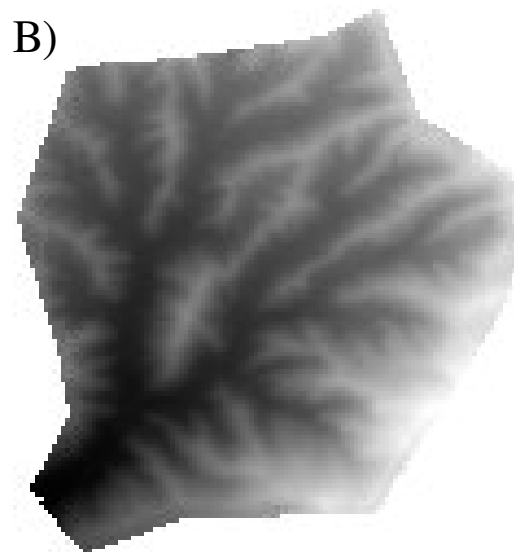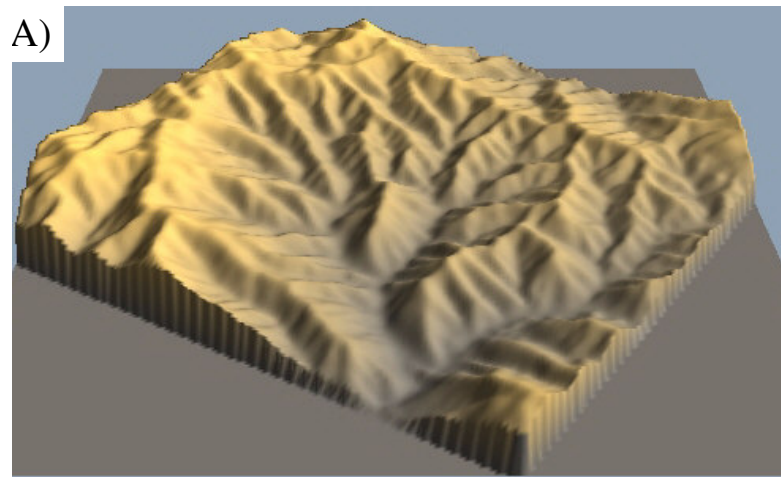
Figure 3-10. Mountainous drainage basin in the Sierra Madre Mountains of southern California, referenced herein as Madulce Peak. A) Perspective view of drainage basin, developed from USGS 7.5 minute DEM (Madulce Peak, northeast quarter of the quadrangle). B) Drainage basin of interest was extracted and plotted as a gray scale elevation map. Grid spacing is 30 m, relief is 553 m, and there are 10,251 data points in the basin (area = 9,225,900 m^2; L = 3037; H = 553 / 3037 = 0.18 L).
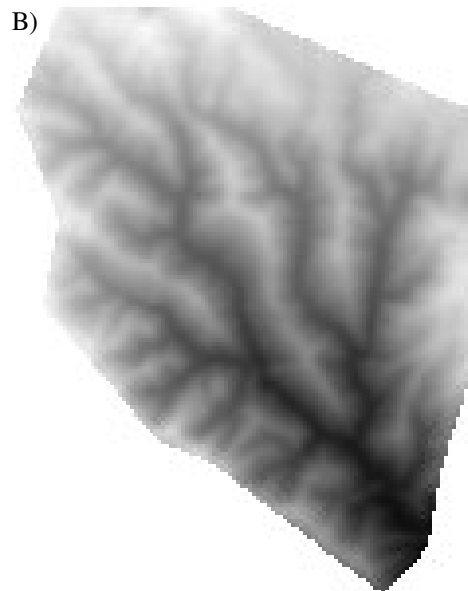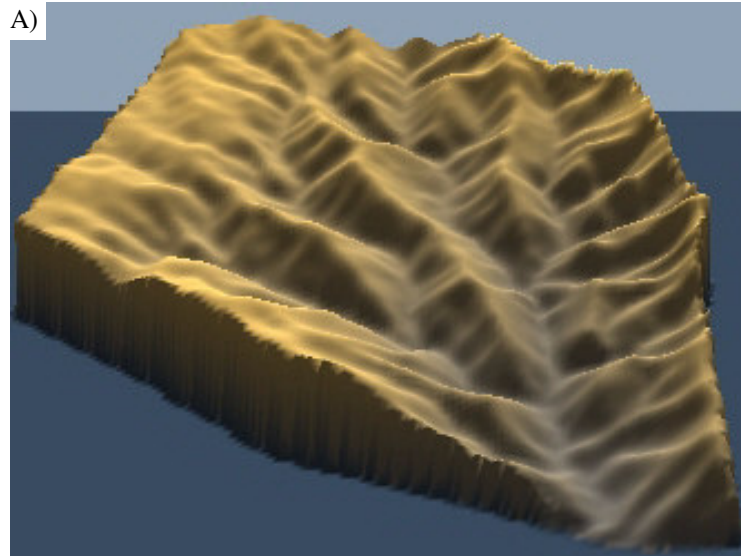
Figure 3-11. Mountainous drainage basin in the Sierra Madre Mountains of southern California, referenced herein as Cuyama Peak. A) Perspective view of drainage basin, developed from USGS 7.5 minute DEM (Cuyama Peak and Reyes Peak quadrangles). B) Drainage basin of interest was extracted and plotted as a gray scale elevation map. Grid spacing is 30 m, relief is 486 m, and there are 12,204 data points in the basin (area = 10,983,600 m^2; L = 3314; H = 486 / 3314 = 0.15 L).
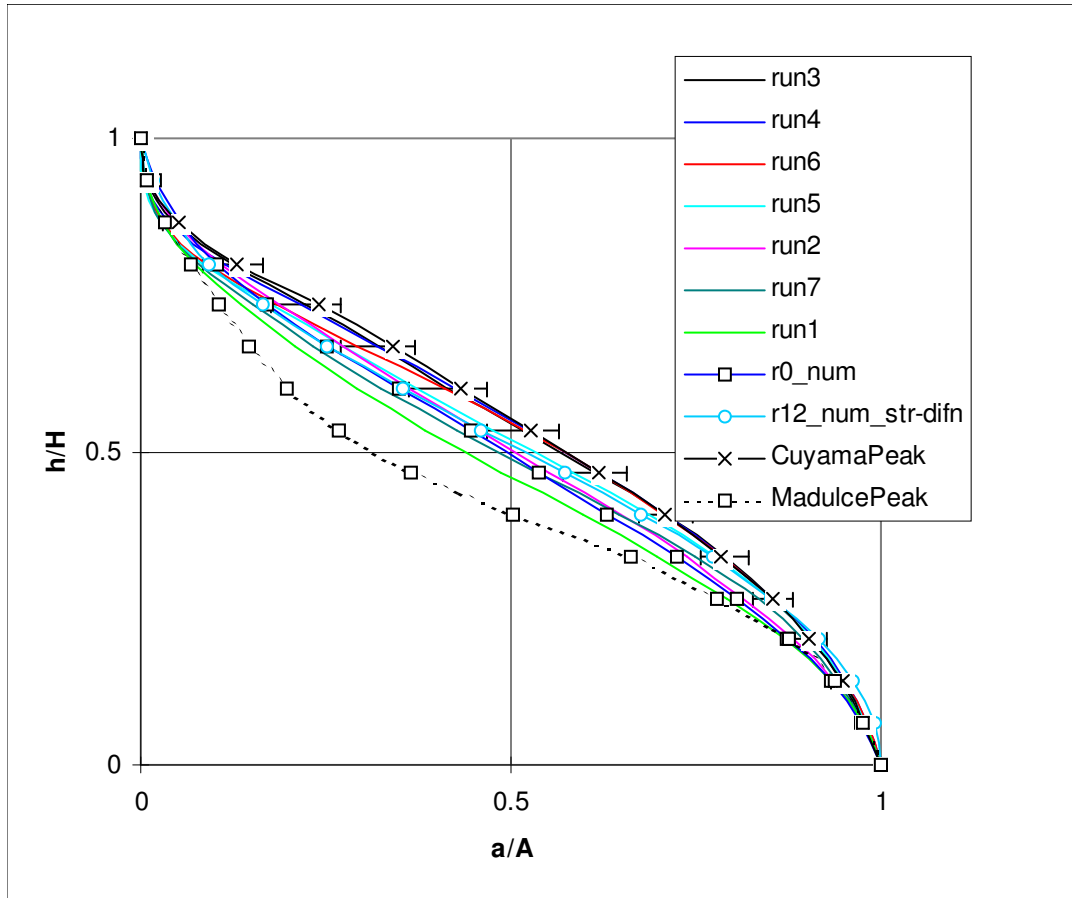
Figure 3-12. Hypsometry (area-altitude) for model and natural drainages. Numerical model has the same dimensions and outlet location as the physical experiment. The numerical landform (r0_num and r12_num_str-difn) mass distributions closely resemble the experimental data. The natural drainage basins essentially define the range for hypsometric curves. There is a greater range in hypsometry between these natural basins than in all of the experimental landforms, which fall somewhere between the two natural drainage distributions.
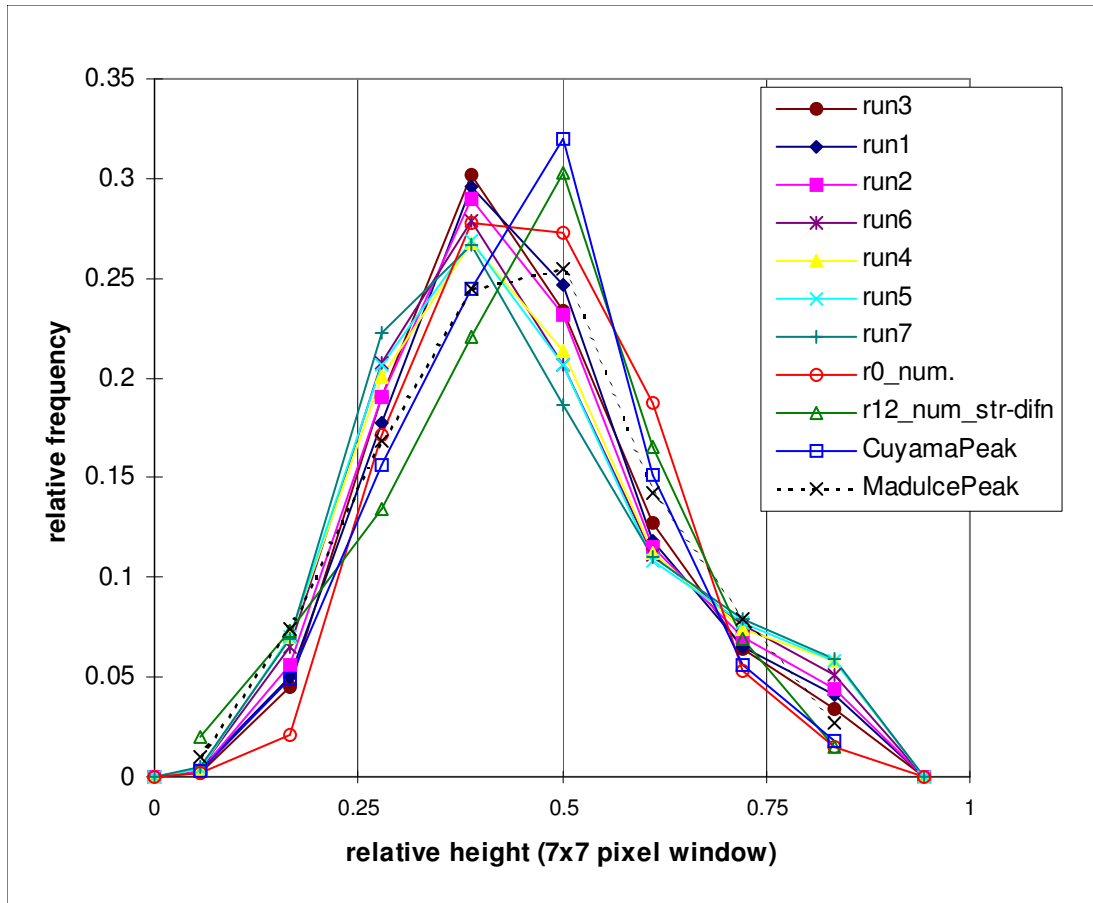
Figure 3-13. Local relative height distributions for model landforms and natural drainage basins. Numerical model has the same dimensions and outlet location as the physical experiment. The numerical landform local relative height distributions (r0_num and r12_num_str-difn) more closely resemble the natural drainage basins. The peak in the distribution is clearly shifted to lower values for physical experiments, suggesting a slightly different structure to the surface overall. Whereas the average point in the physical experiment is a valley, (more highs surround the point), the average point in the numerical and natural basins is positioned with equal numbers of higher and lower points as neighbors, that is, a hillslope.
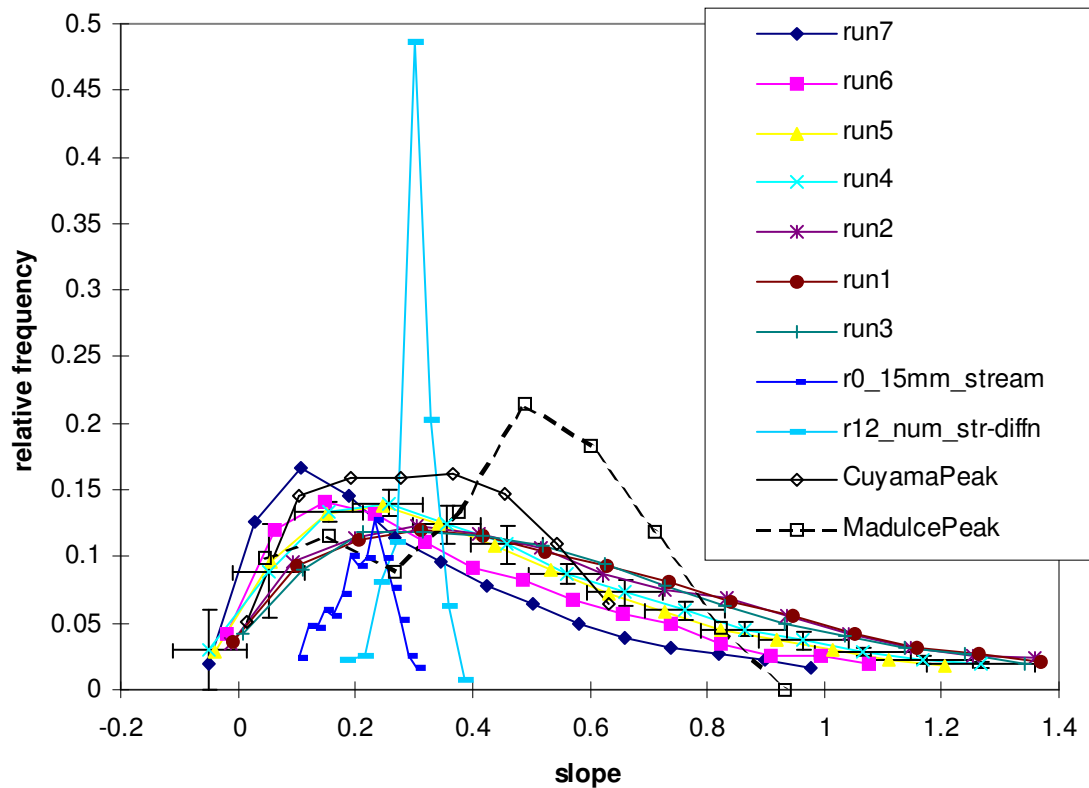
Figure 3-14. Slope distributions for model landforms and natural drainage basins. Numerical model has the same dimensions and outlet location as the physical experiment. The numerical landform slope distributions does not resemble any of the other basins. The range in slope is much narrower, and appears to be more normally distributed (the long tail at larger slope values is absent). Madulce Peak exhibits a similar slope distribution to the physical experiments, and Cuyama Peak shows a higher mean slope, with a longer tail for lower slope values.
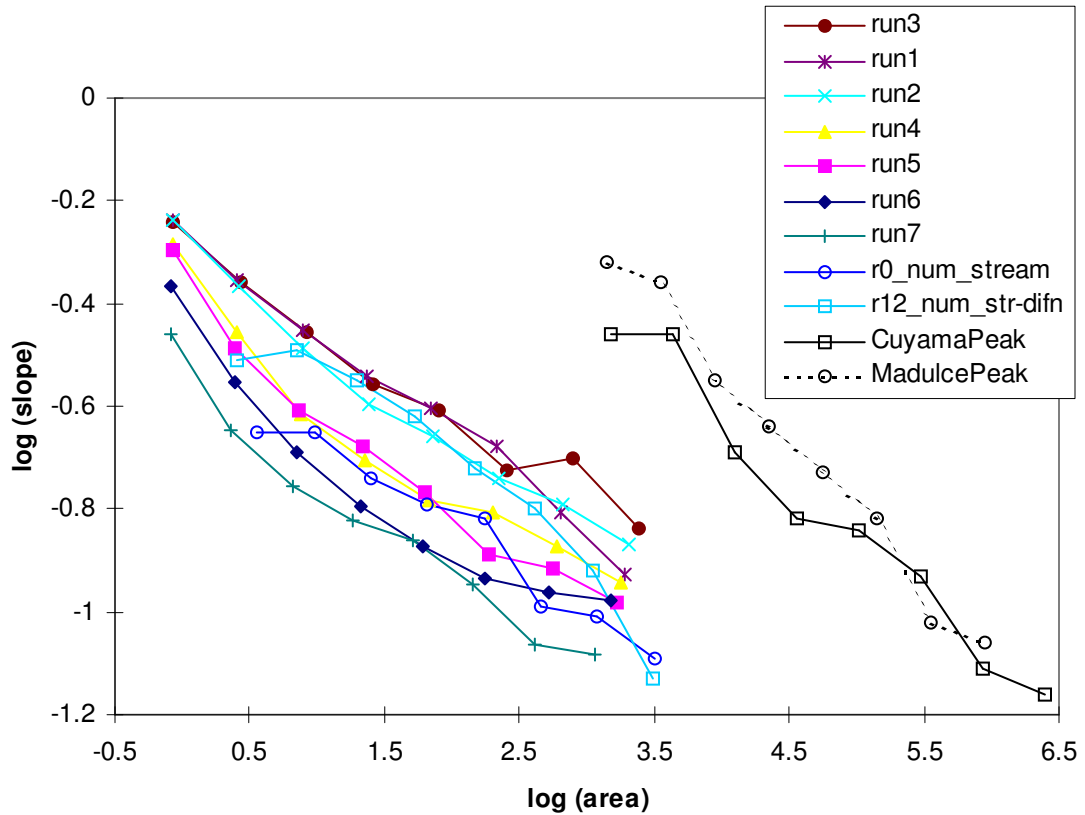
Figure 3-15. Area-slope relations for model landforms and natural drainage basins. Numerical model has the same dimensions and outlet location as the physical experiment. The numerical landform area-slope relation plots well within the experimental data (most closely resembles runs 4 through 6), but does not exhibit steep slopes at the smallest drainage areas. The strong diffusion model exhibits higher slopes. Both natural drainage basins have similar trends, with lower slope value for large area than most of the model runs. They also show a decrease in slope at the smallest scales, suggesting a lower limit to dissection by runoff.

Chapter 4
Landscape Instability Under Steady Forcing

Introduction

   The goal of constructing an erosion facility was to test the idea that eroding drainage basins develop fixed ridge and valley locations at steady state conditions, where erosion rate everywhere balances uplift rate. Several methods provide ways of testing this idea, and they include sketching ridge locations on time series photographs, computing erosion rates by differencing gridded elevation data sets, and computing changes in flow directions. Each of these methods returns a binary outcome: either the landscape structure is changing, or it is eroding uniformly. The first method is outlined in the attached paper titled "*Landscape instability in an experimental drainage basin*" (Hasbargen and Paola, 2000; Appendix A), and documents significant movement of ridge locations for an experimental run (run 2). Computing erosion rates and flow direction changes is addressed in the attached paper "*How predictable is local erosion rate in eroding drainage basins?*" (Hasbargen and Paola, 2003; Appendix B). In this paper, which addresses the problem of prediction in eroding landscapes, erosion rate variability and flow direction changes are mapped against time scale of observation. In short, while erosion rate variability increases rapidly at the shortest time scales of observation, flow direction change approaches nil. This curious observation implies that at short times, landscapes alter their structure in small increments, such that we can easily recognize features at some time t_i and at some later (though short) time t_{i+1} as being the same. While abrupt changes, such as stream capture, have been observed in natural drainage basins, they are rare in physical experiments. Over longer times, drainage basins become much harder to recognize, as ridges grow, migrate, and are annihilated. Methods and results from the two papers noted above are briefly summarized below.

   The next chapter (Chapter 5) addresses the observation that erosion rates in experimental data sets often exhibit localized spatial *patterns* that coincide with migrating divides. This observation implies they are linked in some way. Is it possible that migrating divides enforce spatial organization of erosion rates? This final section of

133

Chapter 4 analyzes possible feedback relations between divide migration and erosion rate variability via upstream area capture of a migrating ridge crest.

Ridge Sketches

Ridge crests were sketched on digitized photographs for eight sequential times after complete dissection for run 2. Ridge crests were chosen because they should be the most stable feature in a landscape, and because they are easier to identify in photographs than streams. Coordinates of all ridge crests were digitized. An example of ridge locations at time one and at some later time appears in Fig. 4-1 (p. 139). Drainage divides have reorganized in the right hand side of the basin. The large divide in the center left of the basin has migrated while more or less retaining shape. Other ridges have extended or shortened.

Ridge coordinates from all 8 photographs were then read into a grid at 1 cm spacing. The number of times that a cell contained a ridge location was recorded for each cell, and the resulting sum normalized to the number of data sets. This value was then plotted as a gray scale bitmap (Fig. 4-2, p. 140). No location was occupied continuously by a ridge over the span of the record (~3 H_r). The most frequently occupied locations were occupied in only 6 of the 8 photographs.

As a simple first order test of stability, the experimental drainage basin demonstrates surprising levels of activity and change. Ridges migrate, extend, shorten, and can be annihilated, with subsequent and fundamental changes to the drainage basin structure.

Spatial Erosion Rates Over Time

Spatially uniform erosion rates are a hallmark of the stable steady state landscape model. Hence, erosion rates provide another direct test for landscape models. The local erosion rate is computed by differencing gridded elevation data sets on a cell by cell basis, and dividing by the time separation between the data sets. The result is a spatial pattern of erosion rates between the two data sets (Fig. 4-3, p. 141).

As a very simple quantification of erosion rate variability, this operation was performed on all possible pairs of gridded data sets for each run. Note, the data sets used represent times of steady state conditions. The results can be summarized by recording

the mean (μ) and standard deviation (σ) of erosion rates for each grid pair, and plotting the coefficient of variation (σ/μ) against the time interval between the grids (Fig. 4-4, p. 142). Note, time has been transformed into fractions of unit eroded relief between the grids. Fractional eroded relief was computed by multiplying the time separation between grids by the long term uplift rate (to obtain the eroded distance between grids, h), and normalizing this length to the run's average maximum relief (H_r).

Clearly, variability decreases with the duration of time between grids. Static steady state landforms erode at a spatially uniform rate, so the coefficient of variation is nil at any time scale of observation. Even if a landscape is eroding nonuniformly, the method of computing variability against the time separation between grids will return low variability at long separation distances, because the average vertical distance between grids becomes large relative to the local relief. Erosional variability at short and intermediate time scales, however, offers a means of discriminating between uniform or nonuniform erosion.

Erosion rate variability (σ/μ) is of order 1 at the shortest documented time scales (erosion through ~0.05 H_r)*,* and decreases to 0.5 at intermediate to long time scales (0.5 H_r to 2 H_r). As Fig. 4-4 demonstrates, the decrease in variability with time can be modeled as a power law, and provides a measure of variability at any time over the measured range (0.1 to 3.5 H_r). It is worth noting that variability, when scaled to the fraction of eroded relief, is approximately the same for runs 1, 2, 4, 5, and 6, suggesting that variability is not sensitive to the forcing conditions, and hence, is not dependent on process activity due to changes in forcing rates.

Flow Direction Changes

Changes in local flow direction offer another measure of landscape activity. If the landscape is eroding uniformly, no changes in flow direction occur. Hence, flow direction change provides a simple yet powerful test of the *uniformly eroding drainage basin* hypothesis, and yields the following quantitative information:

1) a measure of dissimilarity (two elevation fields are *identical* if slope magnitudes and directions are the same, and *similar* if only the flow directions are similar);

2) a spatial map of flow direction changes;

3) a measure of activity (how many cells are changing flow direction);

4) an average rate of angular change; and

5) a measure of maximum dissimilarity, and the time scale required to reach maximum dissimilarity.

Flow directions were computed by determining the flow direction vector in the steepest descent direction on a cell by cell basis for each of two gridded data sets. Flow direction change was then computed on a cell by cell basis by taking the dot product of the flow direction vectors between two grids. The dot product (that is, $\cos(\alpha)$, where α is the angle between vectors) returns values between -1 (flow in opposite direction) and 1 (flow in the same direction). A spatial map of flow change can highlight migrating divides (Fig. 4-5, p. 143).

Summing the individual dot products, and dividing by the number of cells in the grid yields an average flow direction change. If a surface is eroding at a spatially uniform rate, we expect the relation to be a flat line with a flow direction change value of 1, i.e., no change in flow directions with time. If the landscape experiences variable spatial erosion, directional changes plot as a curve. The landscape becomes increasingly less recognizable with time as flow changes accumulate. Average flow direction changes are significant over longer times, and plot as a decay curve (Fig. 4-6, p. 144). Separation time between grids has again been converted into fractions of H_r. As erosion approaches nil, average flow direction change approaches unity, that is, no change. At longer times, the average flow change flattens to a constant value, and this value varies between runs (Fig. 4-7, p. 145). For separation times of ~1 H_r, the mean angular change is ~60 degrees (58 for run 2, 61 for run 4, and 63 for run 6). For separation times of ~0.1 H_r, average angular change is ~40 degrees ($\pm$ 2 degrees). The small differences in average angular change between runs is thought to be due to the roughness and drainage density variations between runs, implying some dependence on run conditions. Logarithmic trend lines with best fit parameters are presented next to each curve. These allow for estimates of flow change over the range of the fit. As such they are predictions for spatial activity in eroding landscapes at various observational time scales.

136

An accounting of the number of cells that have changes greater than a threshold angle, α, was also performed at all separation times. A diagram of fractional area of the basin with changes greater than a threshold angle is presented in Fig. 4-8 (p. 146). There is a rapid increase in the number of cells with flow changes with increasing separation between the grids. At the shortest time scale of observation (~0.05 H_r), over 40 % of the basin has experienced some flow direction change. Flow direction changes reach a clear limit at an eroded distance of ~1 H_r. Beyond this limit, the number of changes remains constant. At 1 H_r, ~65 % of the basin has experienced some angular change, and ~20 % of the cells have experienced flow switches > 44 degrees. The number of switches appears to be constant between runs with dissimilar run conditions, implying a lack of dependence on process activity, relief, slope, and drainage basin structure. This suggests that even at very long separation times the grids exhibit a moderate degree of similarity. In this case, a fixed outlet location dictates some level of similarity because flow must exit at fixed location.

Erosion Rates And Flow Changes In Numerical Model Output

Plots of erosional variability and flow path change were computed for the numerical grid above, and compared to data from a physical experiment (run 6). Steady state relief for the physical and numerical experiments is 16 and 14 cm, respectively, and forcing rates were comparable in both experiments, with r/u = 10 and 8.4 for numerical and physical experiments, respectively. Note, only the steady state portion of each run was used in the comparison. The physical experiment exhibits an order of magnitude greater variability in erosion rates (Fig. 4-8, p. 146), and substantially greater average flow direction changes (Fig. 4-9, p. 147). Clearly, the level of lateral activity is far greater in the physical experiment.

It must be noted that level of lateral changes as compared to numerical model output of landscape change are at odds. Even during a migratory ridge phase of evolution at steady state erosion conditions, the variability of numerical models is roughly an order of magnitude lower than physical experiments. This suggests that 1) landscape models may not capture the true variability in erosion rates, and 2) some feedback mechanism, or

destabilizing mechanism, may be missing from the numerical formulation and implementation. If one is concerned with predicting erosion rates across a landscape, and hence targeting areas where landscape form and process are likely to disrupt permanent human constructions, numerical models may underestimate variability, and hence the hazard to human constructs. Further work on feedback and variability in numerical model formulations must be conducted.

In summary, both local erosion rates and flow direction switches offer quantitative measures of nonuniform erosion. While a steady state relief and slope persist in the physical experiments, smaller scale features of the landscape appear to be somewhat mobile and transient. Significant fractions of the basin area undergo some change in flow direction. Flow changes accumulate at longer time scales of observation to alter the fundamental structure of the landscape, but even at the shortest time scales ($\sim 0.05\ H_r$), nearly 40% of the basin is experiencing some change in flow direction.
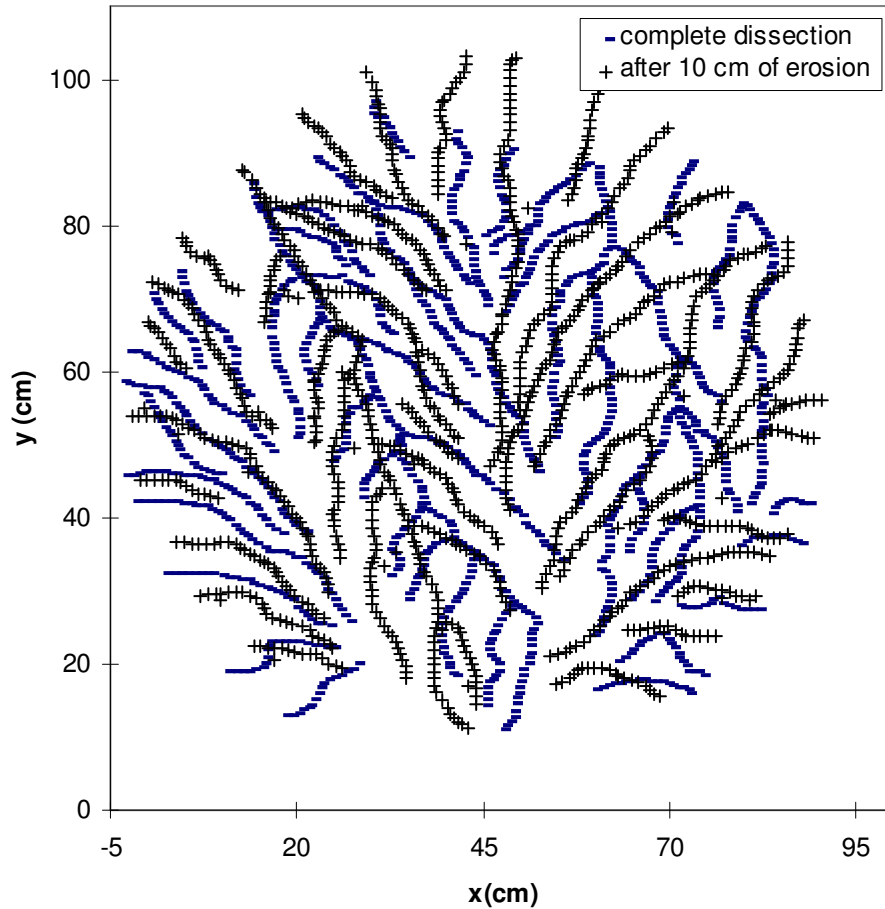
Figure 4-1. Ridge locations for two sequential photographs from run 2, after complete dissection. 10 cm of erosion occurred between the two times. Note the complete reordering of drainage divides in the right hand side of the basin, and the migration of the large divide in the left center.
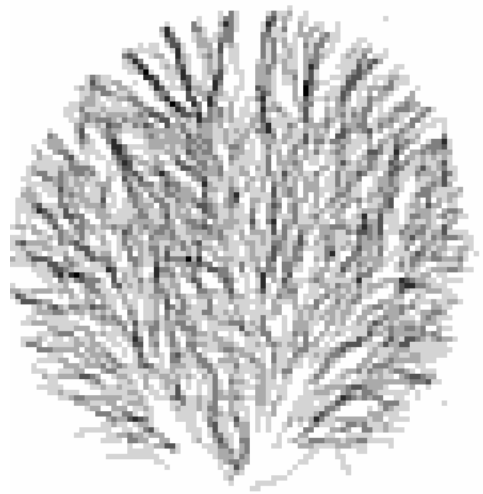
Figure 4-2. Plot of cell occupation by a ridge over a series of eight photographs for run 2. White indicates the cell has never been occupied, black indicates a cell has been occupied in all 8 photographs. No cells were occupied in all eight of the photographs (highest occupancy was 6 of 8). Eroded distance represented by the series is ~ 3 H_r. Few locations show persistent ridges, suggesting that ridge migration is a persistent feature of this run.

Figure 4-3. Spatial erosion rates plotted as a gray scale bitmap (8 grays), computed for grids from run 4 separated by 8 cm of erosion (~0.5 h/H_r). White indicates high erosion rates, and dark indicates low erosion rates. Average erosion rate is 0.59 µm/s (long term average from base level curve is 0.55 µm/s), with a one standard deviation (σ) of 0.19 µm/s ($\sigma/\mu \sim 0.33$).
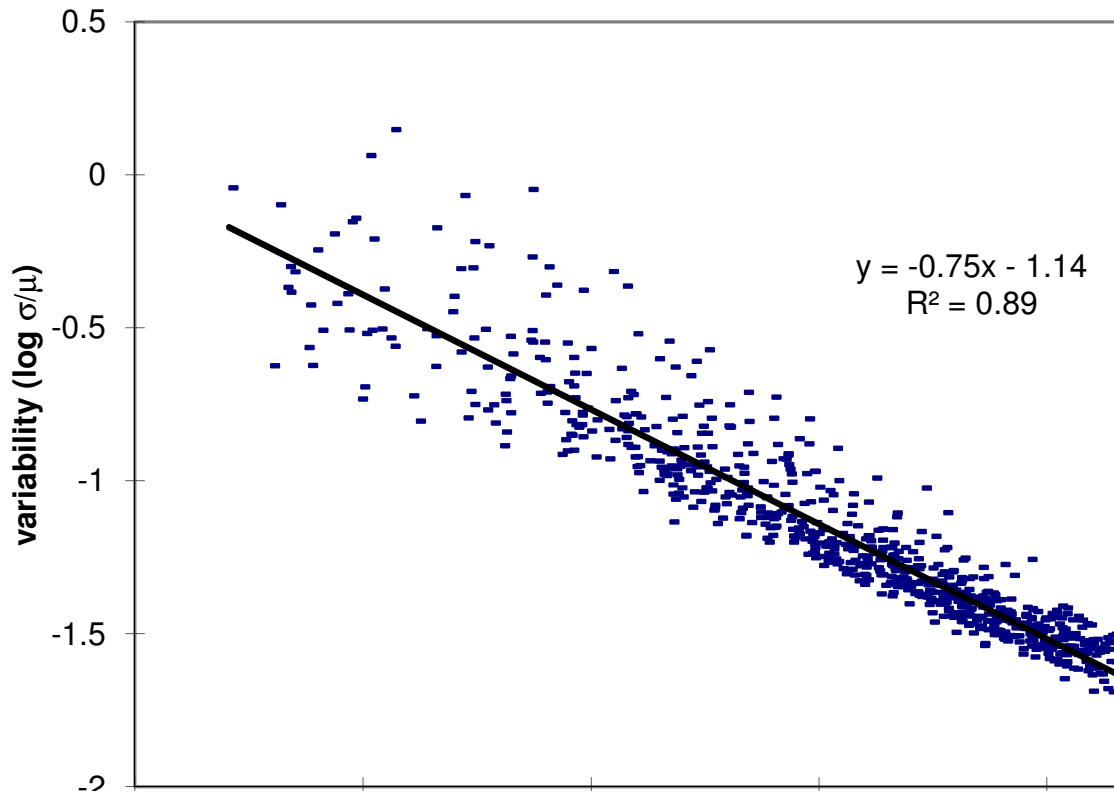
Figure 4-4. Erosion rate variability (σ/μ) plotted as function of separation distance between differenced grids. Data from run 1, 2, 4, 5, and 6. Runs 3 and 7 have been omitted. Run 3 was omitted due to the small number of data sets (3), and run 7 was omitted due to lack of steady state conditions. This chart documents the rapid increase in spatial erosion rate variability at shorter separation times between grids (note the data have been logarithmically transformed). At the shortest separation times, i.e., the time required to erode through 1/10 of the relief, erosion rate variability is of order 1.

Figure 4-5. Spatial map of flow direction changes that have occurred for the same pair used to compute erosion rate in Fig. 4-3. Note especially the dark areas, where flow has reversed. These locations delineate migrating divides. White indicates locations where flow remains unchanged. ~22% of the cells have experienced a flow change greater than *cos* α < 0.7 (45 degrees), and the average angular change (*cos* α) is 0.48 (61 degrees).
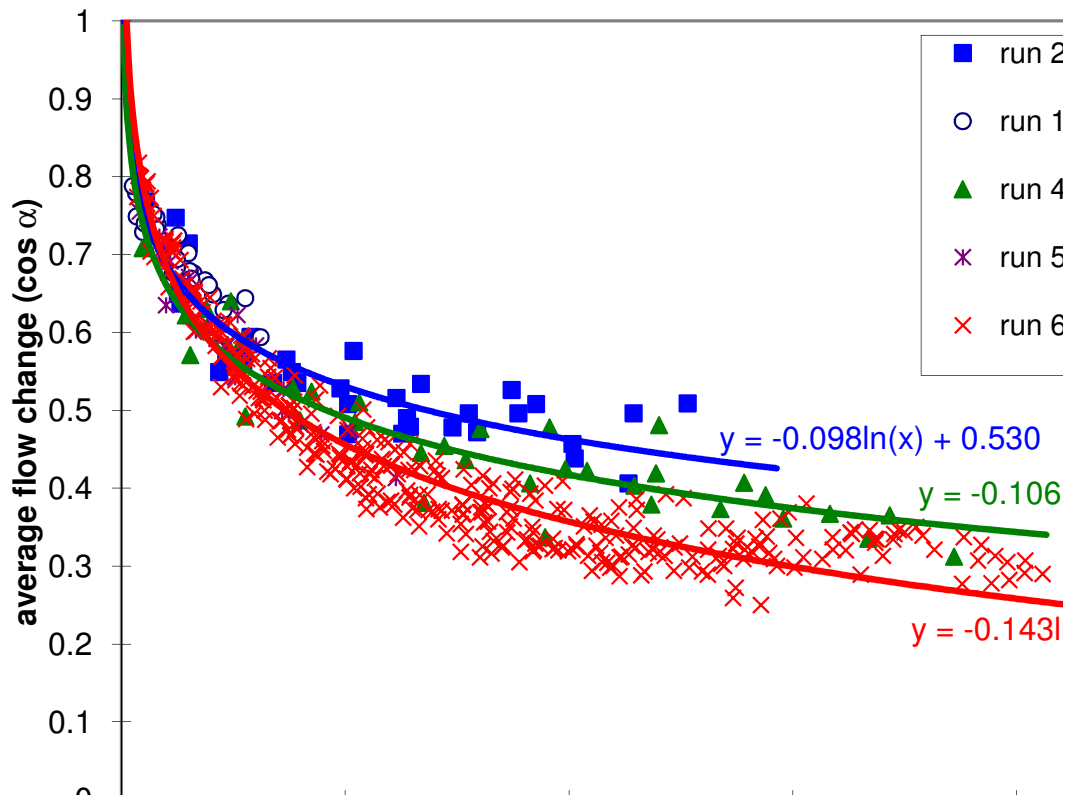
Figure 4-6. Average flow direction change for 5 runs at steady state conditions. Note the asymptotic approach toward unity for small units of erosion, and the rapid decrease in similarity with erosion. The flow paths appear to reach slightly different mean average change values at longer separation times. This may be due to the roughness and drainage density variations between runs. Logarithmic trend lines with best fit parameters are presented next to each curve. There is a general increase in the exponent with *r/u*, implying sensitivity to forcing rates.

144
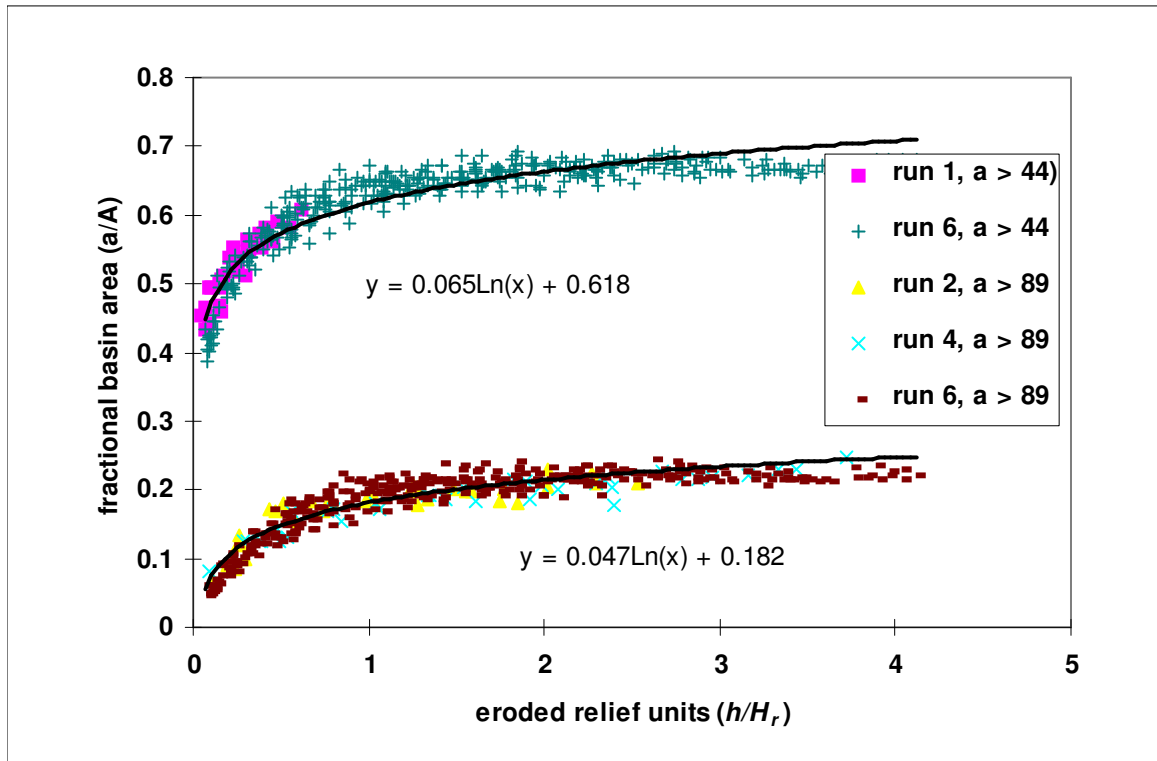
Figure 4-7. Area (fraction of total) involved in flow changes plotted against distance separation between grids. At 1 H_r, ~65 % of the basin has experienced some angular change, and ~20 % of the cells have experienced flow switches > 44 degrees. The number of switches appears to be constant between runs with dissimilar run conditions, implying a lack of dependence on process activity, relief, slope, and drainage basin structure. At the shortest time scale of observation (~0.05 H_r), over 40 % of the basin has experienced some flow direction change.
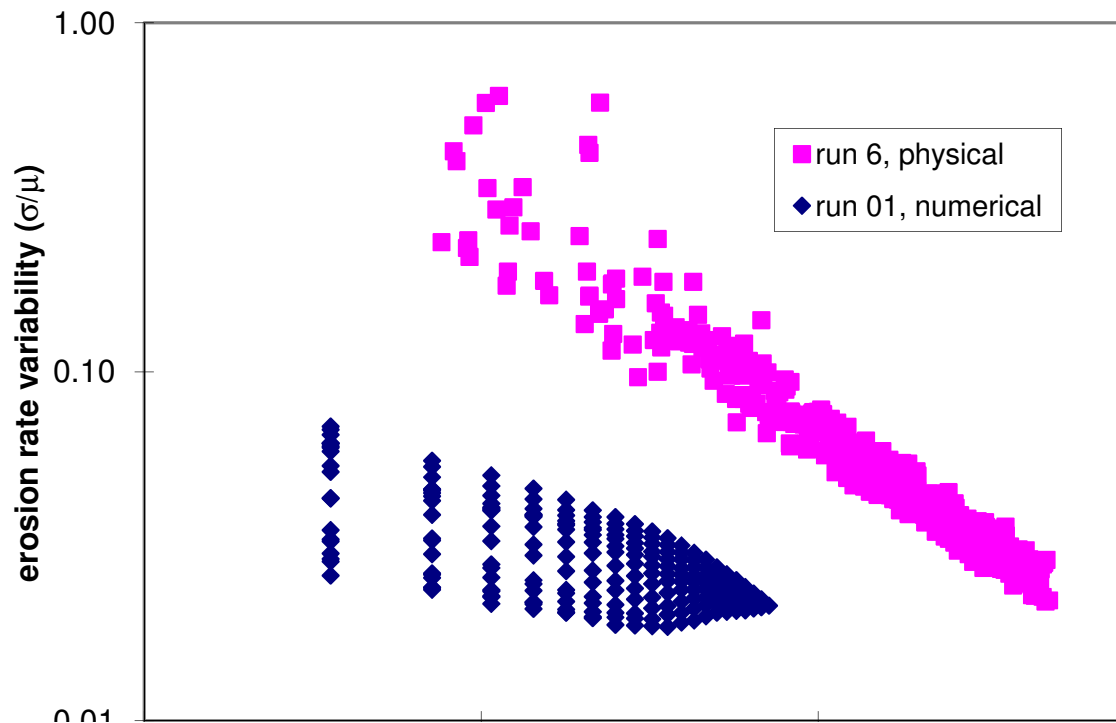
Figure 4-8. Steady state erosion rate variability plotted against eroded relief units for a numerical realization and physical experiment (run 6). Physical experiment exhibits roughly an order of magnitude greater variability than numerical realization. Numerical model has the same dimensions and outlet location as the physical experiment. Steady state relief for the numerical and physical experiments are 14 and 16 cm, respectively. Numerical model employed a stream power erosion law only, with *r/u* = 10. Physical experiment exhibited few hillslope failures, and is dominantly stream based erosion, with *r/u* = 8.4. Note the axes are in logarithmic space.
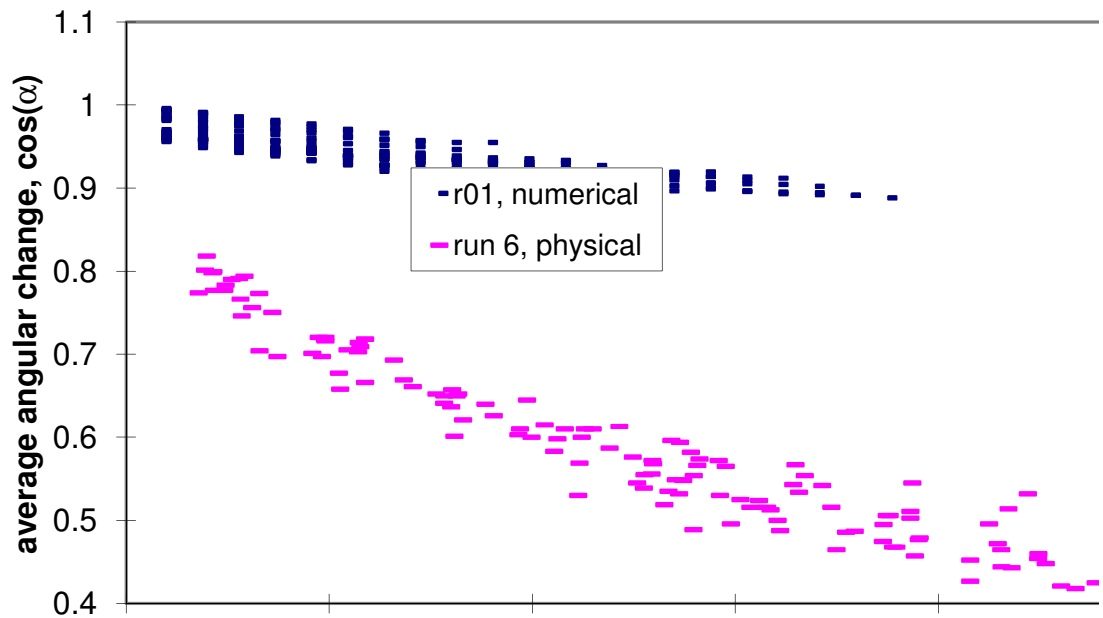
Figure 4-9. Average angular flow change plotted against eroded relief units for numerical (r01) and physical (run 6) model landforms. Physical experiment exhibits a far greater average flow direction change than the numerical realization. Numerical model has the same dimensions and outlet location as the physical experiment. Steady state relief for the numerical and physical experiments are 14 and 16 cm, respectively. Numerical model employed a stream power erosion law only, with $r/u = 10$. Physical experiment exhibited few hillslope failures, and is dominated by stream based erosion, with $r/u = 8.4$.

Chapter 5

Spatial Organization Of Erosion Rates And Divide Migration

Introduction

Experimental eroding drainage basins exhibit variable erosion rates under steady state conditions, where uplift is balanced by erosion. While a constant relief is maintained, the landscape itself continues to reconfigure itself over long time scales. What is driving this form of instability? In this chapter, a mechanism for destabilizing feedback is presented that could contribute to sustained landscape instability. I hypothesize that erosion rate variability and divide migration are entangled in a positive feedback, where divide migration captures runoff from a scavenged basin, decreasing runoff-driven erosion in the scavenged basin, and increasing runoff in the encroaching basin. Process interactions provide the initial variation in erosion rates required for divide migration. Once started, drainage area capture could impose spatial patterns of erosion rate on a drainage basin. Numerical and small scale experimental drainage basins demonstrate such interactions. Erosion rate variability driven by intrinsic process interactions may feed directly into larger scale, long term sustained divide migration.

How do natural landscapes erode over longer time scales? Field studies of erosion rates are accumulating in recent years, both for tectonically active and inactive landscapes. The possibility that erosion keeps pace with uplift has been demonstrated for several field studies (Adams, 1980; Reneau and Dietrich, 1991; Hovius et al., 1997; Meigs et al., 2002). For tectonically quiescent regions, such as the Appalachians, erosion rate studies have demonstrated both moderately uniform (Matmon et al., 2001; Matmon et al., 2003) and substantially variable erosion rates (Harbor, 1996). Further, application of a stream power erosion law to natural landscapes demonstrates that predicted erosion rates are rather variable (Montgomery and Brandon, 2002). The need for a conceptual framework in which to interpret spatial patterns of erosion rates exists. Indeed, theoretical models of stream incision and long term erosion offer a useful starting point for deducing dominant erosive processes at various scales within a drainage basin (Snyder et al., 2000; Lague et al., 2000), as well as offering a way of accessing possible changes in landscape

form to changes in climatic and tectonic forcing (Whipple and Tucker, 1999; Whipple, 2001; Stark and Stark, 2001). Significant insights into the response time of channel networks and hillslopes to changes in forcing have been obtained from these studies, which focus attention on how information is propagated through an eroding drainage basin, a critical issue for understanding dynamic behavior over intermediate to long time scales.

Stream incision is the dominant hypothesized mechanism for information transfer throughout a drainage basin. If knickpoints play a significant role in incision, and propagate as a kinematic wave upstream (Whipple and Tucker, 1999; Stark and Stark, 2001), one might imagine that increased erosion rates would follow in their wake, as hillslopes respond to lowering base level. Downcutting streams could destabilize hillslopes and force slope failures as a knickpoint passes through an area. Hence, local areas in the landscape would experience rapid short term fluctuations in erosion rate, but after the wave has passed through the system, such fluctuations might average to a uniform spatial distribution of erosion rates. A uniform thickness would be removed from the landscape. In this scenario, the entire landscape could maintain a stable form, that is, ridges and valleys maintain fixed spatial locations through time (Hack, 1960). Numerical landform evolution models based on shear stress or stream power erosion laws demonstrate exactly this behavior (Whipple and Tucker, 2001; Stark and Stark, 2001), when perturbed by changing the uplift rate. Stream networks would appear to be inherently stable structures. Stream profile inflections would serve to identify regions with enhanced erosion rates. Hence, under uniform lithologic conditions, a wave of incision might leave the main structure of the drainage basin unchanged over longer time scales, such as the time required for a knickpoint to propagate through the drainage network.

But what if the valley and ridge structure is only quasi-stable under steady state conditions? That is, what if short term erosion and transport processes interact in such a way as to generate emergent larger scale behavior in the drainage basin, such as divide migration? While self-organization of drainage basin structure has been shown for

149

numerical landscape models, intrinsic variability and larger scale behavior has not received much attention. This chapter addresses the issue of divide migration arising from intrinsic process interactions.

Overview of Controls on Divide Migration

Several factors are thought to control divide migration, first postulated by Gilbert (1877). He constructed a general theory of landscape sculpting based on surface runoff, rock resistance, and possible interactions between erosion, transport, and deposition. He detailed several mechanisms for lateral shifting of waterways:

1) Streams experience a broad distribution of storm events, which leads to non-uniform delivery of sediment to the channel. Aggradation can result: the channel floor increases in elevation until the banks no longer keep the stream in its course, and the stream migrates. This mechanism operates most effectively in areas of lower relief (corrasion surfaces) at the foot of mountains. He noted a type locality on the western side of the Henry Mountains, Utah, USA, where there were clearly abandoned channels on a low relief surface. He noted that streams cross inclined strata in this area without any deflection in stream profiles across lithologic contacts, suggesting that vertical incision was limited, and the streams expended most of their effort in eroding laterally. This scenario falls somewhat outside of our focus on steady state eroding drainage basins, where incision must occur.

2) Different rock types present varying degrees of resistance to stream erosion: streams will erode faster into softer material, especially where layered rocks are inclined. As a consequence of differential erodibility, he noted that hard strata tend to eliminate stream channels, and soft layers attract them. Again, drawing on the area surrounding the Henry Mountains, he documented regions of higher relief, with streams occupying softer sedimentary layers, and with more resistant rocks forming ridges. If the strata are inclined, he hypothesized that the stream will continue to erode the softer layers, essentially following the down dip direction of the softer strata. Clearly, rock resistance to weathering and erosion must play a significant role in the stability of ridge and valley locations. In this paper, however, we restrict our attention to instabilities related to

erosional process interactions, and the rest of this paper works within a framework of incision into a uniform lithologic substrate.

3) Gilbert also pointed out that abrupt changes in network structure occur during stream capture, where a headward incising tributary breaches a divide to an adjacent stream with a lower gradient, such as a perched or hanging valley. The incising tributary captures flow, and will downcut even more rapidly after the capture. The downstream portion of the captured stream would experience greatly decreased flow, and hence not erode as rapidly.

Numerous examples of stream capture in natural settings exist: Spain (Casas-Sainz and Cortes-Gracia, 2002; Mather et al., 2000); The Blue Ridge of the central Appalachians (Harbor, 1996); James River, Appalachians (Erickson and Harbor, 1998; Ries et al., 1998); Swiss and Western Alps (Frisch et al., 1998); Black Hills, USA (Zaprowski et al., 2001); and the northeast Basin and Range, USA (Harbor, 1997). For stream piracy to occur in an area of uniform lithology and climate, similar size streams must have unequal gradients. It would appear to be a mechanism that operates on landscapes exhibiting disequilibrium between adjacent sub-basins.

4) Gilbert also considered the possibility that divides will migrate so long as the hillslopes on either side of the divide are unequal. He assumed no difference in erosional processes on either side of the divide. If erosion rate is solely a function of slope and hillslopes have unequal slopes, then the divide crest will migrate in the direction of the hillslope with the lower slope. Smith and Bretherton (1972) considered the possibility of laterally migrating adjacent streams in a kinematic model, and demonstrate that if stream migration is governed by balancing sediment influx from adjacent hillslopes, then systems of streams are inherently unstable, that is, streams will migrate laterally over the time required to erode through the divide relief. They suggested that physical experiments incorporating stream and hillslope erosion could serve as a test for this hypothesis. Their kinematic assessment of migration has not received much attention.

Aside from Gilbert's thought experiments on perturbations to dynamic equilibrium (Gilbert, 1877), and Smith and Bretherton's perturbation analysis (1972), few systematic

151

studies (theoretical or otherwise) of drainage structure instability at steady state conditions exist. One reason for this oversight is that long term systematic behavior is largely inaccessible to us. We have been able to document various pieces of the erosional puzzle through process studies, but grappling with systematic interactions in eroding landscapes is inherently limited by the long times required to observe change. Physical experiments (Parker, 1977; Hancock, 1997; Hasbargen and Paola, 2000; Lague et al., 2002; Hasbargen and Paola, 2003) offer a means of observing long term evolution of drainage basins, and contribute additional insight into the dynamics of steady state landscapes. This field of research is experiencing renewed interest, largely because experimental landscapes offer control over forcing conditions, and time series observations. Detailed collection of the land surface elevations, while not trivial, has become commonplace, and data from physical experiments demonstrate that a dynamic equilibrium between uplift and erosion can readily be attained. Further, small scale experimental drainage basins exhibit spatial scaling properties that are similar to natural drainage basins (Lague et al, 2002).

Physical models of eroding drainage basins at steady forcing from climate and uplift, however, exhibit non-uniform erosion rates, even over longer time scales. Chapter 4 documents increased erosional variability at shorter observation time scales (see also, Hasbargen and Paola, 2003) and ridge migration over longer time scales (Hasbargen and Paola, 2000). This chapter investigates the relationship between spatially variable erosion rates and divide migration. The approach taken here is to acknowledge that lithologic, tectonic, and climatic variability must play a significant role in divide migration, especially in a landscape that is actively incising. However, the focus of this chapter is on divide migration driven by internal erosional dynamics in the absence of tectonic, lithologic, and climatic variability. In this chapter I hypothesize a positive (that is, destabilizing and self-perpetuating) feedback mechanism between erosion rate variability and divide migration that sustains long term drainage basin reconfiguration.

To facilitate comparison between numerical, experimental, and natural landscapes, we can define a horizontal length scale L and vertical length scale H_r in the following fashion:

$$L \sim A^{1/2} \qquad\qquad\qquad (5\text{-}1)$$

$$H_r = Z_{max} - Z_{min} \qquad\qquad\qquad (5\text{-}2)$$

where A is drainage basin area, Z_{max} is the maximum elevation in a drainage basin above datum, and Z_{min} is the minimum elevation above datum. Relief (H_r) typically scales as ~ 0.2 L for the data presented in this chapter.

Numerical Model Evolution

Interestingly enough, divide migration occurs within the simplest formulation of the erosion law (stream power based erosion law, no local diffusion) and in realizations involving local diffusion. Thus, a clue to divide migration falls out of these model runs. Migration and spatially correlated erosion rates are linked, ostensibly by feedback between upstream area capture and local erosion rate. Note, there is no other process operating in the numerical model except stream power driven erosion. In numerical formulations, migration is a transient effect that dies out over time as the landform achieves an optimal flow path arrangement that balances downstream flow accumulation and local slope between adjacent basins. In contrast, experimental landforms continually evolve, well beyond the time scale of stability for numerical simulations.

However, the phase of evolution of numerical models prior to a stationary planform state offers some insight into erosion rate patterns and divide migration. Figure 5-1 (p. 162) displays such adjustments graphically. In this simulation, a single long narrow valley flanked by higher ridges in the center of Figure 5-1 (A) 'closes' from the valley head downstream in subsequent images. The eroded distance between grids is 0.33 H_r.

Spatial erosion rates computed for the sequence in Figure 5-1 are displayed in Figure 5-2 (p. 163). Does valley closure yield a characteristic spatial pattern of erosion rates? Intuitively, a laterally migrating ridge should exhibit a linear trend of higher erosion rates that marches in the migration direction. However, the spatial pattern of erosion rate is somewhat more complex than intuition offers, in this case. The closure of the valley is

marked by higher erosion rates around the valley head and flanking ridges, and sharply decreased erosion rates in the valley. Valley closure is accompanied by lateral migration of the main divide. Figure 5-2 demonstrates that organized behavior is observable over the time required to erode through ~0.3 of the maximum relief of the landscape. Similar patterns have been observed for shorter time scales (0.1 H_r), but are not documented here.

A visual clue of imminent ridge migration in Figure 5-1 is the narrowness of the valley, and the lower elevation of adjacent valleys. A profile across the midsection of Figure 5-1 (A) demonstrates the perched nature of the narrow central valley (Fig. 5-3, p. 164). Differing local base level has been postulated as a prerequisite for stream capture. However, stream capture is not the only possible fate of perched valleys. A perched valley can be annihilated by encroachment of its divides, as the above example demonstrates. Drainage area is captured by the advancing divide, and the valley experiencing encroachment shrinks.

Behavior Of Steady State Physical Experiments

We have constructed a physical model, dominated by surface runoff erosion, that allows a drainage basin to erode through several relief distances at constant forcing from rainfall and uplift. We documented ridge migration (Hasbargen and Paola, 2000) and spatial and temporal variability of erosion rates (Hasbargen and Paola, 2002) in this facility for runs at a statistical steady state balance between erosion and uplift. Figure 5-4 (p. 165) shows an experimental landform long after the original flat surface has been completely dissected.

Long narrow valleys in Figure 5-4 are suggestive that ridge migration accompanied by valley closure is occurring. We extracted elevations from stereophotographs for this run, and developed gridded elevation models from them. We show a time series of elevation models (Fig. 5-5, p. 166) after the photograph of Figure 5-4 was taken. Indeed, the long narrow valley visible in center of Figure 5-5 (A) closes (black arrows), accompanied by downstream migration of a ridge triple junction at the valley head. Other valleys have also experienced closure, and some ridges have grown, while others have shortened. Ridge and valley migration in the absence of valley closure can also be identified in the images.

154

A ridge 'triple junction' at the top right of 5-5 (A) opens as a valley-ridge pair migrates down the right side of the main divide (white arrows). Hence, valley closure, valley opening, and lateral divide migration in the absence of valley annihilation are possible 'modes' of behavior over longer time scales.

Clearly, the valley closure and divide migration in the experimental landform are not that dissimilar from the numerical landscape of Figure 5-1. Note, however, that the experimental landscape exhibits far greater changes than the numerical model. Further, ridge migration is still occurring in experimental landscape long after ($> 2\ H_r$) a statistical balance between uplift and erosion has been reached. Apparently, a feedback mechanism that sustains migration in the erosion facility is missing from the numerical model. For this chapter, the differences between physical and numerical experiments are not a central theme. Of interest here are the geometric features in a landscape that offer clues and insight into longer term behavior of eroding landscapes. Indeed, the elevation profile across the center of the experimental landform (Figure 5-6, p. 167) shows a perched valley experiencing closure, remarkably similar to the numerical simulation.

Spatial erosion rates for the time series elevations in Figure 5-5 reveal a similar pattern to the numerical model, albeit with far spatial variability in erosion rates (Fig. 5-7, p. 168). The characteristic feature of *numerical* erosion patterns is the low erosion rates in the valley that is undergoing closure, with high rates on the flanking ridges. Although experimental landscape erosion patterns are somewhat more complex, spatially coherent patterns exist. Regions with very low or very high erosion rates mark the region of migrating features.

An additional means of tracking changes in the structure of the landscape is given by changes in flow direction. We computed steepest descent flow direction on a cell by cell basis for each of two grids presented above (Fig. 5-5, B-C). We then computed the angular change in flow direction in each cell, using the dot product between flow direction unit vectors. If two elevation fields are identical, their flow fields will be identical. Flow change values range from -1 (flow reversal), 0 (orthogonal flow change) to 1 (no change). We reported average flow direction change as a function of eroded

distance between grids elsewhere (Hasbargen and Paola, 2002; Appendix B). Essentially, average flow direction change increases when computed for longer separation times, suggesting increasing dissimilarity of flow paths over time. Here, we plot individual cellular values for flow change (Fig. 5-8, p. 169) as a gray scale map. Note that spatial patterns of flow change are quite visible, and visually correlate well with spatial patterns of erosion rate. Dark regions indicate locations where the flow field has reversed. These regions typically correspond to the migration of a ridge crest.

   To summarize, we have presented cases of lateral movement of ridges and valleys in physical and numerical landscape evolution models. Erosion rates exhibit some level of spatial correlation and structure around migrating divides. Perched valleys exhibit lower erosion rates, and hence, are encroached upon by adjacent sub-basins. This simple criterion could be used to identify locations in natural drainage basins that might be experiencing divide migration. Erosion rates, derived from cosmogenic nuclides, from sediment flux measurements, or perhaps low temperature exhumation rates based on U-He isotopic measurements, could serve as measures of divide migration over longer time scales.

Divide Migration And Erosion Rates: A Geometric Analysis

   How are erosion rates and divide migration related? Following Gilbert's lead, if erosion rate is simply a function of slope, then symmetric ridges indicate stability. If erosion rate is also sensitive to other factors, such as surface runoff and flow accumulation, lithologic variability, or biologic activity, then a stable criterion becomes more difficult to assess. We can, however, ignore physical processes for a moment, and develop a geometric model that describes the conditions necessary for a drainage divide to migrate. Figure 5-9 (p. 170) sketches a situation for differing erosion rates on each side of a ridge. If we assume that over an appropriate time and length scale that a uniform layer is eroded from a hillslope, then the change in ridge crest location Δx per unit time Δt is a function of hillslope angles α and β and erosion rates on each side of ridge, δz_α and δz_β.

   We develop a relation for ridge migration rate as follows.

$$\tan \alpha = (\dot{z}_\alpha \Delta t - \Delta z) / \Delta x \qquad (5\text{-}3)$$

$$\tan \beta = \Delta z / (x_\beta + \Delta x) \qquad (5\text{-}4)$$

Solving equations 1 and 2 for Δz:

$$\Delta z = \dot{z}_\alpha \Delta t - \Delta x \tan \alpha \qquad (5\text{-}5)$$

$$\Delta z = (x_\beta + \Delta x) \tan \beta \qquad (5\text{-}6)$$

Setting 3 and 4 equal to each other, using $\dot{z}_\beta \Delta t = x_\beta \tan \beta$, solving for Δx, and dividing by Δt yields

$$\Delta x/\Delta t = (\dot{z}_\alpha - \dot{z}_\beta) / (\tan \alpha + \tan \beta) \qquad (5\text{-}7)$$

Several significant implications result from equation (5-7). No migration occurs if erosion rates are either nil or equal. Uniformly eroding landscapes will exhibit temporally stationary divides, regardless of ridge asymmetry. It seems unlikely that asymmetric ridges would experience uniform erosion rates on each side of a divide, particularly if erosion rate is some function of slope. However, equation (5-7) is derived solely from geometrical considerations. Any processes that lead to nonuniform erosion rates will lead directly to divide migration. We consider now the effects of hillslope angles on migration rate in (5-7). As either of the slopes approaches vertical, the denominator approaches infinity, and migration is driven to nil. At the other extreme, as hillslope angles approach 0, the denominator becomes infinitely small, which implies that migration rate becomes infinitely large. It further suggests that divides with lower slope angles can migrate faster than divides with higher slopes. The effect of slope on migration rate leaves open the possibility that divide migration rates can exceed vertical erosion rates.

Are extreme slope conditions required for divide migration rate to be of the same order as erosion rate? Dividing relation (5) by erosion rate differences, assuming for simplicity's sake that hillslope angles are equal, and setting the result equal to unity yields the following:

$$\Delta x/\Delta t / (\dot{z}_\alpha - \dot{z}_\beta) = 1/ (2* \tan \alpha) = 1. \qquad (5\text{-}8)$$

Hence, $\tan (\alpha) = \frac{1}{2}$, or $\alpha \sim 26°$, a value for hillslope angle that is not unusually large or small for natural drainage basins. Thus, divide migration rates on the order of erosion rates are geometrically plausible for eroding drainage basins. Estimates of large scale

157

drainage divide migration at the margin of the Basin and Range are on the order of 1-2 m/kyr, easily on the order of incision rates in this area (Harbor, 1997).

Finally, is there enough vertical space for migration of divides to occur? That is, has erosion consumed a large depth of rock, perhaps on the order of a relief unit? Geobarometric data of rocks in mountainous natural settings demonstrate that exhumed depths of 10-20 km are not uncommon. Relief in many mountain ranges is on the order of 1-5 km. Hence roughly 2 to 10 relief distances (exhumation depth/relief) have passed through the topographic surface. If ridge migration rates can be on the order of erosion rates, then topography can be highly mobile when viewed over this time scale.

The divide migration relation (5-7) can be used to assess erosion rate variability if divide migration rates and hillslope angles are known. The relation can also be coupled with an erosion rate law, and yield predictions for migration rates of drainage divides in natural landscapes.

Observations Of Small Scale Process Interactions In Physical Experiments

As noted earlier, numerical simulations experience divide migration, but such adjustments inevitably lead to a more stable configuration. Self-sustaining instability is not present. In physical erosion experiments, such is not the case. Persistent changes in the drainage structure can occur long after steady state conditions hold. If migration of itself is not capable of self-sustaining behavior, what is driving the physical landscape migration? Small scale local variability in erosion rate could be the answer. Episodes of valley widening and temporary sediment storage, followed by knickpoint generation and excavation of the stored sediment are common at short and intermediate time scales (Fig. 5-10, p. 171). Aggradation in valley floors may result from streams that are near or at capacity, and are unable to transport excess sediment supplied to the channel by a hillslope failure. Deposition ensues. Because uplift is continuous, however, the system must incise. Typically, as a stream incises, the channel narrows and deepens, and the incision occupies a small part of the valley width. There is no mechanism for the rest of the valley to keep pace with incision, due to small area and runoff, and low slope conditions. A terrace can result. Valley aggradation and re-excavation occurs over a wide

range in forcing conditions from uplift and rainfall in physical experiments. Episodic aggradation and incision does not appear to be restricted to unique forcing conditions. Other physical experiments of drainage basin erosion have developed similar behavior (Parker, 1977; Hancock, 1998), when a step base level drop was imposed on the system. After the initial disturbance propagated through the drainage basin, hillslope failures increased, causing local aggradation and re-incision. Further, while such behavior can easily be forced by changing rainfall or baselevel fall rates, they also develop under uniform forcing conditions. Hence, this behavior can arise from intrinsic process interactions—the hallmark of autocyclic behavior.

Discussion

Thus far we have presented evidence for longer term divide migration and shorter term process interactions that can lead to nonuniform erosion in numerical and physical steady state drainage basins. The question arises, is the dynamism exhibited by small scale physical experiments a scale defect? Clearly, small physical experiments can not be dynamically scaled to natural settings. Flow conditions in our model streams indicate that flow is predominantly laminar (maximum Reynolds number of ~500 for various runs). Surface tension effects are clearly visible at very small scales (areas < 1 cm^2) as meniscus at the edge of streams, and as pendant water drops on hillslopes. It is difficult to imagine how these effects are responsible for larger scale process interactions, such as temporary deposition and incision in valleys. Our physical model is clearly a simplified version of natural drainage basins, in that biologic and chemical weathering effects are absent, and forcing is continuously applied. While it is speculative to extrapolate dynamics based on small scale experimental drainage basins, the similarity of form and process between experimental and natural drainage basins is suggestive that such dynamics could occur in larger, natural drainage basins.

Strath and depositional terraces in natural landscapes have often been interpreted as features that develop due to *changes* in climate or tectonic forcing conditions. In our physical experiments, we observe features which strongly resemble terraces that develop during knickpoint migration. Episodic incision was also noted in other physical drainage

159

basin models (Parker, 1977; Hancock, 1997) following a single pulsed base level fall. Terrace formation, stream piracy, and divide migration have been well-documented for natural drainage basins. The development of terraces can be explained by invoking changes in sediment supply, runoff conditions, or tectonic forcing. But these may not be the only means of generating terraces. Our experiments were continuously forced, and spontaneous knickpoint generation occurred within episodic cycles of temporary sediment storage in valleys and subsequent re-incision. Apparently, changes in external forcing conditions are not requirements for terrace formation. Deposition is clearly a means of generating nonuniform erosion rates across a landscape. Knickpoint migration is another. Hillslope failures could trigger local deposition, particularly for streams at or near transport capacity, and generate such epicycles in eroding drainage basins. These interactions are clearly strong enough in physical experiments to sustain persistent variability in erosion rates, which turns on the positive feedback cycle between divide migration and spatially organized erosion rates.

The hypothesized relationship between erosion rate variability and divide migration has interesting implications for the behavior of eroding landscapes. An optimal network structure (Rinaldo et al, 1992) would imply that a stable configuration of valleys and ridges is the ultimate fate for eroding landscapes. Perturbations to the system, either random or propagating, such as knickpoints, cause adjustments that lead to a more stable configuration. Numerical models certainly exhibit such negative, stabilizing feedback. Optimality, however, might be obscured by positive feedback between divide migration and runoff capture.

Spatially correlated erosion rates offer several avenues for further research in natural landscapes. Air and space born sensing of the landscape is in a rapid growth phase, and repeated, densely sampled data sets at very high resolution are being collected. Determining erosion rates across a landscape over shorter time scales such as single storm events is clearly possible with this technology. What patterns of erosion will appear from these data sets? Will spatially correlated erosion rates appear? Interferometry is being used to detect mm to cm changes in ground surfaces. Could this technology also be used

to monitor landscapes for ridge migration? At what temporal and spatial scale will organized behavior become detectable?

Conclusion

The geometric conditions that favor divide migration in theoretical and experimental eroding drainage basins are neither extreme nor restrictive. Erosion rate variability due to short term processes, such as hillslope failures and knickpoint propagation, can give rise to larger scale, longer term behavior, as evidenced by divide migration. Variability in rainfall events and patterns, variations in substrate resistance across a drainage basin, and changes in tectonic deformation rates clearly must disturb erosive processes and generate nonuniform erosion across the landscape. In our physical erosion experiments, however, we have tried to minimize such variability, and divide migration is still a common feature. We suggest that divide migration can be generated by feedback and instabilities that arise from within the system, that is, such behavior is self-organizing and emergent.

Erosion rate variability can be thought of as more than just fluctuations around some average steady state value. Certainly, natural landscapes experience large ranges of storm, earthquake, and fire events that generate large local fluctuations in erosion. Over longer time scales, stream profiles might oscillate as knickpoints propagate through a network, leaving 'wakes' of increased erosion rates in their trail. With several mechanisms for altering erosion rates at a variety of time scales, erosion rates should exhibit a very rich spectra. Given the sensitivity of divide migration on erosion rate, and a positive feedback mechanism between differential erosion rates and divide migration via drainage area capture, long term drainage basin instability with varying length and time scales of organization may be a possibility.
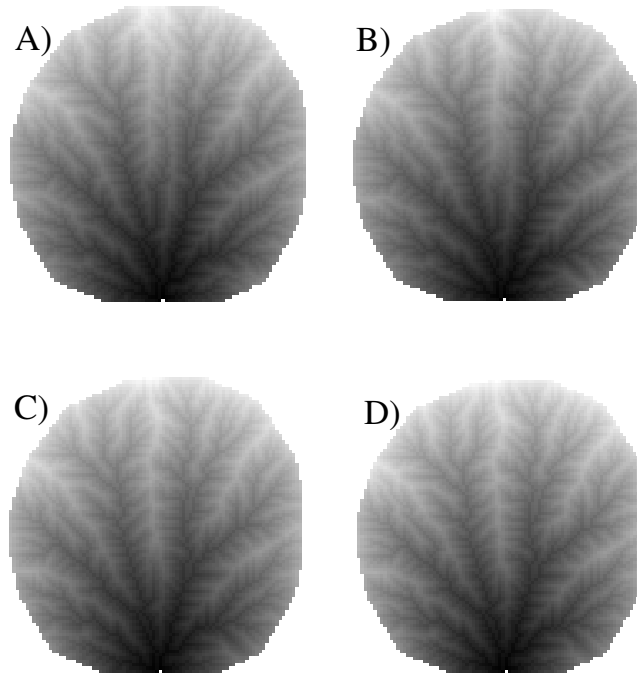
Figure 5-1. Time series elevations of valley closure in a numerical erosion model. Images are gray-scale elevation maps (white = highs, dark = lows). Width of each image is 89 cm (1.1 L). Grid resolution is 1 cm spacing. Range in elevation for each image is 16 cm (0.2 L = 1 H_r). A) A long narrow linear valley separates main ridges down the center of the image. Subsequent images show the closing of this valley from top to bottom. The rest of the landscape appears unaffected by the divide migration. Eroded distance from (A) to (D) is 16 cm (0.18 L, or 1 H_r). Input parameters to the numerical model are listed in the appendix.

Figure 5-2. Spatial erosion rates derived by differencing elevation fields in Figure 1. Erosion rates have been scaled to the spatial range in rate (dark is low, light is high erosion rate). Width of each image is 89 cm (1.1 L). Eroded distance between grids is 5.4 cm (0.33 H_r). Grid resolution is 1 cm. Most of the elevation field is experiencing uniform erosion (gray). The valley clearly is eroding at a lower rate (black), with higher rates at the flanking ridges (white). Residual high rates of erosion along the ridge crest persist after the valley has 'closed', due to minor lateral migration of the main divide.
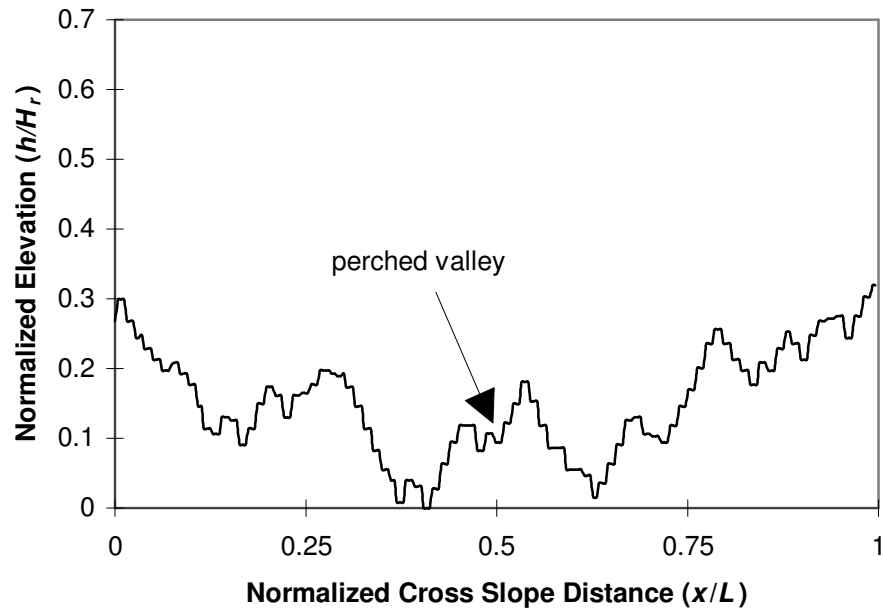
Figure 5-3. Cross slope topographic profile of numerical model elevation field shown in Fig. 5-1A. Cross slope distance (87 cm) has been normalized to L (basin width, in this case), and elevation has been normalized to the total relief in the landscape (16 cm). 'Stepped' nature of the profile reflects the grid resolution of the elevation model (1 cm/pixel). Arrow points to narrow perched valley in the process of 'closing'. Adjacent valleys of similar length are deeper than the perched valley.

Figure 5-4. Vertical photograph of landform in erosion facility after a steady balance between uplift and erosion has been reached. Width of basin is 87 cm. Maximum relief (from top of image to bottom) is 17.8 cm (1 H_r). Note the narrow valley in the lower center of the basin. Its upstream end is beheaded.
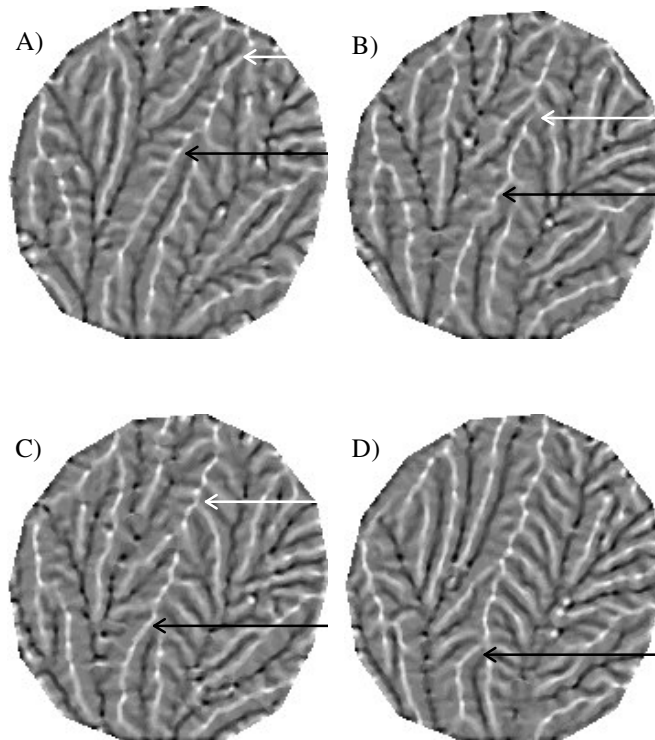
Figure 5-5. Time series elevations of ridge migration in the experimental erosion facility. Width of each image is 87 cm. Grid resolution is 0.5 cm spacing. Range in elevation for each image is 16 cm (0.18 L, or 1 H_r). A long linear valley extending from the outlet to the center of the image culminates in a ridge 'triple junction' (A, black arrow), and has progressively closed by (D). Similar valley closures occur between (A) and (B) in the upper left side of the images, and from (A) to (D) on the right side of the images. Other ridges have migrated in the absence of valley closure (white arrows). Eroded distance from (A) to (D) is 13.5 cm (0.8 H_r).
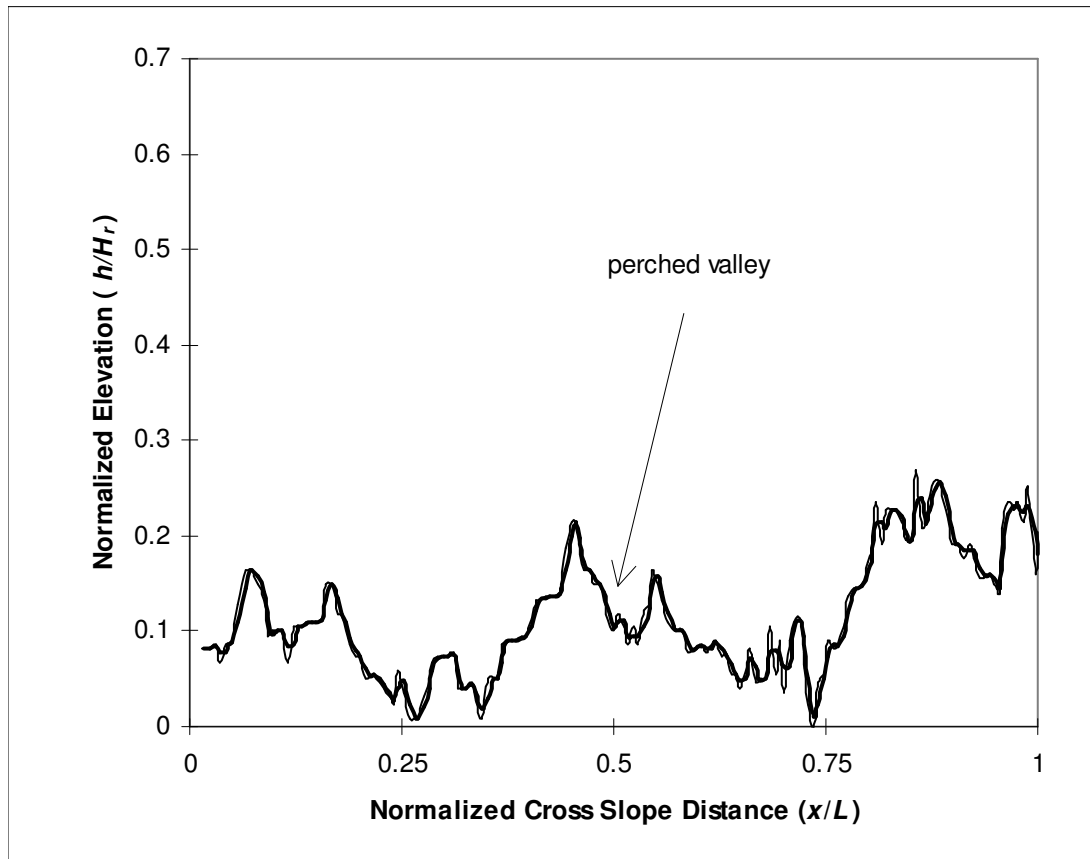
Figure 5-6. Cross slope topographic profile physical experiment elevation field shown in Fig. 5-5A. Cross slope distance (89 cm) has been normalized to L (basin width, in this case), and elevation has been normalized to the total relief in the landscape (17.8 cm). Adjacent valleys are deeper than the perched valley.
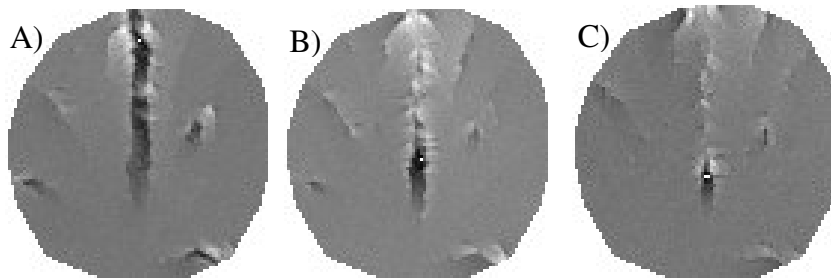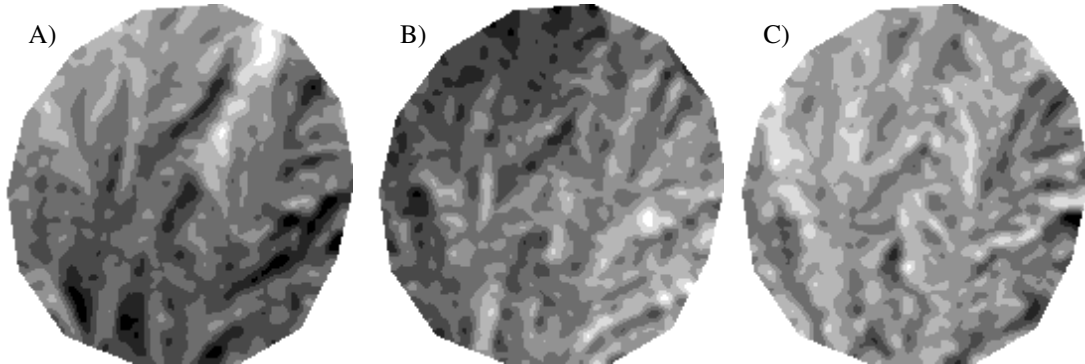
Figure 5-7. Spatial erosion rates derived by differencing experimental elevation fields in Figure 5. Erosion rates have been scaled to the spatial range in rate as 8 grays (dark is low, light is high erosion rate). Width of each image is 89 cm (*L*). Eroded distance between grids is A) 4.2 cm (0.26 H_r), B) 4.6 cm, and C) 4.6 cm (0.28 H_r). Grid resolution is 0.7 cm/pixel. Spatial patterns of erosion are far more complex than the numerical case presented earlier (Figure 3), due to pervasive migration of ridges and valleys, as well as valley annihilation via closure.
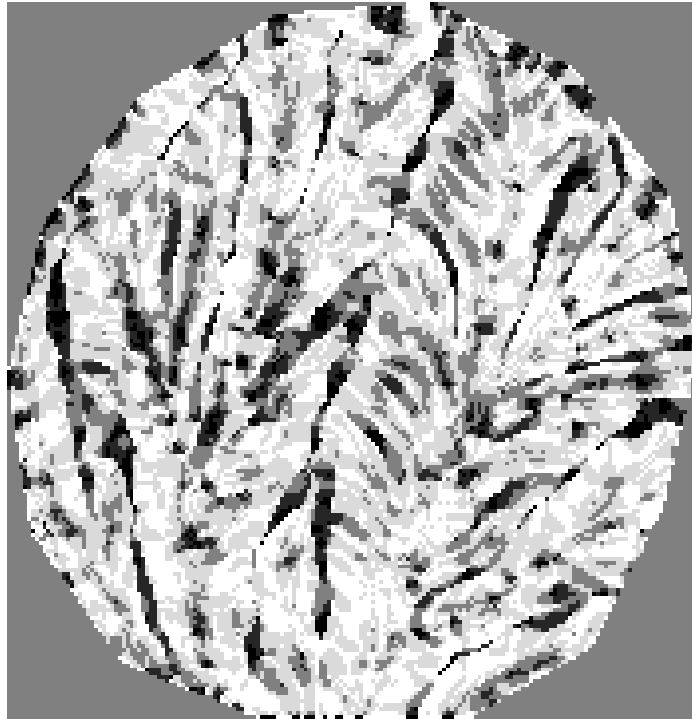
Figure 5-8. Spatial map of local flow direction change, computed for experimental elevation fields in Fig. 5-5B and 5-5C. Spatial patterns appear as linear trends. Dark values indicate flow reversal, and light areas indicate no change in flow direction.
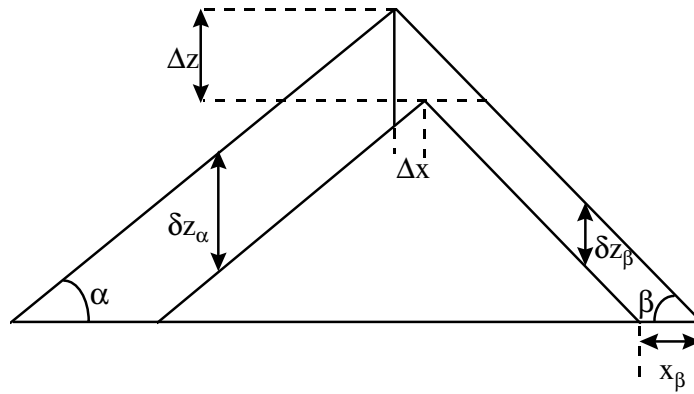
Figure 5-9. Diagram of ridge crest migration (Δx) due to differential erosion rates (δz_a and δz_b) on opposites side of a ridge. The rate of migration depends on erosion rate differences and hillslope angles, α and β.
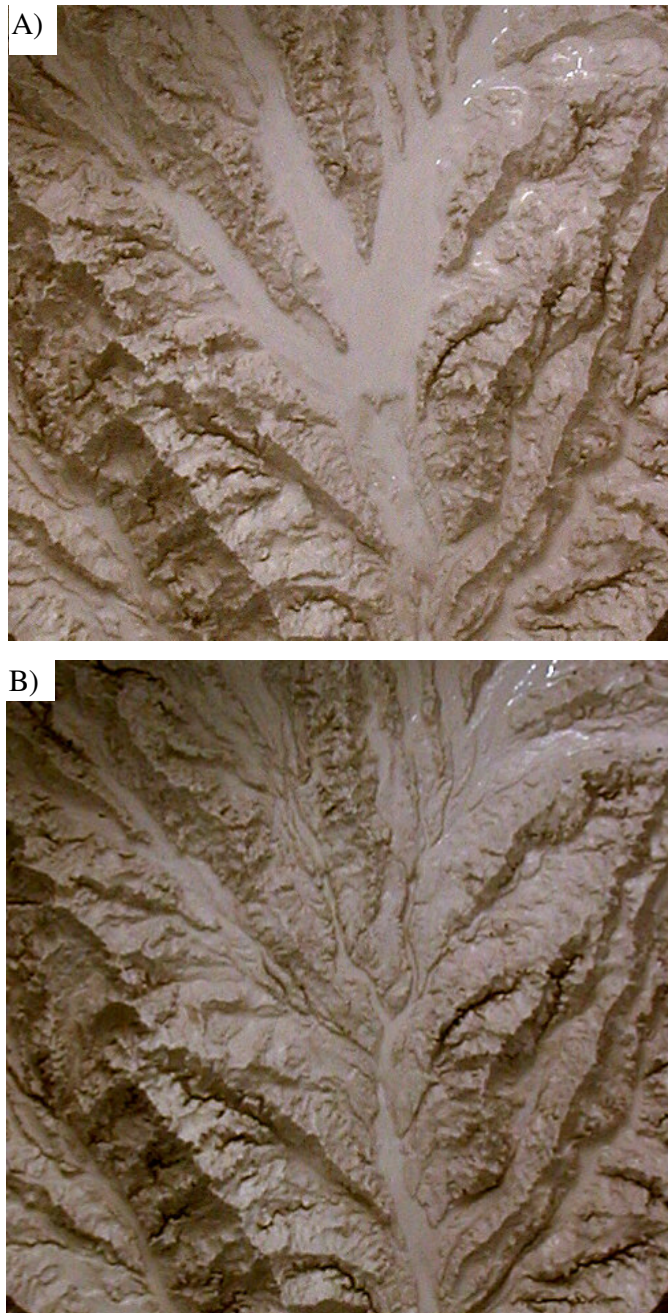
Figure 5-10 Temporary sediment storage, followed by excavation in physical experiment. Width of each photograph is 50 cm. A) A knickpoint is incising into a sediment filled area. Note a second knickpoint is following the first (bottom center of photo). B) Same area as in A, 20 minutes later (base level change of ~3 mm). Sediment has been excavated. Narrow deep channels now occupy the area.

Chapter 6

Conclusion and Future Directions

Discussion of Results

The main goal of this thesis was to develop a physical experiment that would provide a suitable long term comparative test for the stream power erosion model. The stream power model is quite powerful and flexible. By varying erosion law parameters, a remarkable range of landscape form, such as relief, hillslope profiles, drainage density, and stream profile concavity can be modeled (Tucker and Bras, 1998). These models usually start with an initially random rough surface, and evolve into a completely integrated drainage basin. The simplicity and successful replication of commonly observed statistical properties of natural drainage basins has led many researchers to conclude that the model should also capture the dynamic behavior of eroding landscapes. Indeed, the stream power model has kinematic wave solutions to perturbations in uplift rate (Whipple and Tucker, 2000). In the absence of independent calibration of erosion parameters, the 'tune-ability' of the erosion law to replicate form does not allow for rigorous testing of the model based on form alone. However, the stream power erosion model develops stationary uniformly eroding landforms for *any* set of parameters employed in the model. Thus, a testable result from this model is its stable form at steady forcing.

In order to test the erosion model with an experimental erosion facility, several key conditions have to be met. These include runoff based erosion, a homogeneous substrate, and steady uniform forcing from rainfall and uplift. The experimental erosion facility developed 3-5 order drainage basins that eroded through several units of relief at demonstrably stable forcing, and thus represents a first order test of the uniformly eroding drainage basin hypothesis. It is worth noting that these physical experiments were the first of their kind to enforce continuous uplift for long periods of erosion.

None of the physical experiments, even those that eroded through more than 3 H_r, developed the uniform erosion condition exhibited by numerical model simulations. While a constant *statistical* form was attained, as reflected by stable relief, steady

172

sediment flux at the outlet, and stable slope distributions, experimental landforms experienced continuous modifications, both at small local scales (hillslope failures and migrating knickpoints) as well as larger temporal and spatial scales (ridge growth, migration, and annihilation). For all run conditions, experimental streams do not erode uniformly over the profile, but develop migrating knickpoints. Episodic deposition and re-incision within trunk valleys further stymies uniform erosion. This is strongly suggestive that experimental streams are always at or near carrying capacity, and small changes in slope or sediment supply from hillslopes are sufficient to cause deposition. The streams are not operating at detachment limited conditions (assumed in the implementation of the stream power law), but at capacity limited conditions. Apparently, a purely erosional landform is not possible using the granular substrate or cohesion employed in these physical experiments. One must conclude that while the physical experiments clearly mimic the steady forcing conditions in numerical simulations, the presence of several mass transport processes in physical experiments limits the rigor of the test.

As an additional test of the applicability of a single erosion law to the physical experiment, the ratio of exponents (m/n) in the stream power law should remain constant while uplift is varied (that is, they are independent of forcing). Recall that the exponent θ in the area-slope relation is equivalent to m/n. Systematic changes in θ with respect to forcing conditions implies that a single erosion law is not applicable. A range of uplift and rainfall rates were enforced between experimental runs, and θ exhibited some dependence on forcing conditions. This suggests that a single process erosion law does not adequately account for the various processes occurring in the physical experiments.

The value in performing physical experiments, however, does not solely hinge upon a binary outcome of success or failure in simulating a theoretical construct. The physical experiments provide a fascinating view into the internal interactions that are possible within an eroding drainage basin. How *do* landscapes erode? Are slope failures randomly distributed events? Is there temporal and/or spatial organization to eroding landscapes?

Are slope failures and knickpoint migration tightly linked? Is temporary sediment storage in valleys contingent upon hillslope failures?

Time lapse video of each run offers some means of answering these questions. Digitized videos are available for viewing on the CD-ROM supplied with this thesis document. They document upstream propagation of information via knickpoint migration, slope failures, and temporary sediment storage. They further demonstrate changes of the ridge and valley structure over time. Divides can migrate, extend, shorten, and experience annihilation. This aspect of long term evolution is partially captured by numerical simulations prior to reaching a stable drainage basin configuration. The physical experiments do not appear to reach such a stable state. Inevitably, one is left with the wish that the run were continued for a much longer period of time. Geologically, this time scale of erosion (several H_r), is approaching the limit (in terms of rock exhumation) of what is actually measured in field.

The landform dynamism exhibited by the physical experiments offers a contrasting view to numerical model stability. It is the view of this author that numerical and physical experiments should be taken as complimentary approaches to understanding the evolution and erosional behavior of drainage basins. They share some features in common. Both models develop fully extended drainage basins of order 3 to 5 over the scales studied in this thesis. Both exhibit divide migration at some stage in the evolution of the drainage basin. For the numerical models, migration results in a more stable configuration of the stream network. For the experimental facility, divide migration continues over time, and no completely stable configuration has been observed for experimental runs. The physical experiments exhibit additional processes not captured by the numerical model, namely, hillslope failures, deposition, and knickpoint development. Some combination of these processes may be sufficient to destabilize the network, and open up the possibility of persistent long term variability in erosion rates and continual drainage basin configuration.

What can we learn from the physical experiments? 1) A *statistically stable* form is a clear possibility for eroding drainage basins. A well-defined average relief, slope, and

characteristic roughness develops for each set of forcing conditions. Hillslope form in the physical experiments also varies, with nearly linear hillslopes at low *r/u* conditions, and highly concave profiles for high *r/u* conditions. Landscape form is dependent on the combined effects of uplift and runoff. This implies that we should be able to deduce long term average forcing conditions based on the form of the landscape. Substrate resistance to erosion, as well as landscape vegetative characteristics, will complicate such interpretations, and further work on the influence of rock erodibility and vegetation on landscape form needs to be conducted. 2) *Process activity* is sensitive to forcing from runoff and uplift. Hillslope failure activity varies between runs, decreasing with *r/u*. Hence, process activity provides another clue to forcing conditions, and we may be able to place constraints on forcing based on process activity. Again, substrate resistance must play a role in hillslope stability, and must be taken into consideration. 3) *Stream terraces* in natural drainages have traditionally been interpreted as changes in climate conditions or uplift rates. Terraces are visible in many of the physical experiments. Internal process interactions can generate terraces in the absence of *changes* in forcing. Epicycles of temporary sediment storage and re-incision frequently occur in physical experiments. During re-incision, knickpoints develop and migrate upstream, often leaving terraces in their wake. Terraces are more prevalent in runs with lower *r/u* numbers, where mass movements play a more significant role in eroding the landscape. The intrinsic dynamics exhibited by the physical experiments raise intriguing questions concerning process interactions in natural settings. In locations where long term uplift is occurring, a fruitful approach of mapping terraces, knickpoints, and sediment storage areas may offer some evidence for similar epicycles in natural settings. Substantial changes in climate have occurred globally, but some locations may not have experienced significant changes in erosive processes (e.g., glaciation). At the very least, *intrinsic* generation of terraces, deposition, and knickpoints should be considered as a possibility, before climate change is invoked as the explanation of such features. Independent evidence of climate change, preferably in the form of temperature and rainfall/runoff proxies should be sought when sorting out the controls on terrace formation in field settings. 4) In the same vein of

intrinsic dynamics, local erosion rate variability and changes in flow direction appear to be independent of forcing conditions. Erosion rate variability increases at shorter time scales of observation, and flow direction change accumulates at longer time scales. The lack of dependence on forcing suggests that such changes might be inherent to drainage basins where streams are transport capacity limited. Landscape evolution under capacity limited conditions is tantalizingly predictable (landform approaches exact similitude at short time scales of change), and frustratingly stochastic (erosional variability increases at the shortest time scales of observation). The experimental landforms are clearly not drastically altering their drainage structure over short time scales, but over time incremental changes accumulate to fundamentally change the drainage structure of the landform. 5) As with numerical landforms, physical experiments share a great deal in common with natural eroding drainage basins. Slopes tend to be higher in experimental landforms. Breaks in scaling in the area-slope relation, often observed for natural drainage basins (Dietrich et al., 1993), also exist for some run conditions.

Experimental Research Directions

Several future research directions are suggested by this thesis. 1) A numerical model that incorporates transport limited conditions, with thresholds for erosion, deposition, and knickpoint generation should be developed. The implementation would require that transport rates and sediment concentration in the flow be computed at each time step. Some iteration between computed erosion rate, sediment routing, and adjustment of erosion rate based on sediment concentration would also be required. Possible destabilizing effects exist in the interactions between incision and deposition, and these need to be explored in greater detail. 2) A physical experiment that lacks any dependence on transport rate should be developed. This would entail a substrate with a finite resistance to shear stress, that once eroded is easily transported out of the system. This could be a substrate that dissolves, such as halite, calcite, gelatin (i.e., 'jello'), or gypsum. A truly detachment limited condition is required to rigorously test the stream power erosion law, and a dissolving substrate could be the solution. Stability of the landform under steady base level fall and rainfall conditions could be investigated. 3) The effect of

substrate resistance to shear stress should also be conducted. Gilbert (1877) hypothesized that where rocks are hard, slopes are high. Informal tests of erodibility suggest that channel geometry is very sensitive to bed resistance, that is, channels steepen, deepen, and narrow in more resistant materials. This effect could have profound influences on landscape behavior. Deep narrow channels, if cut deep enough, could induce large slope failures that drastically alter the stream network. It is also possible that balancing uplift with erosion is not attainable for very resistant substrates, and a range in resistance should be investigated. 4) Identify regions in natural landscapes that are eroding faster. This could be accomplished by visual inspection of channel arrangements and slopes. For instance, long narrow valleys could well be the locus of encroachment by adjacent drainage basins. Sediment flux measurements, or erosion rates measurements derived from cosmogenic nuclides, could provide additional constraints on erosion rates in adjacent basins. One could also compute erosion rates based on numerical models for erosion, given the topography. Such a study has been performed for the Himalaya (Finlayson et al., 2002). They observed highly variable (computed) erosion rates. Such efforts should be expanded to investigate local patterns of erosion rate. Locally paired high and low erosion rate patterns could delineate regions of the drainage basin where divides are migrating. 5) Investigate the effect of rainfall temporal variability on landscape form and behavior. For run 1, the ground surface was allowed to dry out overnight, and the response upon rehydration involved significant overshoots from the steady state average sediment flux. Streams incised as sediment supply from hillslopes was low prior to rehydration. Once fully wetted, hillslope failure activity increased due to the incision by streams. This is a very intriguing situation. If a landform is rarely at saturated hillslope conditions, will it erode differently than the saturated case? Will hillslope failures increase in size and decrease in frequency? These are unanswered questions that could be addressed with a physical experiment. Further, one could impose a range of rainfall event sizes. Is the behavior over longer times substantially different than a continuous, steadily forced landscape?

The experiments conducted for this thesis represent a base line of behavior and form for experimental landscapes. A variety of landforms are possible for experimentalists, and a rich avenue of exploration and model testing is available. Automation and monitoring methods are increasingly available, and exquisitely detailed data sets will offer further rigorous tests of theoretical constructs of erosion, as well as insight into the relationships between form, forcing, and substrate properties. It is the firm belief of this researcher that experimental, observation based exploration coupled with theoretical modeling will open up new ways of understanding topographic form and process in the field, as well as identify avenues for future research.

Summary of Thesis

The stream power erosion law was implemented in a numerical landscape evolution model. Additional terms were added to the erosion law to account for local diffusion, slope aspect driven diffusion, spatial and temporal variation in rainfall, and temporal variation in uplift. Simulations were conducted within a basin that maintained similar boundaries as an experimental erosion facility. Time series of elevation were extracted from each run. The goal of this part of the thesis was to verify that a numerical erosion model based on stream power developed stable, uniformly eroding landforms. While divide migration was noted after a balance between uplift and erosion was attained, such adjustments to the drainage basin structure resulted in a more stable configuration. The addition of diffusion to the erosion law, and variation in rainfall patterns and gradually varied uplift did not destabilize the landform.

An erosion facility was constructed to test the uniformly eroding drainage basin proposition. The facility consists of an oval tank 1 m deep, 1 m long, and 0.87 m wide. A motor-controlled outlet provided a constant base level fall condition, equivalent to uniform block uplift of the substrate. A rainfall apparatus supplied a fine mist over the surface, generating surface runoff. The substrate consisted of silica flour (d50 = 45 mm) mixed with 1 weight percent kaolinite. A series of 7 runs were conducted where uplift rate and rainfall intensity were varied between runs. Substrate properties were not varied between runs.

A drainage basin of order 3-5 developed for each run, and eroded through at least 1 H_r (relief at dissection) after the initial flat surface was completely dissected. Surface runoff was the dominant erosional process for all runs, but hillslope failures (activity dependent on forcing conditions), temporary deposition in valleys, and knickpoint generation and migration were also observed. Each run was monitored with time lapse video, stereo photography. Sediment and water fluxes were measured at the outlet of the basin. Elevation fields were derived from stereo photographs, and relief, slope, contributing area, and elevation statistics were extracted from the elevation data sets. Relief, slope, surface roughness, and to a lesser degree, drainage density are strongly dependent on uplift rate and rainfall intensity.

While a statistical steady form developed for each run, all of the experimental landforms failed to replicate the spatially uniform erosion exhibited by numerical erosion models at long term steady forcing. Nonuniform erosion was evidenced at the shortest time scales by hillslope failures, deposition, and knickpoint propagation. Divide migration, and ridge extension and annihilation, were observed long after the landform had attained a balance between erosion and uplift. Intrinsic process interactions spawned a rich dynamics in experimental landscapes, as hillslope failures, episodic cycles of deposition and incision, drainage rearrangement, terrace formation, and knickpoint migration pulsed over broad scales in time and space.

Bibliography

Adams, J., Contemporary uplift and erosion of the Southern Alps, New Zealand: Geological Society of America Bulletin, v. 91, p. 1–114, 1980.

Ahnert, F., Functional relationships between denudation, relief, and uplift in large mid-latitude drainage basins: American Journal of Science, v. 268, p. 243–263, 1970.

Armstrong, P. A., T. A. Ehlers, P. J. J. Kamp, K. A. Farley, and D. S. Chapman, Tracking changes in exhumation rates using low-temperature thermochronometry: an example from the Wasatch mountains, Utah (USA), in 9th International conference on fission track dating and thermochronology, eds. W.P. Noble, P.B. O'Sullivan, and R. W. Brown, Geol. Soc. Austral. Abstr., 58, 355-356, Lorne, 2000.

Batt, G.E., Braun, J., Kohn, B.P., and McDougal, I., Thermochronological analysis of the dynamics of the Southern Alps, New Zealand: Geological Society of America Bulletin, v. 112, p. 250–266, 2000.

Beaumont, C., P. Fullsack, P., and J. Hamilton, Erosional control of active compressional orogens, in Thrust Tectonics, ed. McClay K. R., Chapman and Hall, 1-18, 1992.

Bernet, M., Zattin, M., Garver, J.I., Brandon, M.T., and Vance, J.A., Steady-state exhumation of the European Alps: Geology, v. 29, p. 35–38, 2001.

Bierman, P. R., Use of in situ-produced cosmogenic isotopes to determine rates of geomorphic processes, Snowbird, Utah: AGU, Chapman Conf. Tectonics and Topography, 34, 1992.

Brandon, M. T., M. K. Roden-Tice, and G. I. Garver, Late Cenozoic exhumation of the Cascadia accretionary wedge in the Olympic mountains, northwest Washington State, Geol. Soc. Am. Bull., 110, 985-1009, 1998.

Braun, J., and Sambridge, M., Modelling landscape evolution on geological time scales: A new method based on irregular spatial discretization: Basin Research, v. 9, p. 27–52, 1997.

Brown, E. T., R. F. Stallard, M. C. Larsen, G. M. Raisbeck, and F. Yiou, Denudation rates determined from the accumulation of in situ-produced ^{10}Be in the Luquillo Experimental Forest, Puerto Rico. Earth and Planetary Science Letters, 129, 193-202, 1995.

Burbank, D. W., Rates of erosion and their implications for exhumation, Mineralogical Magazine, Vol. 66(1), pp. 25-52, 2002.

Czirok, A., E. Somfai,, and T. Vicsek, Experimental evidence for self-affine roughening in a micromodel of geomorphological evolution, Physical Review Letters, 71, 2154-2157, 1993.

Crave, A., Lague, D., Davy, P., Kermarrec, J. J., Sokoutis, D., Bodet, L., and Compagnon, R., Analogue modelling of relief dynamics: Physics and Chemistry of the Earth (A), v. 25, p. 549-553, 2000.

Densmore, A.L., Ellis, M.A., and Anderson, R.S., Landsliding and the evolution of normal-fault-bounded mountains: Journal of Geophysical Research, v. 103, p. 15 203–15 219, 1998.

Dietrich, W. E., Wilson, C. J., Montgomery, D. R., and McKean, J., Analysis of erosion thresholds, channel networks, and landscape morphology using a digital terrain model, Journal of Geology, v. 101, p. 259-278, 1993.

Erickson, P. A., and D. J. Harbor, Bringing down Floyd; incision by the James River in the Valley and Ridge of Virginia, Abstracts with Programs, Geological Society of America, 30 (7), p. 142, 1998.

Farley, K.A., Helium diffusion from apatite: General behavior as illustrated by Durango fluorapatite: Journal of Geophysical Research, v. 105, p. 2903–2914, 2000.

Fuller, C. W., Willett, S. D., Hovius, N., and Slingerland, R. L., Variability in erosion rates due to discrete supply processes in the eastern Central Range, Taiwan, Anonymous, Earth system

processes; programmes with abstracts, Meeting: Earth system processes, Edinburgh, United Kingdom, p. 87, 2001.

Gilbert, G.K., Geology of the Henry Mountains: U.S. geographical and geological survey of the Rocky Mountain region: U.S. Government Printing Office, Washington, D.C., 160 p., 1877.

Gleadow, A.J.W., and Brown, R.W., Fission-track thermochronology and the long-term denudational response to tectonics, in Summerfield, M.A., ed., Geomorphology and global tectonics: Chichester, Wiley, p. 57–75, 2000.

Granger, D. E., J. W. Kirchner, and R. Finkel, Spatially averaged long-term erosion rates measured from in situ-produced cosmogenic nuclides in alluvial sediment, J. Geol., 104, 249-257, 1996.

Hack, J.T., Interpretation of erosional topography in humid temperature regions: American Journal of Science, v. 258-A, p. 80–97, 1960.

Hack, J.T., Dynamic equilibrium and landscape evolution, in Melhorn, W.N., and Flemal, R.C., eds., Theories of landform development: Publications in Geomorphology, Binghamton, State University of New York, p. 87–102, 1976.

Hancock, G., Experimental testing of the Siberia landscape evolution model. Ph.D. thesis, Univ. of Newcastle, New South Wales, Australia, 1997.

Hancock, G., Experimental testing of the Siberia landscape evolution model. Ph.D. thesis, Univ. of Newcastle, New South Wales, Australia, 1997.

Harbor, David J., Landscape evolution at the margin of the Basin and Range, Geology, v. 25, no. 12, p. 1111-1114, 1997.

Harbor, David J., Nonuniform erosion patterns in the Appalachian Mountains of Virginia, Abstracts with Programs, Geological Society of America, 28 (7), p. 116, 1996.

Hasbargen, L. E., and C. Paola, Landscape instability in an experimental drainage basin, Geology, 28, 1067-1070, 2000.

Hasbargen, Leslie E., and Chris Paola, How predictable is local erosion rate in eroding drainage basins? in Prediction in Geomorphology, eds. P. Wilcock and R. Iverson, AGU Geophysical Monograph 135, 2003.

Heimsath, A. M., W. E. Dietrich, K. Nishiizumi, and R. C. Finkel, Cosmogenic nuclides, topography, and the spatial variation of soil depth, Geomorphology, v. 27, p. 151-172, 1999.

Horton, R., Erosional development of streams and their drainage basins; hydrophysical approach to quantitative morphology, Geological Society of America Bulletin, v. 56, p. 275-370, 1945.

Hovius, N., C. P. Stark, and P. A. Allen, Sediment flux from a mountain belt derived by landslide mapping, Geology, 25, 231-234, 1997.

Hovius, N., C. P. Stark, H. Chu, and J. Lin, Supply and removal of sediment in a landslide-dominated mountain belt; Central Range, Taiwan, J. Geol., 1081, 73-89, 2000.

Howard, A. D., A detachment-limited model of drainage basin evolution, Water Resour. Res., 30, 2261-2285, 1994.

Howard, A.D., Geomorphic systems, equilibrium and dynamics: American Journal of Science, v. 263, p. 302–312, 1965.

Howard, A.D., Equilibrium and timescales in geomorphology: Application to sand-bed alluvial streams: Earth Surface Processes and Landforms, v. 7, p. 303–325, 1982.

Howard, A.D., Equilibrium models in geomorphology, in Anderson, M.G., ed., Modelling geomorphological systems: New York, Wiley, p. 49–72, 1988.

Kooi, H., and Beaumont, C., Large-scale geomorphology: Classical concepts reconciled and integrated with contemporary ideas via a surface processes model: Journal of Geophysical Research, v. 102, p. 3361–3386, 1996.

Koons, P.O., The topographic evolution of collisional mountain belts: A numerical look at the Southern Alps, New Zealand: American Journal of Science, v. 289, p. 1041–1069, 1989.

Kuhlemann, J., Evidence from sediment budget calculations for Miocene large scale shifts of the drainage divide in the Swiss and western Alps, in: B. Sze'kely, W. Frisch, J. Kuhlemann, and I. Dunkl (Eds.), 4th Workshop on alpine geological studies. Tubinger geowiss. Arb. Series A 52, 163-165, 1999.

Kramer, S, and M. Marder, Evolution of river networks. Physical Review Letters, v. 68, no. 2, p. 205-208, 1993.

Lague, D., P. Davy, and A. Crave, Estimating uplift rate and erodibility from the area-slope relationship: examples from Brittany (France) and numerical modelling, Phys. Chem. Earth (A), v. 25, no. 6-7, pp. 543-548, 2000.

Lague, D., and P. Davy, Constraints on the long-term colluvial erosion law by analyzing slope-area relationships at various tectonic uplift rates in the Siwaliks Hills (Nepal), in press, Journal of Geophysical Research, 2002.

Lal, D., Cosmic ray labeling of erosion surfaces: in situ nuclide production rates and erosion models, Earth Planet. Sci. Lett., 104, 424-439, 1991.

Leheny, R., and S. Nagel, Model for the evolution of river networks. Physical Review Letters, v. 71., no. 9, p. 1470-1473, 1993.

Loewenherz-Lawrence, D., Hydrodynamic description for advective sediment transport processes and rill initiation. Water Resources Research, v. 30, no. 11, pp. 3203-3212, 1994.

Martin, Y., K. Rood, , J. W. Schwab, and M. Church, Sediment transfer by shallow landsliding in the Queen Charlotte Islands, British Columbia, Can. Journ. Earth Sci., v. 39, no. 2, 189-205, 2002.

Mather, A. E., Harvey, A. M., Stokes, M., Quantifying long-term catchment changes of alluvial fan systems, Geological Society of America Bulletin, 112 (12), p. 1825-1833, 2000.

Matmon, A., Bierman, P. R., Larsen, J., Southworth, S., Pavich, M., and Caffee, M., Temporally and spatially uniform rates of erosion in the Southern Appalachian Great Smoky Mountains, Geology (Boulder), 31 (2), p. 155-158, 2003.

Matmon, A., P. Bierman, S. Southworth, M. Pavich, and M. Caffee, Temporally and spatially uniform rates of erosion in the Great Smoky Mountains, GSA Abstracts with Program, Annual Meeting, November 5-8, 2001.

Meigs, A., N. Brozovic, and M. L. Johnson, Steady, balanced rates of uplift and erosion of the Santa Monica Mountains, California, Basin Research, v. 11, 59-73, 1999.

Melton, M., Geometric properties of mature drainage systems and their representation in an E4 phase space. Journal of Geology, v. 66, p. 35-54, 1958.

Merritts, D. J., and K. R. Vincent, Geomorphic response of coastal streams to low, intermediate, and high rates of uplift, Mendocino triple junction region, northern California, GSA Bulletin, 101, 1373-1388, 1989.

Miller, J., D. Germanoski, K. Waltman, R. Tausch, and J. Chambers, Influence of late Holocene hillslope processes and landforms on modern channel dynamics in upland watersheds of central Nevada, Geomorphology, 38, 373–39, 2001.

Moglen, G. E., and R. L. Bras, The importance of spatially heterogeneous erosivity and the cumulative area distribution within a basin evolution model, Geomorphology, 12, p. 173-185, 1995.

Montgomery, D. R., and M. T. Brandon, Topographic controls on erosion rates in tectonically active mountain ranges, Earth and Planetary Science Letters 201, p. 481-489, 2002.

Parker, R. S., Experimental study of basin evolution and its hydrologic implications. Ph.D. thesis, Colorado State Univ., Fort Collins, 1977.

Pederson, D. T., Stream Piracy Revisited; a groundwater-sapping solution, GSA Today, 11 (9), 4-10, 2001.

Penck, W., Die Morphologische Analyse: Verlag Von J. Nachf., Stuttgart, 283 pp., 1924.

Phillips, J. D., The end of equilibrium?: Geomorphology, v. 5, p. 195–201, 1992.

Schumm, S.A., and Lichty, R.W., Time, space and causality in geomorphology: American Journal of Science, v. 263, p. 110–119, 1965.

Phillips, L. F., and S. A. Schumm, Effect of regional slope on drainage networks, Geology, 15, 813-816, 1987.

Reneau, S., and W. Dietrich, Erosion rates in the southern Oregon Coast Range: Evidence for an equilibrium between hillslope erosion and sediment yield, Earth Surf. Processes Landforms, 16, 307-322, 1991.

Riebe, Clifford S., J. W. Kirchner, D. E. Granger, and R. C. Finkel, Erosional equilibrium and disequilibrium in the Sierra Nevada, inferred from cosmogenic ^{26}Al and ^{10}Be in alluvial sediment, Geology, 28, 803–806, 2000.

Ries, J., Merritts, D., Harbor, D., Gardner, T., Erickson, P., and Carlson, M., Increased rates of fluvial bedrock incision in the Central Appalachian Mountains, Virginia, Abstracts with Programs, Geological Society of America, 30 (7), 1998.

Rigon, R., A. Rinaldo, I. Rodriguez-Iturbe, R. Bras, and E. Ijjasz-Vasquez, Optimal channel networks: a framework for the study of river basin morphology, Water Resour. Res., 29, 1635-1646, 1993.

Rinaldo, A., I. Rodriguez-Iturbe, R. Rigon, R. Bras, E. Ijjasz-Vasquez, A. Marani, Minimum energy and fractal structures of drainage networks, Water Resour. Res, 28, 2183-2195, 1992.

Roe, G. E., Montgomery, D. R., and Hallet, B., Effects of orographic precipitation variations on the concavity of steady-state river profiles, *Geology*; v. 30; no. 2; p. 143–146, 2002.

Shepherd, R. G., and S. A. Schumm, Experimental study of river incision, GSA Bulletin, 85, no. 2, 257-268, 1974.

Shreve, R. L., Infinite topologically random channel networks, J. Geol, 75, 178-186, 1967.

Shreve, R. L., The probabilistic-topologic approach to drainage-basin geomorphology, Geology, 3, 527-529, 1975.

Sklar, L., and W. Dietrich, River longitudinal profiles and bedrock incision models: Stream power and the influence of sediment supply, in Rivers over rock: Fluvial Processes in Bedrock Channels, Geophys. Monogr. Ser., vol. 107, edited by K. J. Tinkler and E. E. Wohl, pp. 237-260, AGU, Washington D. C., 1998.

Snyder, N. P., K. X. Whipple, G. E. Tucker, and D. J. Merritts, Landscape response to tectonic forcing: DEM analysis of stream profiles in the Mendocino triple junction region, northern California, Geol. Soc. Am. Bull., 112 (8), 1250-1263, 2000.

Strahler, A.. Equilibrium theory of erosional slopes approached by frequency distribution analysis. American Journal of Science, v. 248, p. 673-696, 800-814, 1950.

Stuwe, K., White, L., and Brown, R., The influence of eroding topography on steady-state isotherms. Application to fission track analysis: Earth and Planetary Science Letters, v. 124, p. 63–74, 1994.

Stuwe, K., and M. Hintermuller, Topography and isotherms revisited: the influence of laterally migrating divides, Earth and Planetary Science Letters, 184, p. 287-303, 2000.

Tippett, J.M. and Kamp, P.J.J., Quantitative relationships between uplift and relief parameters for the Southern Alps, New Zealand, as determined by fission track analysis. Earth Surface Processes and Landforms, 20, 153-175, 1995.

Tucker, G. E., and R. L. Bras, Hillslope Processes, Drainage Density, and Landscape Morphology, Water Resources Research, 1998.

Whipple, K. X., and G. E. Tucker, Dynamics of the stream-power river incision model: Implications for height limits of mountain ranges, landscape response timescales, and research needs, J. Geophys. Res., 104, 17,661-17,674, 1999.

Whipple, K.X., Fluvial landscape response time: How plausible is steady state denudation?: American Journal of Science, v. 301, p. 313–325, 2001.

Willett, S. D., and M. Brandon, On steady states in mountain belts, Geology, v. 30, no. 2, p. 175–178, 2002.

Willett, S. D., Orogeny and orography: The effects of erosion on the structure of mountain belts: Journal of Geophysical Research, v. 104, p. 28 957–28 981, 1999.

Willett, S. D., Slingerland, R., and Hovius, N., Uplift, shortening and steady state topography in active mountain belts: American Journal of Science, v. 301, p. 455–485, 2001.

Willgoose, G., R. Bras, and I. Rodriguez-Iturbe, A coupled channel network growth and hillslope evolution model, 1. Theory, Water Resour. Res, 27, 1671-1684, 1991.

Wolf, P. R., Elements of Photogrammetry, Second Edition, McGraw-Hill Book Company, 1983.

Appendix A

Landscape Instability In An Experimental Drainage Basin

ABSTRACT

Do drainage basins develop static river networks when subject to steady forcing? While current landscape evolution models differ in formulation and implementation, they have the common characteristic that when run for long times at constant forcing, they evolve to a static steady state configuration in which erosion everywhere balances uplift rate. This results in temporally stationary ridge and valley networks. We have constructed a physical model of a drainage basin in which we can impose constant rainfall and uplift conditions. The model landscapes never become static, and they are not sensitive to initial surface conditions. Ridges migrate laterally, change length, and undergo topographic inversion (streams occupy former ridge locations). Lateral stream migration can also produce strath terraces. This occurs without any change in external forcing, so the terraces must be considered autocyclic. The experimental drainage basin also exhibits autocyclic (internally generated) oscillations in erosion rate over a variety of time scales, despite constant forcing. The experimental landforms are clearly not perfect analogs of natural erosional networks, but the results raise the possibility that natural systems may be more dynamic than the current models would suggest, and that features like strath terraces that are generally interpreted in terms of external forcing may arise autocyclically as well.

INTRODUCTION

Historically, the idea of a static erosional network with uplift everywhere balanced by erosion has deep roots. Playfair (1802) described drainage basins as trees, each stream delicately adjusted such that at each joining of streams, the slopes were delicately balanced. The systematic change of slope within landscapes suggested to Playfair that an equilibrium existed between erosion and sediment transport over the entire basin, and a stable geometry resulted from this balance. Gilbert (1877) noted that erosional landforms

have convergent stream networks and divergent ridge networks, and proposed that the typical concave-up profile of streams is due to the increased volume of water moving through downstream sections in the drainage network. He postulated that divides between adjacent streams must migrate toward the stream with a shallower gradient; stable channel networks are achieved once gradients in adjacent streams are similar. Instability of drainage lines could be explained in terms of differential resistance to erosion, differential uplift, time, and possibly the interaction between stream transport capacity and availability of sediment for transport. For Gilbert, the network of streams and hillslopes is a strongly interactive system, delicately adjusted at dynamic equilibrium to a stable form. Strahler (1950) characterized erosional landscapes as open mass-transport systems that adjust their morphology to attain a time-independent form. He measured valley-side slope angles from several completely dissected natural drainages, and showed that a given area maintains a characteristic slope with a narrow range of values. The presence of a characteristic slope lends support to the hypothesis of a stable landform. Hack (1960) hypothesized that every stream-hillslope pair is adjusted one to the other, and given constant forcing conditions, all elements of the landscape erode at the same rate, similar to Gilbert's dynamic equilibrium. Differences in form could, under those conditions, be related only to differences in resistance to flow, such as variable lithology and vegetation. Changes in the form could also result from changes in the forcing conditions, but responses to perturbations were fast enough to restore a dynamic steady state adjusted to the new boundary conditions. He explicitly viewed landscapes as spatial structures with time-independent forms.

NUMERICAL FORMULATIONS OF LANDSCAPE EROSION

In general, erosion is controlled by the resistance of the substrate to surface and body forces. The resistance is set by rock properties (crystal structure and chemistry, rock strength or cohesion, grain size), vegetative cover, and degree of saturation. Applied forces vary widely across natural landscapes: the scratching paws of burrowing animals; the pounding impact of rain drops; the torque of bending trees under the wind's impulse; soil expansion and contraction during saturating events and freeze-thaw; episodic failures

of oversteepened slopes; the thrashing torrents of streams; and the grinding mass of a sliding glacier, to name a few. The rate of disintegration of crystalline bedrock to smaller particles also sets a limit on the availability of transportable material. For modeling purposes, simplification is required at some level to obtain solutions to mass transport across the landscape.

Several landscape erosion models have been developed in recent years (Willgoose et al., 1991; Kramer and Marder, 1992; Chase, 1992; Leheny and Nagel, 1993; Howard, 1994; Tucker and Bras, 1998, for overview of models), and they differ in the means and degree of simplification of erosional processes that they employ. However, all of the models assume that forces applied by surface runoff dominate erosional processes in landscapes, and thus are based on routing water down the steepest slope in a numerical grid. Runoff is treated as steady, uniform flow, and this assumption allows the use of upstream drainage through a point as a proxy for stream flow at that point. Calculation of erosion depends on assumptions concerning the availability and transportability of sediment, but in general erosion rate is a function of local slope, discharge, uplift rate, and substrate resistance. The models develop landscapes with branching stream networks similar to natural drainage patterns (Chase, 1992; Leheny and Nagel, 1993), and even capture transient evolutionary features of the network such as extension and abstraction of streams (Glock, 1931; Kramer and Marder, 1992). Models based solely on stream erosion, however, develop slopes approaching infinity near drainage divides. While some natural landscapes have near vertical slopes, most hillslopes flatten near ridge crests. If a diffusive short-length scale process is added to the models, the resultant landforms develop rounded ridge crests, and the mean interfluve distance increases (Chase, 1992; Howard, 1994; Tucker and Bras, 1998). Local diffusion is meant to capture effects such as raindrop impact, bioturbation on hillslopes, and hillslope failures. We note that while the diffusive terms change the form of the numerical landscape, the models nonetheless achieve static landscapes at constant forcing. Numerical models suggest that the only requirements for a dendritic network to develop are detachment and removal of material from the system as water flows downhill. Furthermore, the strong negative feedback

between stream erosion and slope dampens perturbations and drives landscapes to stable forms over longer time scales. Constant boundary conditions inevitably result in stable networks. Thus, numerical models appear to validate conjectures by geomorphologists that landscapes can attain static perfectly adjusted forms. Tests of landform stability under constant forcing are difficult to conduct on natural landscapes because of the long time scale for significant landform change, and the uncertainties in climatic and tectonic history. Physical models of eroding drainage basins (Parker, 1977; Phillips and Schumm, 1987; Schumm et al., 1987; Hancock, 1997) represent a possible means of testing landscape stability, because steady climatic and tectonic boundary conditions can be enforced, and lithologic variability can be minimized. Numerical formulations of landscape erosion based on discharge and slope do not contain an inherent length scale, so in principle they should apply to both small (i.e., sandbox) and large (i.e., continental) scales. Although physical experiments have been used for some time to study drainage-basin evolution (Parker, 1977; Phillips and Schumm, 1987; Schumm et al., 1987; Hancock, 1997), to date no physical model has been developed to monitor landscape change under constant forcing conditions for extensive erosional periods. Numerical results predict that a landform should attain a static geometry after eroding through a vertical distance approximately three times the total instantaneous elevation range (Howard, 1994). We have built a physical apparatus capable of monitoring landscape evolution over this length scale. We note that while eroding through this length may seem extraordinary, fission-track data from South Island, New Zealand, imply an average denudation of ~10 km in the past 10 m.y. (Tippett and Kamp, 1993). Local relief is ~3 km, so, assuming temporally steady relief, about three relief units have been eroded.

EXPERIMENTAL SETUP AND MONITORING

We constructed our experimental system to monitor drainage-basin behavior at steady rainfall and uplift rates. The main purpose of our experiment was to provide a physical test for numerical landscape evolution models. We have attempted to match the simplifying assumptions that go into the models: erosion is controlled by surface runoff, uplift rate, and substrate resistance to surface and body forces. In natural landscapes all of

these quantities vary spatially and temporally. We tried to remove complications associated with random variability, and thus to isolate erosional behavior that results from the elementary dynamics of the eroding system. A simple way to do this is to maintain a uniformly erodible substrate, and force the system at constant rates. We provided the model system with one outlet in the expectation that this would lead to a simply structured dendritic network. The experimental device consists of an oval tank ~1 m in diameter and 1 m deep with a single outlet dammed by a motor-controlled gate (Fig. A-1, p. 196). The motor operates continuously and drops the outlet at a slow, constant rate, in effect uniformly lifting the basin relative to base level. The height to width ratio of the tank permits relative uplift of three to six times the instantaneous drainage relief, defined as the maximum elevation above the outlet. A mister sprinkles rain (droplet size <200 μm) over the basin to generate runoff. The experimental basin forms third- to fifth-order drainage networks. Stream incision and transport dominate erosional processes in the experiment, but we also observe hillslope failures. For each experiment, well-sorted silica silt (median grain diameter $[D_{50}] = 45$ μm) is mixed with kaolinite (100:1 by weight) and water in a cement mixer, poured into the basin, and allowed to settle overnight. The settling process produces a flat surface pocked with small sediment volcanoes (<4 cm diameter) generated by groundwater overpressuring during loading. The initial runoff pattern on this surface is essentially random. Prior to the inception of uplift, rainfall is spatially calibrated by collecting rainfall in pans distributed over the basin. Rainfall is generated by a commercial radial mister. Oscillating fans above the mister break up persistent rainfall patterns, and produce a reasonably uniform rainfall distribution with a spatial variation ~12% (standard deviation/mean) for a measurement interval of 12 min. A run is initiated by starting the motor-controlled outlet and turning on rainfall. The run is terminated when the outlet reaches the bottom of the tank. In the meantime, we monitor landscape development with still photographs and time-lapse video (see attached CD-ROM), and measure sediment flux rates at the outlet of the basin by capturing basin effluent in a cylinder of known volume, and recording the weight and time required to fill the cylinder.

EXPERIMENTAL RESULTS

After a run is started, streams incise from the outlet and extend to the edges of the basin. Trunk streams near the outlet develop knickpoints that migrate upstream as waves, frequently triggering hillslope failures. A statistical balance between uplift and erosion is reached soon after complete dissection of the initial surface, as indicated by the sediment output measurements. Although we have done several runs that show comparable behavior, here we focus on one run, conditions for which are given in the Appendix. We sketched ridge crests on photographs for eight sequential times after complete dissection to monitor landform stability (Fig. A-2, a vertical photograph of the drainage basin nearing complete dissection of the initial flat surface, p. 197). We chose ridge crests because they should be the most stable feature in a landscape, and because they are easier to identify in photographs than streams. Figure A-3 (p. 198) is a plot of ridge crest location for two times, the first just after complete dissection, and the second after an additional 10 cm of erosion. Clearly, ridges have migrated, and several ridges (right side of Fig. A-3) cut across previous ridge locations at angles approaching perpendicular. This plot is for times just after complete dissection, and one might consider such ridge migration as an early adjustment in an approach to a stable form.

For a more comprehensive view, we collected all ridge location coordinates from eight photographs into a single grid (1 cm spacing), and ranked each cell in the grid according to the number of times a ridge occupied the cell (Fig. A-4, p. 199). Hence, the highest rank a cell could have is 8, and the lowest is 0. Darker regions delineate persistent ridge locations. Note that no cell is occupied continuously by a ridge. To place ridge migration into a scaled context, we define a length scale, the relief unit (H_r), as the range in elevation of the landform at complete dissection, in this case, 21 cm. The photographic sequence of Figure A-4 covers ~3 H_r of erosion. Figure A-5 (p. 200) shows that the fractional basin area continuously occupied by a ridge rapidly decreases beyond $1H_r$, and by 2 H_r is essentially zero. Note that the increase in fractional area containing a ridge at $H_r = 0.5$ indicates that total ridge length (a proxy for drainage density) varies temporally.

Stable ridge locations require a uniform erosion rate and similar slope conditions on both sides of the ridge. These conditions are rarely met in the experimental basins, for several reasons. The migration rate of knickpoints is not uniform through the network. Their passage frequently destabilizes a hillslope, inducing hillslope failure and slumping. The ridge crest moves away from the slumping region. Increased sediment discharge from slumping overloads streams locally, and incision rates decrease temporarily. This results in sediment flux oscillations and migration of divides. Lateral ridge migration can result in topographic inversion: stream locations become ridges, and vice versa. Geomorphic signatures of ridge migration within our physical experiment include strath terraces (stream eroded flattened sections above the valley floor), islands in trunk streams, and stream piracy. Apparently, these features do not require changes in climate or tectonic forcing, because these are kept constant in our experiment. This observation suggests that a possible autocyclic origin of these features must be borne in mind when using them to infer climatic or tectonic changes in natural settings.

An additional measure of temporal variation in erosion rates is sediment yield at the outlet. Sediment fluxes (Fig. A-6, p. 201) oscillate 15%–25% around the average erosion rate. One of the causes of variability in sediment output is knickpoint migration. Using time-lapse video, we counted at least 30 knickpoints generated over a vertical erosion distance of 60 cm, or roughly 3 H_r. This suggests that about 10 knickpoints formed per H_r. The initial height of the wave is ~5 mm (approximately the flow depth at the outlet), or 2%–3% of H_r, and 1%–10% of the local valley-ridge relief. Assuming that the eroding wave maintains a constant height, erosion from kinematic waves may account for as much as 30% of total erosion rate. Time-lapse video also revealed that while the knickpoints tend to propagate uniformly upstream, hillslope failures interfered with knickpoint propagation, at times drowning the knickpoint. We stress that knickpoint generation cannot be attributed to abrupt base-level drops, because the outlet drops continuously (Fig. A-6). The knickpoints appear to form spontaneously, and may be a result of instabilities in flow fields close to critical conditions (Parker and Izumi, 2000).

DISCUSSION

Our experimental results are quite different from the static behavior exhibited by numerical models. A possible source of the discrepancy could be residual random variability in rainfall and substrate resistance in our model. Temporal variability of rainfall in our basin was caused by water-pressure fluctuations in the laboratory. However, the time scale of ridge migration is much longer than that of rainfall fluctuations. There may also be minor variability in substrate resistance in the experiments, but it is difficult to see how this could directly cause systematic ridge migration. Do natural eroding drainage basins behave like our model? Our experiment does not incorporate vegetation, chemical weathering, or orographic effects. Furthermore, there are scale distortions between our model and natural systems. The ratio of basin size to grain size in the experiments, although large, is nonetheless much smaller than in most natural systems. Sediment concentration in experimental streams (set by uplift/rainfall rate and substrate density) approaches 25%. Such concentrations are not unprecedented, but are unusual in natural rivers. Feedback between local deposition and erosion may be enhanced at this concentration, and could be a source of instability within model streams. The experimental streams are laminar (maximum Reynolds number ~750), whereas natural mountain streams are always turbulent. We have observed local small standing waves in model flows, which suggest that flows can be supercritical (Froude number >1). Natural mountain streams are frequently supercritical. Individual mass flows (hillslope failures) in the experiments have length scales in the range of 10 cm2, so the ratio of event size to basin size is 0.0016. This ratio is plausible for small natural drainage basins but probably not for large ones. We do not think that any of these scale effects would cause qualitatively different behavior in the experimental system than in natural ones. Furthermore, because current landscape models are formally scale independent, we consider our experiments to be a valid test of them. An obvious next step is to develop a model capable of predicting the existence of dynamic steady-state landscapes. Such a model would presumably be capable of predicting changes in the dynamics as a function of scale and forcing rate, and so would provide a means of resolving the scaling question. Experimentally, a clear next step is to do experiments like the ones described here at

larger scales to test scale dependence of dynamic behavior. In the meantime, our experimental results suggest an alternative and much more dynamic view of the behavior of steady-state landscapes than that presented by the current suite of numerical models. The numerical models are clearly capable of capturing an average topographic form, but these models may not adequately represent the dynamic behavior of eroding landscapes.

APPENDIX

Model Run Parameters

Eroded distance: 80 cm
Rain rate (r): 6.5 μm/s
Uplift rate (u): 2.8 μm/s
Substrate density (ρ_b): 1.8 g/cm^3
Rainfall density (ρ_w): 0.998 g/cm^3
Grain size (D_{50}): 45 μm
Basin area: 6215 cm^2 Silt/clay (by weight): 100
Relief unit (H_r) (maximum relief): 21 cm
Maximum local valley-ridge relief: 8 cm
Maximum knickpoint height: ~0.5 cm
Average ridge density (total ridge length/basin area) (1/cm): ~0.16
Uplift/rainfall forcing ratio: 0.78 (u×ρ_b)/(r×ρ_w) (dimensionless)

REFERENCES CITED

Chase, C.G., 1992, Fluvial landsculpting and the fractal dimension of topography: Geomorphology, v. 5, p. 39–57.

Gilbert, G., 1877, Report on the geology of the Henry Mountains: U.S. Geographical and Geological Survey of the Rocky Mountain Interior Region: Washington, D.C., U.S. Government Printing Office, 160 p.

Glock, W., 1931, The development of drainage systems: A synoptic view: Geographical Review, v. 21, p. 475–482.

Hack, J., 1960, Interpretation of erosional topography in humid temperate region: American Journal of Science, v. 258-A, p. 80–97.

Hancock, G., 1997, Experimental testing of the Siberia landscape evolution model [Ph.D. thesis]: Newcastle, New South Wales, Australia, University of Newcastle, 467 p.

Howard, A.D., 1994, A detachment-limited model of drainage basin evolution:Water Resources Research, v. 30, p. 2261–2285.

Kramer, S., and Marder M., 1992, Evolution of river networks: Physical Review Letters, v. 68, p. 205–208.

Leheny, R., and Nagel S., 1993, Model for the evolution of river networks: Physical Review Letters, v. 71, p. 1470–1473.

Parker, G., and Izumi, N., 2000, Pure erosional cyclic and solitary steps created by flow over a cohesive bed: Journal of Fluid Mechanics (in press).

Parker, R.S., 1977, Experimental study of basin evolution and its hydrologic implications [Ph.D. thesis]: Fort Collins, Colorado State University, 331 p.

Phillips, L.F., and Schumm, S.A., 1987, Effect of regional slope on drainage networks: Geology, v. 15, p. 813–816.

Playfair, J., 1802, Illustrations of the Huttonian theory of the earth (reprint): Urbana, University of Illinois Press, 528 p.

Schumm, S.A, Mosley, M.P., and Weaver,W.E., 1987, Experimental fluvial geomorphology: New York, Wiley, 413 p.

Strahler, A.N., 1950, Equilibrium theory of erosional slopes approached by frequency distribution analysis; part 1: American Journal of Science, v. 248, p. 673–696.

Tippett, P., and Kamp, J., 1993, Fission track analysis of the late Cenozoic vertical kinematics of continental Pacific crust, South Island, New Zealand: Journal of Geophysical Research, v. 98, p. 16,119–16,148.

Tucker, G.E., and Bras, R.L., 1998, Hillslope processes, drainage density, and landscape morphology: Water Resources Research, v. 34, p. 2751–2764.

Willgoose,G., Bras, R., and Rodriguez-Iturbe, I., 1991, A coupled channel network growth and hillslope evolution model, Part 1, Theory: Water Resources Research, v. 27, p. 1671–1684.
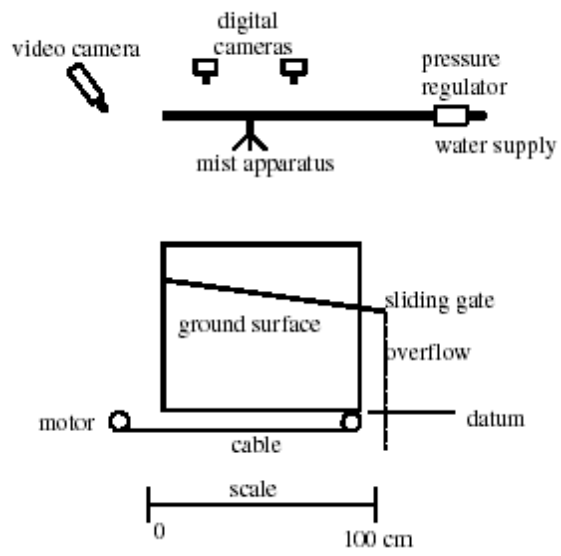
Figure A-1. Schematic cross section of erosional facility.

Figure A-2.Vertical photograph of drainage basin nearing complete dissection. Note that upper right corner retains remnants of initial flat surface. Basin is 87 cm wide, 98 cm long. Original digital photograph is 1280 × 960 pixels.
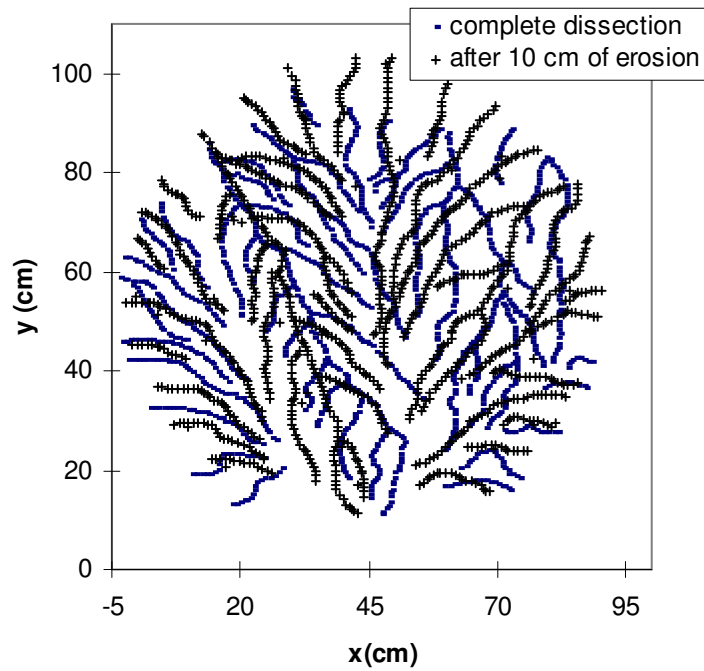
Figure A-3. Ridge networks for two sequential photographs. We sketched ridge segments on digital photographs (1280 × 960 pixels), extracted photographic coordinates of ridges, and projected coordinates to ground reference frame using three-dimensional projective coordinate equations. Eroded distance between photographs is 10 cm.
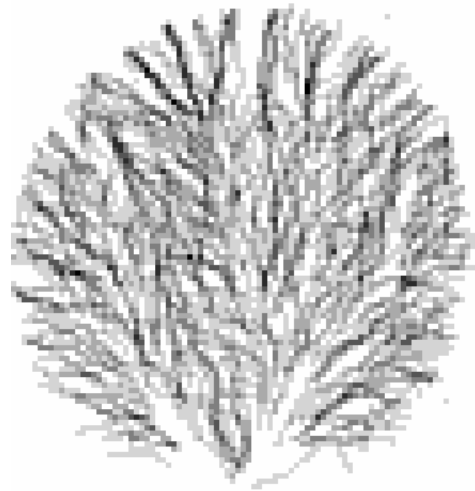
Figure A-4. Density plot of cell occupation by ridge. We counted number of times that 1 cm^2 cell was occupied by ridge in eight photographs after complete dissection, and plotted as gray scale. Dark regions have been more frequently occupied by ridge. Few ridges have maintained position, and these tend to occur at basin margins. Note that maximum value that cell can have is 8. No cells in plot have values exceeding 6. Basin width is 87 cm.
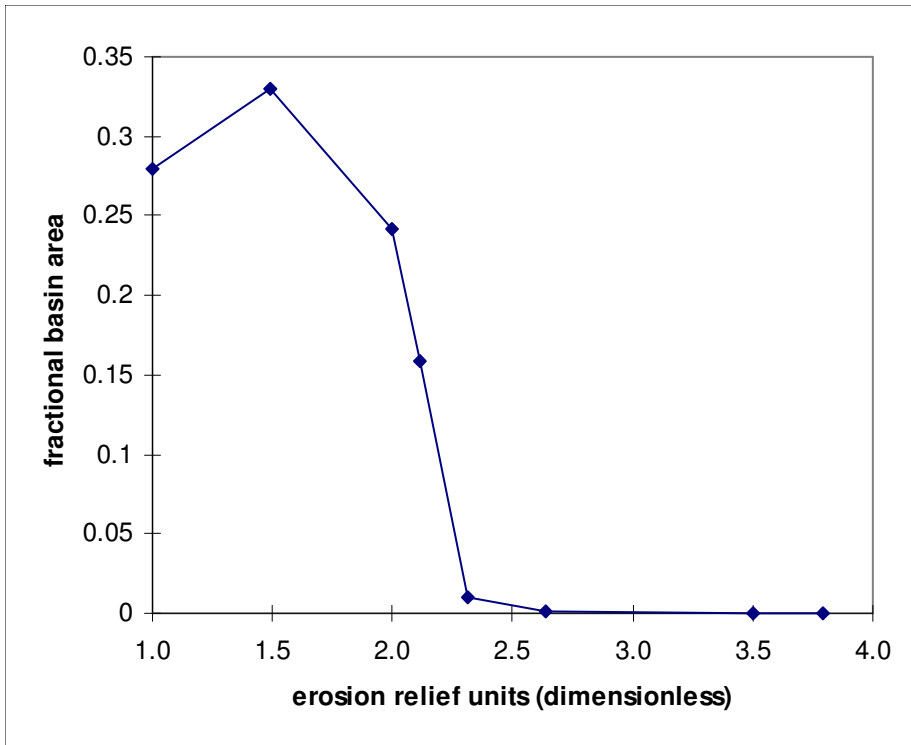
Figure A-5. Fraction of basin area occupied continuously by ridge. Eroded distance since complete dissection was normalized to Hr (Hr = eroded distance from initial flat surface to complete dissection). Note that by 2 Hr , no cell has been continuously occupied.
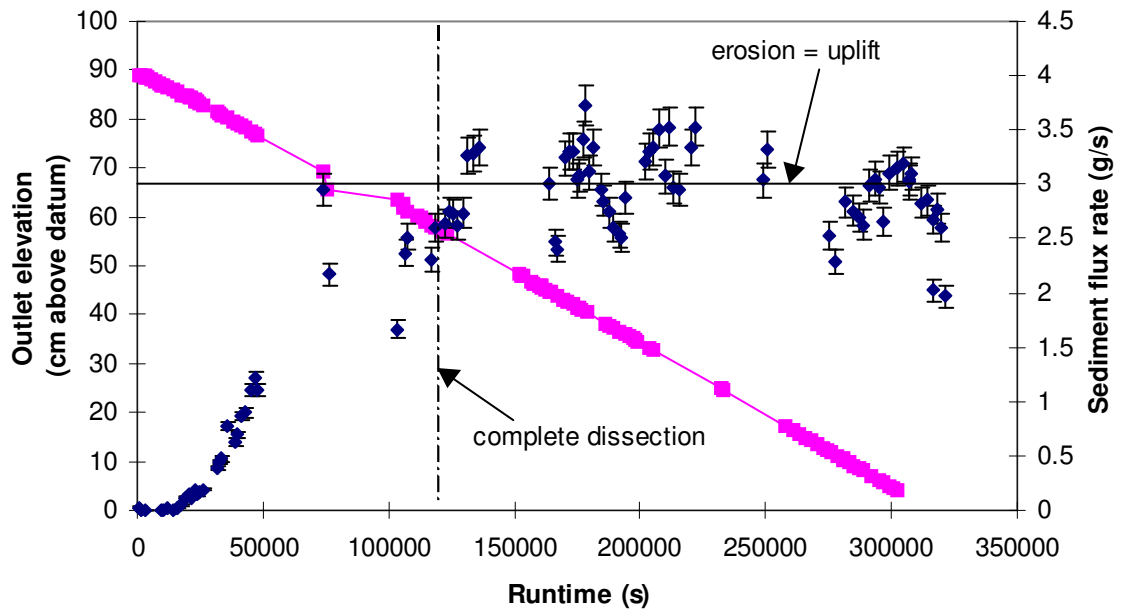
Figure A-6. Base-level curve and sediment flux at outlet. Measurements of bulk density were deconvolved into water and flux rates using mixing relation, density of water and sediment grains (quartz), and fill time. Measurement errors for volume are 1%; for mass, 0.5%; and for time, 5%. Error bars are plotted as 5% of calculated mass rate. Elevations of outlet were taken from fixed tape measure by outlet. Squares—outlet elevation; diamonds—sediment flux rate.

Appendix B

How Predictable is Local Erosion Rate in Eroding Landscapes?

Abstract

The current suite of numerical landscape models suggest that, under steady forcing, erosional landscapes evolve to a static steady state in which erosion everywhere balances uplift. Among other things, this implies that the only limitation on our ability to predict the future configuration of a landscape is imperfect knowledge of initial conditions and stochastic forcing events (e.g. storms, earthquakes). These are formidable obstacles to prediction, but they are apparently not the only ones. We have constructed a physical model of a drainage basin which erodes through several units of relief. We conducted several constantly forced runs at various base level fall and rainfall rates. The landscapes develop 3rd to 5th order stream networks, and erode by surface runoff, hillslope failures, and upstream migrating knickpoints. Within the constraints of an overall balance between uplift and erosion, interactions between streams and hillslopes result in spatially and temporally variable erosion rates. These results suggest that eroding drainage basins at steady forcing are intrinsically dynamic structures. Current numerical models do not exhibit the same level of erosional variability at steady forcing, suggesting that some feedback mechanisms may be missing from model formulations. The presence of inherent dynamism in eroding landscapes could seriously complicate predictions of local erosion rate, even if an average balance between uplift and erosion rate has been attained for a given drainage basin.

Introduction

The legacy of chaos theory is the recognition that there are systems that we may not be able to predict even with perfect knowledge of their governing equations. We approach prediction in a chaotic system differently than in a classical deterministic system. For a chaotic system, at least part of our effort must be aimed at predicting statistical properties of the system rather than exact sequences of events. Predicting statistical properties of a geomorphic system (e.g. mean and variance) is no less "rigorous" than predicting classical deterministic properties (e.g. wavelength), though it may require considerably more computational effort.

Before proceeding further, it is worth defining some terms. We follow convention and use *stochastic* to describe dynamics that for all practical purposes cannot be predicted exactly, i.e. that must be described probabilistically. *Random* behavior is a type of stochastic behavior in which the probability structure is very simple, e.g. white noise. Stochastic behavior in a system may be the result of stochastic forcing, in which

202

case we refer to it as *externally forced*, or it may arise spontaneously as a result of the system's internal dynamics, in which case we refer to it as *intrinsic*. The idea that a geomorphic system may show strongly unpredictable behavior with no external cause is well known in sedimentary geology, where it is associated with processes like avulsion and is known as *autocyclicity*. The use of 'cycle' in this context has historical roots and does not imply a well-defined repeat period. *Steady state* refers to a system that is balancing inputs (i.e., uplift) to and outputs (i.e., erosion) from the system. *Static steady state* implies uniform flux divergence at any scale (time or space), and no deviation from the average divergence exists. A static steady state system may or may not be forced at the boundaries of the system. *Dynamic steady state* implies non-zero forcing at the boundaries of the system, and global fluxes into and out of the system balance. The local fluxes, however, may exhibit deviations from the global average.

Erosional landscapes have been described in stochastic terms at least since the pioneering work of Shreve on random drainage networks [*Shreve*, 1975; *Shreve*, 1967]. Numerical landscape models [*Whipple* and *Tucker*, 1999; *Moglen* and *Bras*, 1995; *Howard*, 1994; *Beaumont* et al., 1992; and *Willgoose* et al., 1991] generate geometrically reasonable networks, and capture one important part of landscape unpredictability: sensitivity to initial conditions. One could not generally predict the final form of the landscape from a given initial topography, and slight changes in initial topography can produce quite different-looking landscapes. Nonetheless, as far as we are aware, stochastic dynamics in current landscape models are limited to the relation between initial conditions and final network configuration. None of these models produces ongoing, intrinsically generated stochastic dynamics. Forced with steady uplift and rainfall, and constant substrate conditions, these models evolve to a steady state that, while dependent in its details on the exact starting topography, is everywhere adjusted so that erosion rate locally balances uplift rate (static steady state). In this condition, the topography cannot continue to evolve.

It is difficult to know to what extent this is a good description of the behavior of natural landscapes. Landscape modelers are as aware as anyone else of dramatic, discrete erosional events (e.g. landslides, knickpoints) that suggest that erosion is discontinuous on short time scales. What is not known is the extent to which these events are just minor 'noise' about a condition that would be effectively static (given steady forcing) on the length and time scales for which the models are intended, or whether they portend a more fundamental instability that would prevent an eroding landscape from ever reaching the static condition that current models predict.

In order to address dynamics that might exist beyond event scale fluctuations, longer term measurements of landscape form are required, preferably over some time or length scale in which an average erosion rate is well-characterized. A simple and natural choice for this length scale might be drainage basin relief. The difficulty of investigating erosion dynamics at this scale is that the time required to erode through a significant portion of relief is quite long. For instance, a landscape eroding at 1 mm/yr with maximum relief of 1 km requires 100 kyr to erode through 1/10 of the relief. If we could observe erosion across the landscape on this time scale, what would it look like? Is the entire surface eroding at a uniform rate? If not,

what kinds of behavior are possible? Are erosion events distributed randomly in space and time? Or is erosion organized locally in some way?

Physically-based numerical models of eroding drainage basins offer a means of studying erosional behavior over longer time scales [*Whipple and Tucker*, 1999; *Moglen and Bras*, 1995; *Howard*, 1994; *Beaumont et al.*, 1992; *Willgoose et al.*, 1991]. A commonly employed erosion law is the shear stress or stream power law:

$$\partial z / \partial t = U - (b\, A^m\, S^n + c\, S) \tag{1}$$

where z is elevation, t is time, U is tectonic uplift rate, A is cumulative upstream area draining to an element, S is the local slope in the steepest downstream direction, b and c are constant coefficients related to the erosive potential of the process, and m and n are calibrated scaling parameters that incorporate erosivity (downstream width-depth-velocity scaling relations, shear stress and entrainment relations, and average climatic conditions) and erodibility (rock properties). Three dimensional landscape models are usually allowed to evolve from an initial random topography. Some evolution of the network occurs after a global balance of uplift and erosion has been attained. Howard [1994] notes that after eroding through 3 relief distances, the landscapes are stationary, and erode everywhere at the same rate (static steady state).

Interestingly, this erosion law has kinematic wave solutions to perturbations. An abrupt change in uplift rate, for instance, would propagate as a wave across the landscape [*Whipple and Tucker*, 1999]. While theory for erosional wave propagation across a numerical landscape exists, we point out that the mechanism of wave propagation is an external change in forcing. No existing model for drainage basin erosion spontaneously generates knickpoints in the absence of changes in forcing conditions. At steady forcing, stability of the landscape is inevitable in current numerical models.

Reported erosion rates in natural drainage basins show substantial spatial variability. Average hillslope erosion rates in the Oregon coast ranges vary ~50%, with a range three to four times the minimum erosion rate [*Reneau and Dietrich*, 1991]. Erosion rates vary by a factor of 10 over a small drainage basin in northeastern California, USA [*Granger et al.*, 1996]. Deep-seated landsliding accounts for a large fraction of hillslope erosion in the Southern Alps of New Zealand for short time scales (tens of years) [*Hovius et al.*, 1997], and in Taiwan [*Hovius et al.*, 2000]. Power law distributions for shallow landslides have been reported for Queen Charlotte Islands, Canada [*Martin et al.*, 2002, in press]. A power law relation between landslide magnitude and frequency implies large spatial and temporal variations in erosion rate. Erosion rates derived from cosmogenic nuclides for small catchments in the Sierra Nevada of California exhibit order of magnitude ranges [*Riebe et al.*, 2000]. Spatial erosion rates during the Holocene for several small (<100 km^2) drainage basins in Nevada, USA exhibit comparable variability [*Miller et al.*, 2001]. These field studies all point to substantial variability in erosion rates. Is this due to external effects, such as variability in climate, tectonics, or lithology, or could it be due to intrinsic interactions between hillslopes and streams?

Long-term system behavior in natural eroding landscapes remains somewhat hypothetical. Significant progress has been made toward obtaining surface exposure ages and erosion rates on a land surface using

cosmogenic nuclide concentrations [*Heimsath et al*., 1999; *Granger et al*., 1996; *Brown et al*., 1995; *Bierman*, 1992; *Lal*, 1991] , and low temperature geochronometry is yielding exhumation rates [e.g., *Armstrong et al*., 2000; *Brandon et al*., 1998], but we know of no study that has detailed surface ages and erosion rates in an eroding drainage basin at a resolution required to make statements concerning long term patterns of erosion. Natural landscapes are also subject to significant fluctuations in climatic, tectonic, and base level conditions that further complicate study of dynamic systematic behavior in an eroding drainage basin.

An alternative means of investigating landscape evolution has been the use of small-scale erosion facilities [*Davy et al*., 2000; *Hasbargen and Paola*, 2000; *Hancock*, 1997; *Czirok et al*., 1993; *Parker*, 1977]. Small scale physical experiments allow manipulation of boundary conditions, and hence allow for a range of conditions to be explored, such as changes in landscape form due to rainfall rate [*Hancock*, 1997; *Parker*, 1977], or the effect of initial surface slope on network development [*Phillips and Schumm*, 1987]. Further, measurements of landscape form and mass fluxes across system boundaries can be used to test numerical model predictions. There are limitations to physical experiments, in that some forces become important in the total force balance at small scales, such as water surface tension and molecular viscosity, that are not representative of anything at a larger scale, and may not be well-represented in a numerical model either. Physical experiments offer, however, a view into the dynamics of drainage basins eroded by surface runoff and slope failures, and thus may offer insight into longer term evolution of larger drainage basins that erode with similar processes.

We designed an experiment to investigate the systematic erosional behavior of a drainage basin at steady forcing. Our experiment is a simplified model of an eroding drainage basin experiencing constant, uniform rainfall and uplift rates, and a homogeneous substrate. We have eliminated vegetation and chemical weathering, and minimized substrate, rainfall, and uplift variability in an effort to isolate basic physical processes of surface runoff, incision, and mass transport within the framework of a dendritic (i.e., convergent flow) drainage basin. The goal of these experiments is to test the idea that drainage basins erode at spatially uniform rates under constant forcing conditions, and ultimately to understand the kinds of behavior that are possible within an eroding drainage basin.

Experimental Design And Run Conditions

Our experimental drainage basin is an elliptical tank, with a surface area of 6477 cm^2 (99 cm long and 87 cm wide), and depth of 100 cm. A motor-controlled sliding gate (1 cm wide) functions as the outlet to the basin (Figure B-1, p. 223). A radial mist apparatus located 1.5 m above the tank generates rainfall. Oscillating 23 cm fans situated 2 m above the tank are used to break up stable air circulation patterns and promote mixing of rainfall in the facility. The tank was constructed from sheet metal, and rests on a plywood base supported by concrete blocks. An electric variable speed motor allows us to drop the outlet at rates from 0.5 to 50 μm/s. During the course of each run, outlet elevation above datum was measured on a fixed mm scale tape. Base level curves were constructed from these measurements, and base level fall rates

were derived from the regression coefficient of elevation against time. We note that this configuration (a dropping base level) is equivalent to spatially uniform uplift across the basin (block uplift).

The substrate consists of kaolinite and silica flour (D_{50} = 45 µm) mixed in a cement mixer (1:100 clay/silt), with water added until the mix is capable of flowing. We then poured the mix into the basin, and allowed it to settle overnight. Settling produces a standing body of water, which upon draining reveals a flat surface pocked with small mud volcanoes (< 2 cm in diameter).

Rainfall spatial patterns were measured by collecting rain in pans scattered over the basin prior to each run. The coefficient of variation of rainfall for short time intervals (5-10 minutes) is ~15%, and decreases to ~5% for measurement intervals longer than 30 minutes. Total water discharge (runoff) was measured at the outlet during each run, and provides an additional measure of temporal rainfall variation. This measure includes runoff from rainfall as well as groundwater contained in the substrate. The coefficient of variation for total runoff ranges from 1.8% for Run 6 to 12.5% for Run 3.

We have conducted five runs at various uplift and rainfall rates (held constant during each run) that eroded through several relief units (see Table A-1 for run conditions, p. 221). We define a relief unit (H_r) as the maximum relief at complete dissection of the initial flat surface. After complete dissection, the run continues until the outlet has reached the bottom of the tank. One run (Run 1) was turned off overnight, and the surface dried out. The response time to balance uplift and erosion during rehydration for Run 1 was ~ 1 H_r, or ~0.04 H_r of erosion. Run 1 eroded through ~1.5 H_r. We noted that the landscape was still evolving at the end of the run, so we added 20 cm to the tank walls for subsequent runs to allow the landscape to erode for a longer time at dynamic steady state conditions. The remaining runs were conducted continuously, with minor interruptions in base level fall and rainfall for photographs.

We organize our runs according to the ratio of rainfall/uplift mass rates (r/u), i.e., rainfall rate (L/T) divided by uplift rate (L/T) multiplied by their respective densities. In essence, r/u is the average vertical mass flux of rainfall over a unit area, divided by the vertical mass flux of substrate per unit area due to uplift. This nondimensional number can be thought of as a water to rock ratio, or qualitatively as a measure of forcing conditions that range from dry uplift to wet uplift, or more simply as dilute (high r/u) or concentrated (low r/u) erosion conditions. For runs presented in this paper, r/u varies from 0.6 to 8.2. We hypothesize that for a given substrate at steady forcing, the topographic form is set by surface shear stress (runoff) and substrate resistance to gravitational forces (hillslope failures). At high r/u, surface runoff is sufficient to remove all of the material supplied by uplift. A higher drainage density results, and hillslope failures decrease in size. At low r/u, slopes develop that enhance hillslope failures, resulting in a larger range of hillslope failure size.

Measurement Methodology

Our data collection was initially guided by the concept that a landscape develops a static form at constant forcing conditions. In order to test this idea, we developed methods to measure topography and

monitor planform changes, as well as collect detailed records of sediment and water leaving the erosion facility.

In order to address overall planform stability of drainage basin features, we used a VHS video camcorder modified for time-lapse image collection. An automated shutoff valve was inserted into the rainfall water line for runs 3, 4, and 6, to allow for clearer images for time-lapse video. Shutoff times varied for the runs, in the range of 5-10 s in duration every 250 to 500 s. Time lapse video capture rates varied from 2 s of video (30 frames/s) every 250 s to 1 s every 500 s. We later subsampled the videotape, and transferred the record to digital format for viewing on a computer. Time-lapse records allow us to compress time, and reveal process interactions at longer time scales not readily accessible at real time conditions, such as interactions between hillslope failures and knickpoint propagation. Longer term divide migration is also more readily detectable. Digitized video of the runs can be viewed online at http://www.geo.umn.edu/orgs/ seds/les/.

For detailed measurements of landscape form, we used stereo digital photographs to develop gridded elevation models of the landform. The process involves several steps. Photographic coordinates of measured benchmarks on the basin were used to orient the images in the ground reference frame. Correlated features (pixels) were automatically extracted from stereo pairs. Given known image orientations, elevations can be derived from solutions to collinearity equations for correlated points [*Wolf*, 1983]. The precision of photogrammetric solutions using a 1280 x 960 pixel resolution camera is modest. Elevation changes calculated for single pixel shifts range from 7 to 20 mm, depending on the distance between the ground surface and camera, and the field of view. However, a fair amount of detail can be discriminated from the elevation fields derived from this method (Figure B-2, p. 224).

Typically, 30,000 to 40,000 correlated points are collected from each stereo pair of photographs. After computing ground coordinates from correlated photographic points, the ground coordinates are read into a grid at 7 mm spacing (there are 12,757 grid points in a 7 mm grid with boundaries coincident with the erosion facility walls). We then filter the grid for extreme slopes (>250%), and average the grid with three passes of a moving window (3x3 pixels). We performed this set of operations on all of the grids. Filtering extreme slopes removes faulty correlations introduced by automated image correlation. Smoothing removes stepped increments in elevation due to the resolution of the digital images (1280x960 pixels).

Observations And Measurements

At the beginning of each run, streams incise headward from the outlet into the initial flat surface. Measurements of sediment flux at the outlet indicate that erosion balances uplift roughly at the time of complete dissection of the initial surface. Sediment flux varies modestly after complete dissection, with a coefficient of variation ranging from ~15% for run 3 to ~7% for run 1. The dominant erosive process is surface runoff that self-organizes into a dendritic stream network. The landscape is forced with continuous uplift and hence is predominantly erosional. However, we note there are always some valleys with temporary sediment storage. This is true for all of the runs we have conducted. Knickpoint (an

oversteepened section in a stream) generation and migration are common in all of the runs. Knickpoints propagate upstream through the network, and have the appearance of waves, wrapping around and lapping against ridges, and re-excavating valleys with stored sediment. Knickpoint propagation experiences significant interference from hillslope failures in lower *r/u* runs, and incised stream reaches are frequently overwhelmed with sediment, temporarily halting the advance of the knickpoint. While surface runoff performs the bulk of the work in eroding and transporting sediment out of the system, knickpoints clearly assist in excavation of stored sediment and incision into the substrate.

We also observe areas of very low relief, strongly resembling terraces, bounded by incising streams. The areas tend to be rather small, on the order of 10-50 cm2, and somewhat lenticular in plan view. Over time these areas can grow into well-defined ridges, though frequently they are annihilated by migrating stream channels.

As noted above, we used time series of stereophotographs to derive elevation data sets for each run. The number of data sets varies between runs from 3 for Run 3 to 32 for Run 6 (see Table B-1). We computed the distribution of elevation and slope, average and standard deviation of elevation as a function of distance from the outlet, and the exponent and intercept for the slope-area relation for each data set. Average values of maximum relief, local slope, and regional slope are plotted graphically against *r/u* in Figure B-3 (p. 225), and demonstrate that these measures vary systematically with forcing conditions. Time-averaged values for area-slope parameters are given in Table B-2 (p. 221). Coefficients of variation (derived from the range in average values in all data sets after complete dissection) for these values are listed in Table B-3 (p. 222). Note that we did not compute variances for area-slope parameters. Average values of relief and slope vary less than 10% for each run at steady state conditions, indicating that a stable statistical form develops in our experimental landscapes.

Temporal Measures Of Dynamism

We now show that within a statistically stable form at steady forcing, temporal and spatial erosion rates vary substantially. We calculate local erosion rates by differencing gridded elevation data sets on a cell by cell basis, and dividing by the time separation between the data sets. The result is a spatial pattern of erosion rate between the two data sets (Figure B-4, p. 226). We performed this operation for all possible grid pairs for Runs 1,2,4, and 6.

To assess the spatial variance of erosion rate, we calculate the mean (μ) and standard deviation (σ) of erosion rate for each pair of grids. We then plot the coefficient of variation (σ/μ) against the time separation between the grids. We perform this set of operations for all possible pairs of grids for each run. We did not perform this calculation for run 3, due to the limited number (three) of gridded data sets. If the landform were eroding at a spatially uniform rate, the coefficient of variation would be zero. If the time separation between grids is very long, such that the average vertical distance between grids is large relative to the local relief, the coefficient of variation again approaches a value of zero. Short and intermediate time scales for

steadily forced landforms offer a means of discriminating between spatially uniform or spatially nonuniform erosion.

In order to eliminate scale dependence of time in our experiment (we measured time in seconds), we multiplied time by uplift rate, which yields a distance h, and divided h by the relief at dissection (H_r). This yields a nondimensional temporal measure in units of fractional relief. We plot the coefficient of variation of erosion rate against fractional relief for runs 1,2,4, and 6 (Figure B-5, p. 227). A power law relationship exists between the variance of erosion rate and vertical eroded distance, with a characteristic exponent about -2/3. Data from different runs plot on the same trend, implying that erosional variability is not sensitive to forcing conditions in our experiments. We attribute erosional variability to knickpoint migration, hillslope failures, and ridge migration. For comparison, we plot the typical erosion rate variability of an evolving stream power based gridded numerical model (simplified after *Howard*, 1994) after a balance between uplift and erosion rate has been attained. Numerical erosional variability is roughly an order of magnitude lower than for experimental landforms. Note that ultimately the variability goes to nil for all numerical models at steady forcing.

Changes in local flow direction offer another measure of landscape stability. We first calculate the flow direction vector in the steepest descent direction on a cell by cell basis for a gridded data set. We then compute the change in flow direction on a cell by cell basis by taking the dot product of the flow direction vectors between two grids. The dot product (that is, $\cos(\alpha)$, where α is the angle between vectors) returns values between -1 (flow in opposite direction) and 1 (flow in the same direction). Summing the individual dot products, and dividing by the number of cells in the grid yields an average flow direction change. If a surface is eroding at a spatially uniform rate, we expect the relation to be a flat line with a flow direction change value of 1, i.e., no change in flow directions with time. If the landscape experiences variable spatial erosion, directional changes plot as a curve. We plot average flow direction change for all possible time separations after complete dissection (Figure B-6, p. 228). Note we again convert time into fractions of H_r. The data show that the change in flow direction asymptotically approaches unity as eroded relief approaches nil, and flattens to a constant average change at longer times. At higher r/u conditions, experimental landscapes develop smaller sub-basins (higher drainage density), hence a wider distribution of flow directions are possible. This results in a larger possible average flow direction change at longer times (see $r/u = 8.2$, Figure B-6, p. 228). Average flow direction change varies between runs, suggesting dependence on forcing conditions and process activity (such as frequency and size of hillslope failures).

Discussion

Stochastic erosional variability in natural landscapes could result either from stochastic forcing or intrinsic, self-organized variation. These are hard to separate in natural settings because atmospheric and tectonic forcing are highly variable. The experiments we report here illustrate intrinsic ("autocyclic") erosional variability at steady forcing. In an average sense, these experimental landscapes are 'adjusted' to forcing from climate and uplift, as reflected by a characteristic relief and slope for each set of uplift and

rainfall conditions that we impose. We note, however, from time-lapse video and animation of time series elevation data that ridges and valleys are mobile features. Such mobility requires erosional variability. Our experimental landscapes are clearly not eroding at spatially uniform rates.

What is the source of such variability? We have tried to minimize external variability by maintaining constant rainfall and uplift rates, and using a homogeneous substrate. As with any physical experiment, perfect uniformity is not possible. We observed short-term fluctuations in rainfall, on the order of 10-100 s duration, due to pressure variations in the laboratory water supply. Minor stick-slip sliding of the outlet also occurred (<1mm/slip). We mixed the substrate thoroughly in a cement mixer, but small-scale heterogeneity in clay concentration in the substrate is possible. We do not think that minor fluctuations in any of these quantities can explain the temporal changes we observe in our experiment. For instance, Run 1 dried out overnight. The coefficients of variation for slope and relief are no larger than those for other runs that were conducted continuously, suggesting that dry-out (3 dry-out events over 1.5 H_r, in this case) does not significantly alter long-term behavior and form.

The gradual change in flow direction over time suggests that lateral migration of topography occurs over time scales much longer than perturbations from rainfall and uplift. Time series animation of elevation shows that small ridge spurs (and even some longer ridge segments) are mobile over time scales of the order 0.1 H_r/u. Migrating knickpoints are a common feature in all of the runs we have conducted. Our landscapes always store some sediment in valleys. The presence of temporary sediment storage implies that our experimental trunk streams are at or near carrying capacity, and cannot both incise and transport sediment on the slopes they develop. Knickpoints are the assistance mechanism to locally steepen channel slopes, and allow streams to both transport and incise. Knickpoints also interact with hillslope failures, especially in low r/u conditions. Interactions work both ways, i.e., a migrating knickpoint can destabilize a hillslope, and a hillslope failure can bury a channel. For higher r/u, hillslope failures decrease in size and frequency, and knickpoints propagate as a wave away from the stream and up to the ridge crest, frequently generating some wobble in ridge crest location as waves reach the crest from opposite sides of the ridge slightly out of phase.

Our experiments aim at the behavior of eroding drainage basins at dynamic steady state. We already know that erosion in natural landscapes can be highly localized spatially and temporally. This is also true in our experiments. But with the added perspective of seeing the model landscape evolve through several relief distances (H_r), we find that this short-term variability is not just minor noise on an essentially static topographic pattern. Rather, short-term variability cascades up in scale, through a set of feedbacks we have not fully identified, to induce variability in the basic ridge and valley structure of the landscape itself. The general landform characters of local and regional slope develop and fluctuate within modest limits. Within this general framework, the system behaves somewhat loosely. Ridges and valleys can migrate, extend, shorten, or be annihilated. Spatially uniform erosion displays itself only over longer time periods, on the order of the time required to erode through a relief of topography.

These results for a small steadily forced erosional drainage basin raise the possibility that natural eroding drainage basins may show strong intrinsic stochastic dynamics. Current numerical models of landscape evolution do not exhibit the same level of variability. We think that numerical models are missing some key feedback elements. Possible sources of destabilizing feedback could include sediment concentration in streams and stream incision [*Sklar and Dietrich*, 1998]; local erosion and deposition of sediment for streams at transport capacity; and the destabilizing influence of knickpoint propagation on adjacent hillslopes. For natural landscapes, vegetation might play a role by increasing resistance to erosion, hence steepening hillslopes. Episodic changes in vegetation, perhaps due to drought or fire, might force fluctuations in erosional resistance and increase the scale of 'erosive events' over longer times, particularly for uplifting landscapes.

Conclusions

Spatial erosion rates for our experiments are strongly dependent on the time scale of observation. Erosion rate variability increases at shorter observation times, and can be characterized by a power law relation with an exponent ~-2/3. The exponent in the relation does not appear to be sensitive to forcing conditions. Steady state erosion rate variations on the order of ~50% of the average erosion rate are still common after eroding through ~0.1 H_r. Temporal flow direction changes indicate a significant amount of lateral migration in experimental landscapes. Changes in flow direction exhibit greater variability at higher *r/u* forcing conditions. Both of these measures indicate that spatial variability in erosion persists long after a balance between uplift and erosion has been established. We attribute variability to both small scale erosive events, such as hillslope failures and knickpoint migration, and larger scale landscape instability, such as ridge growth, migration, and annihilation.

The possibility of continuous, internally generated landscape instability raises interesting new questions about the idea of optimality in drainage networks [*Rigon et al*., 1993; *Rinaldo et al*., 1992]. If a network is constantly reconfiguring itself, can it be said to be 'optimal'? If not, does it vary about a state that is near optimal? More generally, how close are the mean properties of an ever-changing (but statistically stable) landscape to those predicted by any of the present numerical landscape models?

If natural drainage basins are capable of feedback such as we observe in our physical experiment, then prediction of erosion in landscapes may be comparable in difficulty to predicting more classical chaotic systems such as earthquakes or weather. However, if erosional variability is spatially organized in some way, (for instance, near knickpoints or migrating drainage divides), then as a first step we should be able to identify the most active regions in the basin based on knickpoint location, breaks in slope in hillslope profiles, or perhaps asymmetric ridges.

quality of this paper. This work has been partially supported by GSA grant #6048-97, and by a summer research grant from the Dept. of Geology and Geophysics, University of Minnesota.

References

Armstrong, P. A., T. A. Ehlers, P. J. J. Kamp, K. A. Farley, and D. S. Chapman, Tracking changes in exhumation rates using low-temperature thermochronometry: an example from the Wasatch mountains, Utah (USA), in 9th *International conference on fission track dating and thermochronology*, edited by W.P. Noble, P.B. O'Sullivan, and R. W. Brown, Geol. Soc. Austral. Abstr., 58, 355-356, Lorne, 2000.

Bierman, P. R., Use of in situ-produced cosmogenic isotopes to determine rates of geomorphic processes, Snowbird, Utah: AGU, *Chapman Conf. Tectonics and Topography*, 34, 1992.

Beaumont, C., P. Fullsack, P., and J. Hamilton, Erosional control of active compressional orogens, in *Thrust Tectonics*, ed. McClay K. R., Chapman and Hall, 1-18, 1992.

Brandon, M. T., M. K. Roden-Tice, and G. I. Garver, Late Cenozoic exhumation of the Cascadia accretionary wedge in the Olympic mountains, northwest Washington State, *Geol. Soc. Am. Bull.*, 110, 985-1009, 1998.

Brown, E. T., R. F. Stallard, M. C. Larsen, G. M. Raisbeck, and F. Yiou, Denudation rates determined from the accumulation of in situ-produced 10Be in the Luquillo Experimental Forest, Puerto Rico. *Earth and Planetary Science Letters*, 129, 193-202, 1995.

Czirok, A., E. Somfai,, and T. Vicsek, Experimental evidence for self-affine roughening in a micromodel of geomorphological evolution, *Physical Review Letters*, 71, 2154-2157, 1993.

Davy, P., D. Lague, J. Kermarrec, D. Sokoutis, L. Bodet, and R. Compagnon, Analogue modelling of relief dynamics, *Physics and Chemistry of the Earth (A)*, 25 (6-7), 549-553, 2000.

Granger, D. E., J. W. Kirchner, and R. Finkel, Spatially averaged long-term erosion rates measured from in situ-produced cosmogenic nuclides in alluvial sediment, *J. Geol.*, 104, 249-257, 1996.

Hancock, G., Experimental testing of the Siberia landscape evolution model. Ph.D. thesis, Univ. of Newcastle, New South Wales, Australia, 1997.

Hasbargen, L. E., and C. Paola, Landscape instability in an experimental drainage basin, *Geology*, 28, 1067-1070, 2000.

Heimsath, A. M., W. E. Dietrich, K. Nishiizumi, and R. C. Finkel, Cosmogenic nuclides, topography, and the spatial variation of soil depth, *Geomorphology*, v. 27, p. 151-172, 1999.

Hovius, N., C. P. Stark, and P. A. Allen, Sediment flux from a mountain belt derived by landslide mapping, *Geology*, 25, 231-234, 1997.

Hovius, N., C. P. Stark, H. Chu, and J. Lin, Supply and removal of sediment in a landslide-dominated mountain belt; Central Range, Taiwan, *J. Geol*., 1081, 73-89, 2000.

Howard, A. D., A detachment-limited model of drainage basin evolution, *Water Resour. Res*., 30, 2261-2285, 1994.

Lal, D., Cosmic ray labeling of erosion surfaces: in situ nuclide production rates and erosion models, *Earth Planet. Sci. Lett*., 104, 424-439, 1991.

Martin, Y., K. Rood, , J. W. Schwab, and M. Church, Sediment transfer by shallow landsliding in the Queen Charlotte Islands, British Columbia, Can. Journ. Earth Sci., v. 39, no. 2, 189-205, 2002.

Miller, J., D. Germanoski, K. Waltman, R. Tausch, and J. Chambers, Influence of late Holocene hillslope processes and landforms on modern channel dynamics in upland watersheds of central Nevada, *Geomorphology*, 38, 373–39, 2001.

Moglen, G. E., and R. L. Bras, The importance of spatially heterogeneous erosivity and the cumulative area distribution within a basin evolution model, *Geomorphology*, 12, p. 173-185, 1995.

Parker, R. S., Experimental study of basin evolution and its hydrologic implications. Ph.D. thesis, Colorado State Univ., Fort Collins, 1977.

Phillips, L. F., and S. A. Schumm, Effect of regional slope on drainage networks, *Geology*, 15, 813-816, 1987.

Reneau, S., and W. Dietrich, Erosion rates in the southern Oregon Coast Range: Evidence for an equilibrium between hillslope erosion and sediment yield, *Earth Surf. Processes Landforms*, 16, 307-322, 1991.

Riebe, Clifford S., J. W. Kirchner, D. E. Granger, Robert C. Finkel, Erosional equilibrium and disequilibrium in the Sierra Nevada, inferred from cosmogenic 26Al and 10Be in alluvial sediment *Geology*, 28, 803–806, 2000.

Rigon, R., A. Rinaldo, I. Rodriguez-Iturbe, R. Bras, and E. Ijjasz-Vasquez, Optimal channel networks: a framework for the study of river basin morphology, *Water Resour. Res*., 29, 1635-1646, 1993.

Rinaldo, A., I. Rodriguez-Iturbe, R. Rigon, R. Bras, E. Ijjasz-Vasquez, A. Marani, Minimum energy and fractal structures of drainage networks, *Water Resour. Res*, 28, 2183-2195, 1992.

Shreve, R. L., The probabilistic-topologic approach to drainage-basin geomorphology, *Geology*, 3, 527-529, 1975.

Shreve, R. L., Infinite topologically random channel networks, *J. Geol*, 75, 178-186, 1967.

Sklar, L., and W. Dietrich, River longitudinal profiles and bedrock incision models: Stream power and the influence of sediment supply, in *Rivers over rock: Fluvial Processes in Bedrock Channels*, *Geophys. Monogr. Ser.*, vol. 107, edited by K. J. Tinkler and E. E. Wohl, pp. 237-260, AGU, Washington D. C., 1998.

Whipple, K. X., and G. E. Tucker, Dynamics of the stream-power river incision model: Implications for height limits of mountain ranges, landscape response timescales, and research needs, *J. Geophys. Res.*, 104, 17,661-17,674, 1999.

Willgoose, G., R. Bras, and I. Rodriguez-Iturbe, A coupled channel network growth and hillslope evolution model, 1. Theory, *Water Resour. Res*, 27, 1671-1684, 1991.

Wolf, P. R., *Elements of Photogrammetry*, Second Edition, McGraw-Hill Book Company, 1983.

_____

Leslie E. Hasbargen, Department of Geology and Geophysics, 310 Pillsbury Drive SE, University of Minnesota, Minneapolis, MN 55455. (hasba002@tc.umn.edu)

Chris Paola, Department of Geology and Geophysics, 310 Pillsbury Drive SE, University of Minnesota, Minneapolis, MN 55455. (cpaola@umn.edu)

Table B-2 Experimental run conditions

run id	# of data sets	uplift rate (μm/s)	rainfall rate (μm/s)	water/ rock $(r/u)^a$	basin depth (cm)	grain size (D_{50}) $(\mu m)^b$	clay: silt wt%	substrate density (g/cm^3)
1	10	2.16	3.8	1.0	43.8	40	1	1.7
2	10	2.82	3.86	0.8	84.8	40	1	1.7
3	3	6.02	6.1	0.6	82.9	40	1	1.7
4	11	0.55	6.2	6.4	88.1	40	1	1.7
6	32	0.94	13.5	8.2	88.8	40	1	1.7

[a] Mass forcing rate (velocity *density) ratio: $(r\,\rho_w) / (u\,\rho_s)$, where ρ_w is rain density, and is ρ_s substrate density.

[b] Analyses generously provided by John Pitlick, U. of Colorado, Boulder. Analyses performed with a Malvern long bed laser particle size analyzer.

Table B-2 Relief and slope statistics after complete dissection.

	run 3	run 2	run 1	run 4	run 6
water/ rock (r/u)	0.6	0.8	1.0	6.4	8.2
maximum relief (cm)	25.2	24.2	23.1	17.6	15.8
local slope	0.43	0.43	0.44	0.37	0.28
regional slope	0.26	0.23	0.22	0.17	0.16
area-slope exponent	-0.13	-0.14	-0.16	-0.15	-0.13
area-slope intercept	0.46	0.45	0.48	0.34	0.26

Table B-3 Coefficient of variation (σ/μ) for relief and slope.

	run 3	run 2	run 1	run 4	run 6
water/ rock (*r/u*)	0.6	0.8	1.0	6.4	8.2
maximum relief (cm)	0.047	0.073	0.064	0.087	0.083
local slope	0.072	0.064	0.110	0.134	0.088
regional slope	0.063	0.078	0.055	0.060	0.107
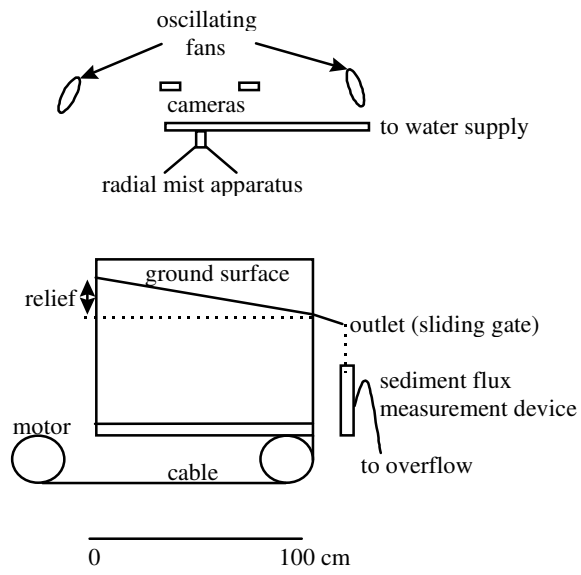
Figure B-1. Schematic cross section of erosion facility.
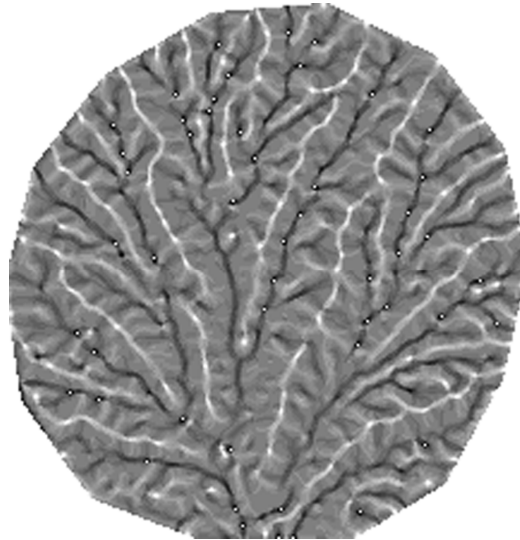
Figure B-2. Local relative height map for Run 4 (runoff-dominated erosion, *r/u* = 6.4). Width of image is 87 cm, maximum relief is 16.7 cm, grid spacing is 4 mm. Local relative height is the number of cells in a gliding box (5x5 pixels) lower than the center cell in the box, divided by the total number of cells in the box. Relative height values range from 0 (local depressions) to 1 (local peaks).
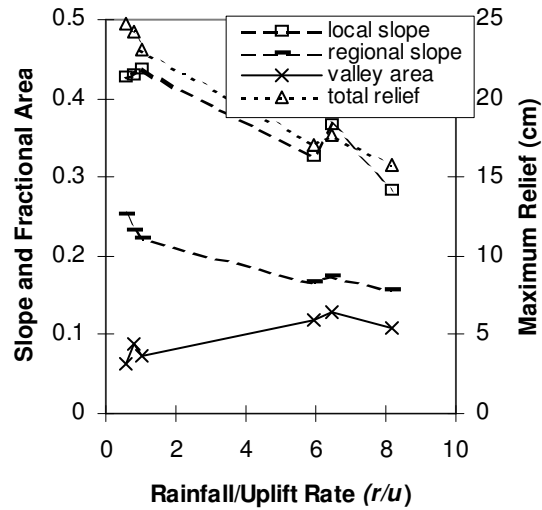
Figure B-3. Average topographic measures plotted against forcing conditions. Local slope is the average steepest descent slope. Regional slope is the average regression coefficient derived from plots elevation against distance from the outlet. Total relief is the average maximum range in elevation. Valley area is the fractional area of the basin occupied by cells with local relative height values <0.375 in a moving 5 x 5 pixel window (recall local relative height ranks a cell from 0 (depression) to 1 (peak)). Ranges in values (1 σ) for a given run are <10%. Note slope and relief closely track each other. Valley area increases slightly with *r/u*, suggesting stream networks advance into smaller areas at higher *r/u* conditions.
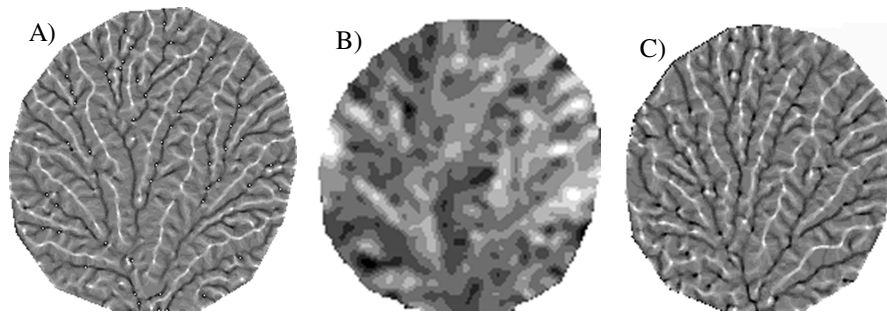
Figure B-4. Spatial erosion rates for two grids separated vertically by 7 cm for Run 4 ($r/u = 6.2$). A) Local relative height for the first grid of the differenced pair. B) Gray scaled plot of spatial erosion rates. White represents a high erosion rate (0.81 μm/s), black is low (0.42 μm/s), with an average erosion rate of 0.62 μm/s. C) Local relative height for the second grid of the pair. Maximum elevation range for each grid is 17.5 cm (a) and 15.4 cm (c). Width of each image is 87 cm. Spatial resolution is 7 mm/pixel.
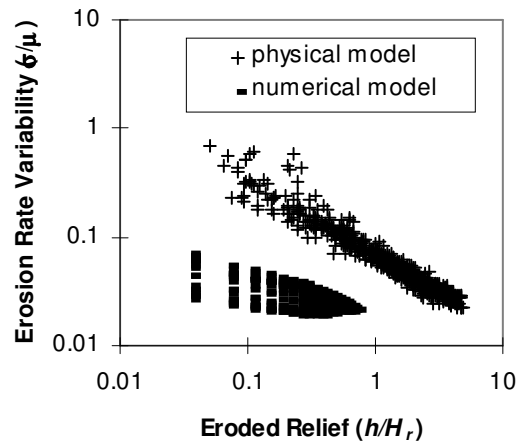
Figure B-5. Coefficient of variation of steady state erosion rate (σ/μ) plotted against eroded relief for runs after complete dissection. Note the axes are logarithmic. Power law exponents for individual runs vary over a narrow range from -0.66 to -0.74. Spatial erosion rates from a numerical erosion model demonstrate roughly order of magnitude lower variability in erosion. Note, data was extracted from numerical model after erosion balanced uplift, but before model reached a static steady state.
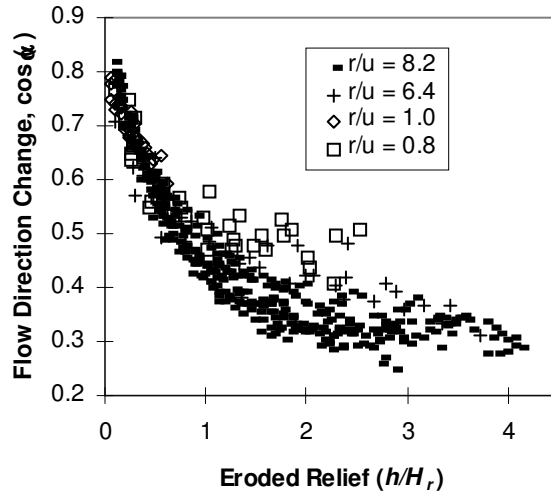
Figure B-6. Average flow direction change plotted against eroded distance for 4 separate runs. The curves shift systematically with the forcing parameter r/u. Average angular change approaches values $> 60°$ for eroded distance on the order of 1 H_r. Angular changes greater than $80°$ are improbable in our experimental basin, because flow is forced to exit the basin at a single outlet.